FEDERAL UNIVERSITY OF SANTA CATARINA
SCHOOL OF TECHNOLOGY
GRADUATE PROGRAM IN AUTOMATION AND SYSTEMS ENGINEERING

Fabio Henriques Mantelli

Multirotor UAV as a Platform for Acoustic Tomography of The Atmosphere

Florianópolis
2020

Fabio Henriques Mantelli

Multirotor UAV as a Platform for Acoustic Tomography of The Atmosphere

Dissertation submited to the Graduate Program in Automation and Systems Engineering of the Federal University of Santa Catarina to obtain the title of Master of Science in Automation and Systems Engineering.
Supervisor: Prof. Alexandre Trofino Neto, PhD.

Florianópolis
2020

Ficha de identificação da obra elaborada pelo autor,
através do Programa de Geração Automática da Biblioteca Universitária da UFSC.

Mantelli, Fabio
Multirotor UAV as a Platform for Acoustic Tomography of The Atmosphere / Fabio Mantelli ; orientador, Alexandre Trofino Neto, 2020.
94 p.

Dissertação (mestrado) - Universidade Federal de Santa Catarina, Centro Tecnológico, Programa de Pós-Graduação em Engenharia de Automação e Sistemas, Florianópolis, 2020.

Inclui referências.

1. Engenharia de Automação e Sistemas. 2. Tomografia Acústica da Atmosfera. 3. Airborne Wind Energy. 4. Perfiladores de Vento. 5. Veículo Aéreo Não Tripulado. I. Trofino Neto, Alexandre. II. Universidade Federal de Santa Catarina. Programa de Pós-Graduação em Engenharia de Automação e Sistemas. III. Título.

Fabio Henriques Mantelli

Multirotor UAV as a Platform for Acoustic Tomography of The Atmosphere

This work at master's level was evaluated and approved by an examining board composed of the following members:

Prof. Felipe Pimenta, PhD.
Federal University of Santa Catarina

Prof. Marcelo de Lellis, PhD.
Federal University of Santa Catarina

Prof. Felipe Cabral, PhD.
Federal University of Santa Catarina

We certify that this is the **original and final version** of the dissertation that was deemed adequate to obtain the master's degree in Automation and Systems Engineering.

Documento assinado digitalmente
Werner Kraus Junior
Data: 27/07/2020 09:28:30-0300
CPF: 531.085.239-53

Coordination of the Graduate Program

Documento assinado digitalmente
Alexandre Trofino Neto
Data: 24/07/2020 10:48:24-0300
CPF: 477.021.687-49

Prof. Alexandre Trofino Neto, PhD.
Supervisor

Florianópolis, 2020.

ACKNOWLEDGEMENTS

First, and foremost, to God, for his overwhelming grace. For his love, care and guidance amidst my doubts and stumbles. For sustaining me and my family along this journey and for fulfilling my life of meaning and purpose.

To my wife, Natália, for her love, support, patience and understanding.

To my mother, Márcia, for being such a role model of competence, excellence, good character, love for the family and for the research.

To my father, Sylvio, for teaching and inspiring me in the ways of the engineering.

To my academic advisor, Prof. Alexandre Trofino, for giving me this opportunity, for pushing me throughout all of this process and for the valuable academic contributions in the development of this work and the structuring of this document.

To my colleagues in the Graduate Program in Automation and Systems Engineering (PPGEAS) and in the UFSCKite lab, for the companionship and ready assistance whenever requested. In special for Matheus Bastos and Artur Leones, which contributed significantly to this work.

To Prof. Aldo von Wangenheim from the Image Processing and Computer Graphics Lab. (LAPiX) lab in Department of Informatics and Statistics (INE)/Universidade Federal de Santa Catarina (Federal University of Santa Catarina) (UFSC), for lending the drone for this research.

To Prof. Felipe Pimenta from the LABDINO in OCN/UFSC, for making the LIDAR wind profiler available to perform the validation experiments.

To the CNPQ, for the master's scholarship and for believing in the potential of the brazilian youth, taking an active part in the development of science and research in Brazil.

To all my professors, who fulfilled their roles in shaping the future of this nation, and in doing so, passed me the knowledge necessary to carry out this work.

Lastly, to God again, which is the beginning and the end. Without him nothing of this would have been accomplished.

RESUMO

Informações detalhadas acerca do perfil de vento e temperatura de determinada localidade são desejáveis durante o processo de avaliação de potencial eólico. De maneira especial, sistemas de *airborne wind energy* (Airborne Wind Energy (AWE)) se beneficiam destas informações para determinação de procedimentos de pouso e decolagem e de altitude ótima de operação. Atualmente, os equipamentos de medição de perfil de vento disponíveis no mercado possuem um alto custo, não podem ser empregados em áreas remotas ou não possuem o alcance desejado para aplicações AWE. Esta dissertação propõe uma solução portátil, reutilizável, autônoma e de baixo custo para medir o perfil de vento e temperatura para avaliação de potencial eólico de localidades para aplicações AWE. A solução consiste no uso de um veículo aéreo não-tripulado (VANT) como uma plataforma de instrumentação para um dispositivo de tomografia acústica da atmosfera. A descrição da arquitetura de hardware e software requerida para desempenhar todas as funcionalidades necessárias para operação contínua de dispositivo de tomografia acústica baseado em VANT multirotor é apresentada. O software de tomografia acústica proposto é aplicado em um modelo de atmosfera de acordo com a configuração de hardware estipulada. Os resultados alcançados em simulação foram comparados com os obtidos de outros perfiladores de vento baseados em VANT e apresentaram um desempenho similar ou superior a estes. Os resultados da dissertação demonstraram que o dispositivo proposto potencialmente tem precisão suficiente para ser utilizado como instrumento de medição atmosférica.

Palavras-chave: Tomografia acústica da atmosfera. *Airborne Wind Energy*. Perfiladores de vento. Veículo aéreo não-tripulado.

RESUMO EXPANDIDO

Introdução

Uma alternativa existente para a geração de energia eólica consiste no uso de dispositivos suspensos no ar ou *Airborne Wind Energy (AWE)*. Estes dispositivos são suspensos por forças aerostáticas ou aerodinâmicas e convertem a energia cinética do vento em eletricidade. O conhecimento do perfil do vento nas localidades onde esta tecnologia potencialmente será implementada traz uma série de benefícios. Estas informações são úteis nesta etapa de prospecção para auxiliar a determinação da altitude ótima de operação e de procedimentos de pouso e decolagem. Turbinas eólicas convencionais também se beneficiam destas informações na etapa de prospecção de localidades. Entretanto, a tecnologia convencional de perfiladores de vento, baseada em RADAR, SODAR e LIDAR possui uma série de desvantagens, dentre as quais se destacam o alto custo dos equipamentos, limitações quanto à operação em certas condições meteorológicas e limitações referentes ao alcançe e resolução.
Esta dissertação explora em profundidade, pela primeira vez, o uso de um Veículo Aéreo Não-Tripulado (VANT) do tipo Vertical Take-Off and Landing (VTOL) como plataforma para a tomografia acústica da atmosfera. Um dispositivo baseado nesta técnica é proposto para levantar o perfil de vento na etapa de prospecção de localidades para instalação de tecnologia AWE. O dispositivo apresentado possui uma série de características vantajosas para esta aplicação, como o baixo custo, portabilidade e possibilidade de operação autônoma.

Objetivos

O objetivo principal deste trabalho é apresentar um perfilador de vento e temperatura da atmosfera autônomo, portátil, reutilizável e de baixo custo para prospecção de sítios eólicos. O dispositivo proposto deverá ser projetado de acordo com as especificações do sistema Pumping Kite Power System (PKPS) do grupo UFSCKite (`https://ufsckite.ufsc.br/`). Para alcançar este objetivo principal, uma série de objetivos secundários devem ser cumpridos, os quais são:

1. Conduzir um estudo a respeito do uso da tomografia acústica como método para medir o perfil de vento da atmosfera.
2. Simular a aplicação da técnica de tomografia acústica da atmosfera no contexto desejado a fim de avaliar a sua adequação para o uso proposto.
3. Projetar um protótipo que permita uma análise comparativa da técnica com as alternativas existentes.
4. Construir e validar um algoritmo de tomografia acústica da atmosfera por meio de simulação, de acordo com o protótipo projetado.
5. Avaliar os resultados obtidos em comparação com técnicas semelhantes de medição de vento baseadas em VANT.

Metodologia

A metodologia proposta por esta dissertação para cumprir os seus objetivos é baseada nas configurações de tomografia acústica apresentadas nos trabalhos de Kevin Rogers

e Finn (2013), V.E. Ostashev *et al.* (2000) e Vecherin *et al.* (2006). O algoritmo de tomografia apresentado utiliza as medições do tempo de propagação de um amplo conjunto de raios acústicos que atravessam um determinado volume da atmosfera para estimar os valores de temperatura e velocidade do ar dentro deste volume. Para analisar e validar tal algoritmo, ferramentas de simulação são utilizadas para gerar valores de entrada através de modelos matermáticos do perfil de vento da atmosfera e da propagação do som no ar, de acordo com a configuração proposta. Os modelos e ferramentas utilizadas na simulação são apresentados em detalhe.
No que diz respeito ao protótipo, sensores e atuadores são necessários para emitir e medir os sinais que posteriormente serão utilizados como valores de entrada dos algoritmos. Os princípios de instrumentação por trás dos sensores e atuadores acústicos e de sistemas de posicionamento ou navegação relevantes para esta aplicação são apresentados.

Resultados e Discussão

Um protótipo de tomografia acústica é proposto baseado nos algoritmos, modelos, princípios de instrumentação e sistemas de posicionamento apresentados. A arquitetura de sistema do protótipo é apresentada, descrevendo os arranjos entre os diferentes subsistemas de software e hardware. Os sistemas de hardware e software são separados em módulos distribuídos em solo e embarcados no VANT. Os módulos embarcados contem a instrumentação necessária para emitir sinais acústicos e controlar a trajetória do VANT, enquanto os módulos de solo contém a instrumentação necessária para mensurar sinais acústicos.
O método de validação do sistema é baseado em simulação. Os parâmetros e a estrutura de simulação adotada que correspondem ao protótipo projetado são apresentados em detalhes. Após isso, os resultados obtidos com a simulação são apresentados e comparados com os trabalhos de Palomaki *et al.* (2017) e Finn *et al.* (2017). A análise comparativa demonstra que os resultados obtidos em simulação pelo dispositivo de tomografia baseado em VANT multirotor provêm estimações de direção e velocidade do vento com performance melhor que os outros dispositivos aos quais está sendo comparado. As estimações obtidas para direção e velocidade do vento possuem desempenho suficientemente adequado para uso em observações meteorológicas, segundo os requisitos da World Meteorological Organization (WMO). Já os resultados de estimação de temperatura apresentaram uma qualidade insatisfatória, com um bias elevado, tornando-os inadequados para observação meteorológica.

Considerações Finais

Nesta dissertação, um projeto de hardware e software para um dispositivo de tomografia acústica baseado em VANT multirotor a fim de ser usado durante o processo de avaliação de sítios eólicos é apresentado. Uma simulação contendo os principais algoritmos e modelos que envolvem a tomografia acústica é proposta. O desempenho dos resultados obtidos em simulação são comparados com outros dispositivos de medição de vento baseados em VANT. Os resultados obtidos nesta dissertação demonstram que os algoritmos e princípios de medição e instrumentação apresentados no projeto de hardware e na simulação apresentam as funcionalidades adequadas para medir o perfil de vento com um desempenho similar a outros dispositivos base-

ados em VANT. Com pequenas alterações, o sistema proposto possui o potencial de atender os requisitos da WMO para instrumentos de observação meteorológica.
A solução proposta nesta dissertação é inovadora e possui uma série de características vantajosas para aplicações de AWE. Além disto, a tecnologia aqui proposta pode se tornar uma alternativa de baixo custo para obter medidas do perfil de vento da atmosfera nas mais diversas aplicações. Os resultados apresentados apresentam um conjunto preliminar de ferramentas que permitirão um posterior estudo, avaliação, desenvolvimento, validação, análise estatística e aprimoramento da técnica de tomografia acústica da atmosfera pelo grupo UFSCKite.
Palavras-chave: Tomografia acústica da atmosfera. *Airborne Wind Energy*. Perfiladores de vento. Veículo aéreo não-tripulado.

ABSTRACT

In the process of wind resource assessment, detailed information about the wind and temperature profile of the site being assessed is desirable. This is specially true for airborne wind energy (AWE) systems, for which this information is relevant in determining the take-off and landing procedures and finding an optimal operating height of the system. Current autonomous devices commercially available are expensive and can not be employed in remote areas or can not reach the desired height range for AWE applications. The present dissertation proposes a portable, reusabe, low-cost automated solution to measure the wind and temperature profile for AWE assessment applications. The solution consists on the usage of an Unmanned Aerial Vehicle (Unmanned Aerial Vehicle (UAV)) as an instrumentation platform of an Acoustic Atmosphere Tomography (AAT) device. A hardware and software architecture for the multirotor UAV-based AAT device is described to perform all of the functionalities required for its full continuous operation. The proposed AAT software is applied to an atmosphere model in accordance to the stipulated hardware setup. The results obtained in simulation environment were compared to other similar UAV-based wind profilers and presented accuracy performances close to or better than them. The dissertation results has shown that the proposed device has the potential to be accurate enough to be used as a weather observation instrument.

Keywords: Acoustic Tomography of the Atmosphere. Airborne Wind Energy. Wind Profilers. Unmanned Aerial Systems.

LIST OF FIGURES

LIST OF TABLES

LIST OF ABBREVIATIONS AND ACRONYMS

AAT	Acoustic Atmospheric Tomography
AC	Alternating Current
ADC	Analog to Digital Converter
AWE	Airborne Wind Energy
CCA	Cross-Correlation Algorithm
CORS	Continuously Operating Reference Station
DC	Direct Current
DOA	Direction of Arrival
GNSS	Global Navigation Satellite System
IMU	Inertial Measurement Unit
INE	Department of Informatics and Statistics
INS	Inertial Navigation System
ISA	International Standard Atmosphere
LAPiX	Image Processing and Computer Graphics Lab.
LASER	Light Amplification by Stimulated Emission of Radiation
LIDAR	Light Detection And Ranging
LOS	Line Of Sight
MAV	Manned Aerial Vehicle
MEMS	Micro Electro Mechanical systems
NTP	Network Time Protocol
OS	Operating System
PKPS	Pumping Kite Power System
PPGEAS	Graduate Program in Automation and Systems Engineering
PPK	Post-Processed Kinematic
PPS	Pulse-Per-Second
RADAR	Radio Detection And Ranging
RBF	Radial Basis Function
RF	Radio Frequency
RMSE	Root Mean Square Error
RSSI	Received Signal Strength Indication
RTF	Ready To Fly
RTK	Real-Time Kinematic
RWP	RADAR Wind Profiler
SNR	Signal-to-Noise Ratio
SODAR	Sound Detection And Ranging
TDOA	Time Difference of Arrival
TOA	Time of Arrival
UAS	Unmanned Aerial System

UAV	Unmanned Aerial Vehicle
UFSC	Universidade Federal de Santa Catarina (Federal University of Santa Catarina)
USART	Universal Synchronous Asynchronous Receiver Transmitter
USB	Universal Serial Bus
VANT	Veículo Aéreo Não-Tripulado
VTOL	Vertical Take-Off and Landing
WMO	World Meteorological Organization

LIST OF SYMBOLS

i	Sound ray index
δV_x	Deviations in the wind velocity component in the direction x
δV_y	Deviations in the wind velocity component in the direction y
δV_z	Deviations in the wind velocity component in the direction z
δT	Deviation in the acoustic temperature
j	RBF index
$\hat{L}_i$	Unit vector tangent to the straight line ray path i
l_i	Length of the straight line ray path i
N_R	Total number of ray paths
N_{RBF}	Number of RBFs for each RBF network
τ	Propagation time of an acoustic wave
$\vec{V}_0$	Average wind velocity vector
u_z	Mean wind speed at the height z
u_*	Friction velocity in ms^{-1}
κ	Von Kárman's constant
z	Height variable
z_0	Roughness length in meters
u_1	Wind speed at height z_1
z_1	Height variable
p	Exponential parameter between 0 and 1
u_2	Wind speed at height z_2
z_2	Height variable
c_L	Speed of sound in a motionless atmosphere
γ	Ratio of specific heats (adiabatic index) for dry air
R	Gas constant for dry air
T	Acoustic temperature
T_a	Dry air temperature in Kelvin
q	Specific humidity
$\vec{U}$	Sound wave group velocity vector
n	Unitary vector normal to the wave front
$\vec{V}$	Wind velocity vector
A_a	The attenuation in dB due to atmospheric absorption of a plane sound wave
S_0	Intensity of the plane sound wave at origin
S	Intensity of the plane sound wave after propagating the distance r in a direction perpendicular to the phase front
r	Propagation distance of a sound wave
a	Absorption coefficient in $\mathrm{dB\,m^{-1}}$
Γ	Ray path

l	Position inside the ray path variable
c_0	Average speed of sound
δc	Speed of sound deviations
$\delta \vec{V}$	Wind velocity deviation vector
T_0	Average acoustic temperature
δF	Function representing a generic quantity function that can be replaced by δV_x δV_y δV_z or δT
k	Scaling or spread factor of the RBF
$h_{i,j}$	The shortest distance between the ray path i and the center of the RBF j
$d_{i,j}$	The distance from the beginning of the ray path i to the orthogonal projection of the center of the RBF j to the ray path i
W_{Fj}	Weigh of the RBF j related to quantity F
$\Omega_{i,j}$	Projection of the RBF j at the ray path i. Defined in Eq. 18
$\mathbf{\Omega_i}$	Column array containing the projection of every RBF at the ray path i. Defined in Eq. 18
$\mathbf{W_F}$	Column array containing the weighs of all of the RBFs related to quantity F
erf	Gauss error function. Defined as $\text{erf}(x) = \frac{2}{\sqrt{\pi}} \int_0^x e^{-t^2} dt$
$\mathbf{L}$	Column array that contains the length of each sound ray
$\boldsymbol{\tau}$	Column array that contains the propagation time of each sound ray
$\mathbf{L}_x$	Column arrays of size $N_r \times 1$ containing the x components of the displacement vector from the acoustic source to the receiver $(\hat{L}_i \cdot l_i)$ for every ray
$\mathbf{L}_y$	Column arrays of size $N_r \times 1$ containing the y components of the displacement vector from the acoustic source to the receiver $(\hat{L}_i \cdot l_i)$ for every ray
$\mathbf{L}_z$	Column arrays of size $N_r \times 1$ containing the z components of the displacement vector from the acoustic source to the receiver $(\hat{L}_i \cdot l_i)$ for every ray
$\mathbf{\Omega}$	Matrix of size $N_R \times N_{RBF}$ containing the projection of every RBF on each ray path
$\mathbf{W_T}$	Column array of size $N_{RBF} \times 1$ that contains the weights of the RBF network for δT
$\mathbf{D}$	$D(v)$ returns the diagonal matrix with elements of v in the main diagonal
$\mathbf{W_V}_x$	Column array of size $N_{RBF} \times 1$ that contains the weights of the RBF network for δV_x
$\mathbf{W_V}_y$	Column array of size $N_{RBF} \times 1$ that contains the weights of the RBF network for δV_y
$\mathbf{W_V}_z$	Column array of size $N_{RBF} \times 1$ that contains the weights of the RBF network for δV_z
$\mathbf{b}$	Column array where $b_i = \frac{\tau_i}{l_i}$
$\mathbf{J}_{N_R}$	Column array of ones with length N_R

$\hat{\mathbf{L}}_x$	Column array containing the x components of the unitary vectors pointing in the ray path direction for every ray
$\hat{\mathbf{L}}_y$	Column array containing the y components of the unitary vectors pointing in the ray path direction for every ray
$\hat{\mathbf{L}}_z$	Column array containing the z components of the unitary vectors pointing in the ray path direction for every ray
V_{0x}	x component of $\vec{V}_0$
V_{0y}	y component of $\vec{V}_0$
V_{0z}	z component of $\vec{V}_0$
u	Mean wind speed variable
V_x	Wind velocity component in the direction x
V_y	Wind velocity component in the direction y
V_z	Wind velocity component in the direction z

CONTENTS

1 INTRODUCTION

The electric energy consumption has been steadily increasing in the past decades and, along with this trend, the demand for sustainable power generation (GOLDEMBERG et al., 2000). Systems that harvest the kinetic energy of the wind are presented as clean, renewable and low impact power generation options that are quite attractive in comparison to other alternatives (EVANS et al., 2009). Among the many variants of wind power systems, the conventional horizontal axis wind turbines are responsible for the largest part of power generation in the world. The horizontal wind turbines economically viable and commercially available today have a generation capacity of up to 20 MW and need large amounts of steel, concrete and other materials to be built and installed. The cost to transport the large structures that compose a wind turbine and the materials required for their assemble limits the potential sites of wind farms. Also, once the wind turbines reach the end of its lifetime, another issue arises: A large volume of materials need to be transported away to proper disposal sites, without the possibility of being recycled, incurring in additional costs. An argument could be made that perhaps larger, higher capacity wind turbines may increase the profitability of wind farms and therefore increase the amount of sites viable for the conventional wind turbine technology. However, it is believed that the conventional technology is reaching its scalability limit because any raise in rated capacity may not compensate the increased cost in materials, foundations, installment, transport and logistics. Besides that, even for low power systems, many times government subsidies are required in order to make wind projects viable (THRESHER et al., 2007).

As an alternative to conventional wind power systems that may circumvent these limitations, a new paradigm in wind power generation has been studied the past decade: Airborne Wind Energy (AWE) (FAGIANO; MILANESE, 2012). It consists in an approach where devices suspended in the atmosphere either through aerostatic or aerodynamic forces convert the kinectic energy of the wind into electricity. AWE systems do not need large towers or rigid mechanical structures for its operation and may operate in elevated altitudes, much above the reach of conventional wind turbines, whose blade tips currently reach about 200 m. Since wind speed tends to increase with altitude and considering that the wind power available is proportional to the cube of the wind speed, the possibility of operation in higher altitudes consists in one the main advantages of AWE systems over conventional wind turbines (ARCHER; CALDEIRA, 2009). Another advantage that AWE systems have over conventional wind turbines is the drastic cost reduction. The steel or concrete tower is replaced by tether lines and the large steel blades are substituted by a light-weighted aerostatic or aerodynamic structure. This incurs in a decrease in transport and installation costs. Also, maintenance in AWE systems can be performed on the ground, by landing the airborne unit, which reduces

costs and simplifies procedures.

However, AWE technology still faces some particular challenges, such as automated take-off and landing. In addition, robust, efficient, long-term operation of this technology is yet to be demonstrated. To better study and propose solutions for those challenges, a good knowledge of the wind profile at the sites where the technology will potentially be implemented is desirable. This is due to the fact that wind speed and direction in lower heights greatly affects take-off and landing procedures of AWE devices. Also, the knowledge of the wind profile is useful in the process of determination of the flight trajectory and optimal operating height of the airborne devices. Thus, the local wind profile becomes a desirable characteristic to be known when assessing a specific site for the implementation of AWE technology.

The wind resource assessment process is usually based on wind measuring devices mounted upon meteorological masts (NREL, 1997). For this process, one or several anemometers are installed at fixed heights on the mast. This introduces a limit to the height of the measurements taken due to the mast size, which usually is about 50 or 60 m. The problem with this method is that the logistics of transporting and installing this kind of platform are costly, which makes it not feasible for remote sites to be assessed for wind farming. Also, the height limitation of this method means that by itself it is not an adequate option to evaluate sites for airborne wind energy (AWE) systems. AWE systems have been presented as potential substitutes for the conventional wind turbines as the main paradigm in wind harvesting (RANNEBERG et al., 2018; ZILLMANN; BECHTLE, 2018). They can harvest wind power from variable altitudes and many of such devices depend on the wind near surface to take off and land. Thus, the knowledge of the wind profile on the sites being evaluated is needed for this technology. RADAR, SODAR and LIDAR are currently the devices commercially available for autonomous wind profile measurement in the lower layers of the atmosphere. They are based on remote sensing techniques that rely on the backscattering of radio, sound or light waves, respectively, on the atmosphere. These devices are often very expensive and in some cases require a substantial amount of power for their operation. Those reasons sometimes makes them inadequate for wind assessment.

This dissertation presents a new strategy to perform the measurements required in the assessment of potential wind farm sites. It employs a technique called acoustic tomography and a multirotor UAV (*unmanned aerial vehicle*) to estimate the temperature and the wind vector field in a determined three-dimensional volume of the atmosphere. The technique is based on the fact that the propagation speed of acoustic signals varies with the temperature and the velocity of the wind through the signal path. If the propagation time of an acoustic signal is measured, an average propagation speed along its path may be obtained. If enough rays traverse a certain volume of the atmosphere at different angles, the variations of the propagation speed vector fields inside the vol-

ume can be estimated. These variations in the propagation speed can be mapped to changes in the temperature and wind velocity fields. Fig. 1 shows the schematic of the multirotor-UAV-based acoustic tomography device. In this dissertation, it is proposed that a UAV carries a siren in it's payload module as the acoustic source for the atmospheric tomography. A matrix of microphones is spread on the ground as the acoustic receivers. The drone executes a mission, traversing a determinate trajectory while emitting acoustic pulses that cross certain atmospheric volume. A time delay estimation algorithm processes the data collected by the microphone and sends information about the propagation time of each sound pulse to the tomography algorithm. Precise information about the location of the UAV at the moments where the pulses are emitted is collected during the mission. After the mission is complete, the drone lands in a shelter, where its batteries are automatically recharged. A battery bank located on the shelter, which is recharged by a solar panel, provides the power necessary to operate the whole system.

Figure 1 – Schematic of the multirotor-UAV-based acoustic tomography device.

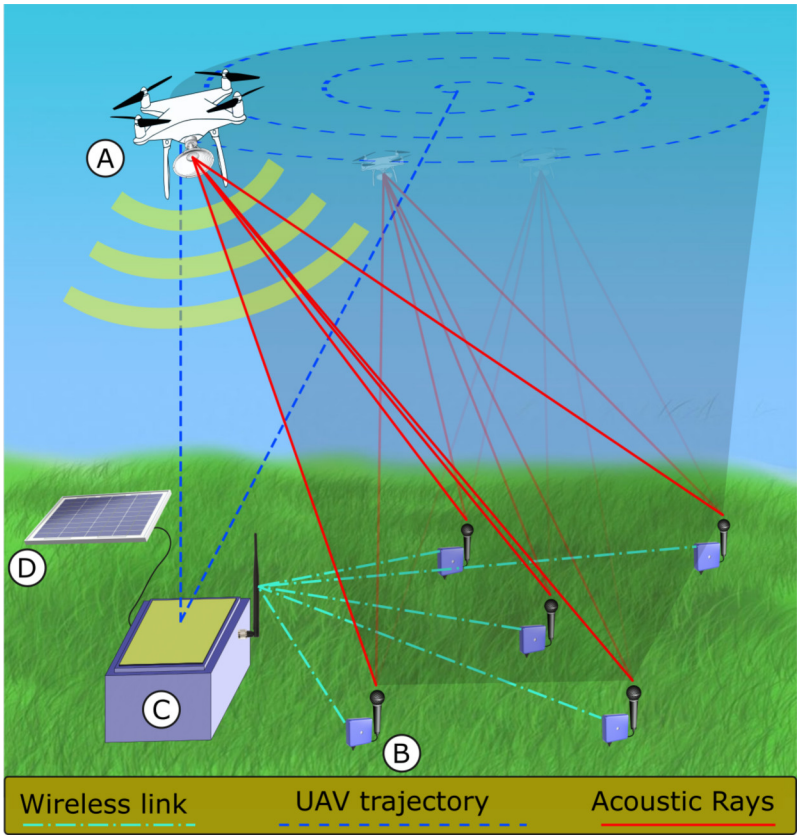

Source: Own elaboration. A) Multirotor UAV with a siren in the payload module; B) Ground module, with microphone; C) Shelter; D) Solar panel.

This dissertation explores in depth, for the first time, the usage of a multirotor or Vertical Take-Off and Landing (VTOL) (*Vertical Take-Off and Landing*) UAV as a

platform for acoustic tomography of the atmosphere. This platform has an advantage over fixed-wing UAVs for evaluating potential wind farm sites because it is capable of performing automatic vertical take-off and landing procedures. Another advantage is the possibility to automatically recharge its batteries between missions with the assistance of photovoltaic solar panels, a battery bank and a charging pad. Such device can be applied in the wind resource assessment process for both conventional and airborne wind energy applications. A portable, low-cost, multirotor-UAV-based wind profiler may also be used as a complement or in substitution of conventional wind profilers for atmospheric boundary layer measurements in many applications. It may even be used in situations where the conventional technology can not be employed satisfactorily, such as in certain complex terrains or atmospheric conditions (BANTA et al., 2012). Moreover, the device presented in this dissertation can, with minimal modifications, provide the wind profile inside a three-dimensional volume of the atmosphere, which is of special interest for the boundary-layer meteorology field of study. Conventional wind profilers can only provide the wind profile of a cone-shaped volume of the atmosphere. With the device presented in this dissertation, the shape of the volume of the atmosphere being measured can be determined by the user according to his convenience with great flexibility.

This dissertation presents the efforts made by the author to explore, study, design, simulate and test a wind-measuring device adequate for AWE systems. Sec. 1.2 presents the objectives of the dissertation. Ch. 2 presents in detail the preliminary study realized on the atmospheric boundary layer wind measurement platforms and instruments, on the use of aircraft to measure wind, on the atmospheric acoustic tomography and on the usage of UAVs as a tomographic platform. In Ch. 3, a brief theoretical foundation about the boundary layer wind profile and propagation of sound in the atmosphere is presented. Afterwards, the instrumentation and algorithm methods employed by the multirotor UAV-based acoustic atmospheric tomography device are presented. A great effort was made by the author in designing and assembling the hardware architecture. However, this is a complex system with a lot of subsystems integrated together, and the purchase, assembly and testing process of this integrated device presented unexpected difficulties which delayed the development process. The hardware components of the ground and payload modules were purchased, the modules were assembled and some of the low-level subsystems were individually validated experimentally. However, complete functional experiments of the modules were not performed in time to be included in this document. The Mikrokopter MK EASY Okto XL2 4S (`https://www.mikrokopter.de/en`) was lended from the LAPiX to be the UAV system used in this work, and flight tests with the desired trajectory were performed. Nevertheless, no test flight was performed with the payload module embedded in the UAV. Since the full development of the prototype was not achieved as initially intended,

the advancements made in the experimental setup are presented in Ch. 4 in the form of the system architecture design. The ground and payload instrumentation modules, the simulation setup, its results and a comparative analysis are presented in Ch. 4. The conclusions and future work are presented in Ch. 5.

1.1 PUMPING KITE PROTOTYPE

The system presented in this dissertation is designed to be used as a wind assessment tool for an AWE prototype system proposed by the UFSCKite lab (`https://ufsckite.ufsc.br/`). The prototype currently being developed in UFSCKite consists of a pumping kite power system (PKPS). The pumping kite concept is first presented by Loyd (1980) and consists in using a tethered wing, which can be rigid or flexible, whose trajectory is controlled to achieve large traction on the tether and unroll a reel. The reel is attached to the axis of an electric machine, generating power while unwinding. This consists of the active phase of the operation of the system, in which power is being generated. Once the reel is unwound, the system enters a passive phase, in which the wing trajectory is controlled to minimize the traction force on the tether. In this phase, the electric machine is used to rewind the reel, spending a small portion of energy from the grid. Fig. 2 illustrates the trajectory and the principle of operation of the pumping kite prototype being developed in the UFSCKite laboratory. The power balance between the active and passive phases of the PKPS is positive, and the system can be used to generate power. The prototype currently being developed in UFSCKite is designed to operate in heights of up to 600 m of altitude and wind speeds between 5 and 13 $\mathrm{m\,s^{-1}}$. Since the acoustic tomography device presented in this dissertation is intended to be used in conjunction with the pumping kite prototype, those ranges are being used as requirements for the system presented in this dissertation.

1.2 OBJECTIVES

The main goal of this work is to propose a portable, reusable, low-cost automated solution to measure the wind velocity and temperature profile for airborne wind energy assessment applications. The device proposed shall be designed taking into account the PKPS state of art context, in which the UFSCKite lab is currently inserted, and the near-future expected developments. Based on the UFSCKite PKPS, the proposed wind profiler should be able to perform its measurements on heights up to 600 m above ground level in remote sites, with limited or no access to the power grid, as the application of AWE systems may be particularly useful in remote sites (LUCHSINGER et al., 2018). Currently, the commercially available devices able to measure the wind profile are inadequate for this application. Their characteristics, advantages and limitations are further discussed in Sec. 2.3.9. VTOL UAV systems are particularly useful

Figure 2 – The UFSCKite pumping kite prototype schematic.

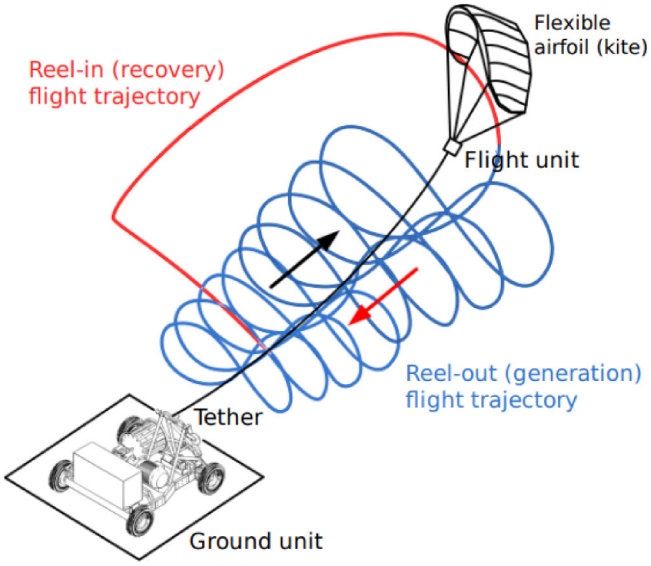

Source: https://ufsckite.ufsc.br/ufsckite-eng/.

for remote automatic applications due to the fact that these systems operate on a low power budget and are not costly in comparison to other commercially available wind profilers. Also, a wide array of lightweight instruments and sensors may be embedded in UAV systems in a very simple manner. Thus, VTOL UAV systems present themselves as an advantageous instrumentation platform to be used to measure the wind profile in the pretended height range. The solution proposed in this dissertation is based on this technology. Sec. 2.4 presents different methods to perform wind velocity measurements using rotary-wing UAV as a platform. Of the methods proposed, the device presented in this dissertation uses the acoustic tomography technique to estimate the wind profile.

In order to achieve the main objective of this work, a series of specific objectives may also be stated, which are presented as follows.

1. Conduct a study of the acoustic tomographic technique as a method of measuring the wind profile of the atmosphere.

2. Simulate the application of the acoustic tomography technique on the desired context in order to evaluate its adequacy.

3. Design a prototype that may allow a comparative analysis of the technique with its existing alternatives.

4. Build and validate an acoustic atmospheric tomography (AAT) algorithm by simulation in accordance with the designed prototype.

5. Evaluate the results obtained in comparison to similar UAV-based wind-measuring techniques.

2 LITERATURE REVIEW

2.1 CHAPTER INTRODUCTION

This literature review is hereby presented with the objective of determining the state of the art in the usage of multirotor UAVs to measure wind speed and direction, specially in wind resource assessment applications. In order to achieve this objective, a systematic revision was made according to the recommended procedures presented by Silva and Menezes (2001). As suggested by Silva and Menezes (SILVA; MENEZES, 2001), the objective of this chapter is to present an empiric review trying to understand how the acoustic tomography has been researched over time and what are the methods currently being applied to measure the wind profile on the surface and boundary layer. In what relates to the acoustic tomography, the following review is focused towards the publications that presents tomography devices operated with the aid of *Unmanned Aerial Systems* (Unmanned Aerial System (UAS)). Starting from a pre-determined structure, this bibliographic survey was done mainly from review articles, digital research databases, internet search engines and through bibliographic citations made by articles and books that relate to this dissertation subject. After the initial survey, the bibliography was analyzed and classified. After a critical analysis and interpretation of the gathered material, the results of this study are presented in this chapter.

In this chapter, a bibliographic study about the current wind sensors and platform technologies used in wind speed and direction measurement in the boundary layer is initially presented. Subsequently, the last developments in the use of UAS on wind measurement are described. Finally, references of works that use acoustic tomography to measure the atmosphere's wind profile are presented, highlighting the works that present the application of this technique with the aid of UAS.

2.2 BOUNDARY LAYER WIND MEASUREMENT PLATFORMS

According to Giebel et al. (2012) and Moyano Cano (2013), many platforms are used to assemble wind sensors for the analysis of wind profile in the boundary layer of the atmosphere. They are: towers, tethered balloons, kites, ground stations, Manned Aerial Vehicle (MAV)s, solar balloons, masts and radiosondes. In the sequel, those platforms are presented and compared with respect to their cost, spatial and temporal resolution, data transmission, ease of application, operation automation level and other practical aspects. Fig. 3 illustrates the platforms described in this section.

The towers, ground stations and masts are rigid platforms, on which different desired sensors are attached. Those are simple platform options that do not present any particular hindrance on data transmission due to the possibility of direct connection between the sensor devices and the data storage unit. Additionally, the temporal reso-

Figure 3 – Platforms and instruments for wind measurement in the atmospheric boundary layer.

Source: (MOYANO CANO, 2013, p. 12). a) Meteorological tower, b) Weather station in a mast, c) MAV, d) Tethered balloon, e) Kite, f) UAVs, g) Radiosonde, h) SODAR/LIDAR/Radio Detection And Ranging (RADAR) in ground station.

lution on data collection is limited only by sensor specification. Wind sensors attached to these platforms typically do not need manual operation, however, they are only capable to effectuate point measurements. Multiple sensors installed in different heights are required to get information about the wind profile; and the spatial resolution of the resulting measurements is determined by the amount of sensors employed. Thus, in order to achieve finer resolution, there is a need of a great number of sensors, which can considerably increase the cost of the setup.

Radiosondes and solar balloons are aerostatic devices that contain low density gases inside a latex membrane. Since these gases are lighter than the air, when a radiosonde or a solar balloon is released in the atmosphere, it moves in an ascending trajectory and may carry a small payload with it. The balloon continues its ascending trajectory until a rupture of the membrane happens due to the expansion of its internal gases on elevated altitudes, where the atmospheric pressure is low. When the membrane breaks, the device gets in free fall or parachuted fall. The load capacity of such devices is very small and any collected data have to be immediately transmitted through

a wireless link to a base, where the data storing device is situated. While using such devices, the payload is often not recovered because the device may be carried away by the wind very far from the release point and the cost of its tracking and dislocation may make the retrieval operation unfeasible. The inflation and release operations necessary for balloon platforms need to be performed manually. Those operations are troublesome and time-consuming, and limit the temporal resolution of data collection.

In order to minimize payload loss problems, a tether may be attached to the balloons. However, this limits the altitude reached by these devices by the tether length. A similar problem is also present when using kites as measurement platforms.

UAS, when used as platforms, may provide measurements with better spatial resolution, since they can freely move through the atmosphere. Still, they have a limited operation time and eventually need to be refueled to keep taking measurements. Most of the time, the refueling operation is performed manually by a human operator.

2.3 BOUNDARY LAYER WIND MEASUREMENT SENSORS

Since the late-1980s, a great interest has been shown in studying and improving anemometer technology due to its application on wind resource assessment. This happened because small accuracy errors in the wind sensors propagate to significant errors in the estimated wind power (KRISTENSEN, 1999). Thus, the choice of instrument to measure wind speed and direction should be done carefully in order to reach the most adequate solution. This section consists of a small overview of the most commonly used wind sensors and their adequacy in relation to wind resource assessment application. The wind sensors commonly utilized to perform wind measurements on the boundary layer are, according to (GIEBEL et al., 2012): Cup anemometers, propeller anemometers, sonic anemometers, hot-wire anemometers, sphere anemometers, laser-cantilever anemometers, pitot tube, multi-hole probe, sodar, lidar, and radar. Those are presented, compared and analyzed in the following sections.

2.3.1 Cup anemometers

Cup anemometers are one of the simplest wind sensors being applied in meteorology or in wind energy sector. Most cup anemometers consist of three or four hemispherical cups mounted on horizontal arms, mounted on a vertical shaft at equal angles (see Fig. 4). Horizontal wind blowing from any direction rotates the shaft due to the fact that the drag coefficient of the concave part of the cup is higher than of the convex part. The rotation is often measured by one or multiple reed switches that commute as the shaft is revolving. The wind speed is proportional to the angular velocity of the rotating shaft by a constant that can be determined analytically or by calibration.

Cup anemometers have been the standard instrument used in wind measure-

Figure 4 – P2546A-L Cup anemometer

Source: https://www.campbellsci.com.br/p2546a, accessed Jan. 2020.

ment due to its linear response, ability to measure multi directional horizontal wind speed and overall low cost. In addition of being robust, easy to install and reliable, it requires very low maintenance and thus can be left unattended for years. However, in order to measure wind direction, it needs to be coupled with an additional sensor, usually a wind vane. It also has the limitation that it cannot measure vertical components of wind speed. Due to the mechanical properties of the system, it also has the characteristics of filtering out high frequency variations, and is subject to a phenomena called overspeeding, described in depth in N. Busch and L. Kristensen (1976), where the anemometer responds non-linearly to fluctuating winds.

2.3.2 Propeller anemometers

The propeller anemometer is widely used as a wind measurement sensor. It consists of two to four helicoidal or flat blades attached to a rotor which rotates as the wind flows through them. In a similar manner as the cup anemometers, usually one or more reed switches are used to measure the angular speed of the rotor, which is linearly proportional to the component of the wind speed parallel to the rotating axis of the propeller. Differently to the cup anemometers, the torque experienced by a propeller anemometer is due to lift forces on the blades, rather than drag forces. Since lift forces can exceed drag forces considerably in magnitude, a propeller anemometer can be designed to achieve a faster response than a cup anemometer with equivalent moment of inertia in the rotor. However, constructing a low-weight propeller anemometer capable of resisting gale-force winds is much harder than constructing a robust low-weight cup

anemometer (BUSCH, N. E. et al., 1980). An example of a propeller anemometer can be seen in Fig. 5.

Figure 5 – Propeller anemometer with wind vane

Source: https://www.campbellsci.com/05108-l, accessed Jan. 2020.

A propeller anemometer is a very cheap and low maintenance wind measuring option, but its response for winds incident from any direction other than perpendicular to the rotating axis is not linear in respect to the incident angle. Moreover, its response does not correspond perfectly to the cosine of the angle of attack. Thus, in order to achieve better measurements, the propeller anemometer should be always pointing towards the wind. In order to address this, a propeller anemometer may be attached to a wind vane. In this setting, the system can be built so that the axis of rotation follows the direction of the wind (see Fig. 5). A wind vane with one rotational joint is sufficient to provide 2D wind measurement. A second joint can be added to the wind vane in order to collect 3D wind measurements. Another manner to collect 3D wind information with propeller anemometers is by using a set of three sensors with their rotation axis orthogonal to each other. However, this solution does not escape from the nonlinear angular response problems. The propeller anemometer does also present, although in a smaller degree, overspeeding problems similar to those ones present in cup anemometers (BUSCH, N. E. et al., 1980).

2.3.3 Ultrasonic anemometers

The ultrasonic anemometer (see Fig. 6) is another very common sensor in wind resource assessment. It uses ultrasonic acoustic waves to measure wind velocity. A pair of an ultrasonic emitter and receiver is positioned in order to measure the phase

shift of ultrasonic rays caused by the flow of the wind along the ray path. A single ultrasonic ray can only sense the component of the wind in the ray direction. Thus, three emitter/receiver pairs are employed on a sensor in order to get measurements of 3D wind components.

Figure 6 – 3D ultrasonic anemometer

Source: https://www.campbellsci.asia/81005, accessed Jan. 2020.

This remote measuring device does not contain any moving parts and has high frequency response and fine temporal resolution. It is a sensor which requires low maintenance and does not need any recalibration. This fact minimizes downtime of the sensor which leads to high levels of data availability.

However, there are some disadvantages in using ultrasonic sensors. They are expensive, compared to the other options already stated. The emitter and receiver supports introduce distortion to air flow. Also, ultrasonic sensors are subject to performance degradation in the presence of precipitation due to caustics and sound speed variations that may happen on account of temperature and humidity variations. Despite that, the effect of humidity and temperature on ultrasonic measurements is well understood and can be compensated with additional sensors or often times, neglected.

2.3.4 Hot-wire and hot-film anemometers

Hot-wire and hot-film anemometers are devices used to measure a combination of wind velocity and temperature. It works with a thin wire or film heated by joule effect which is cooled by the air flow. As the wire or film is cooled, the resistance of the wire changes making it possible to extract information about the incident flow. There are two modes of operation of hot-wire or hot-film anemometers, constant current, or constant

temperature. In constant current mode, a current source supplies a stable current to the hot wire or film and a voltage sensor measures the electric potential difference on the wire which is related to the air flow parameters. In constant temperature mode, an electric circuit is applied in order to control the temperature of the hot wire or film to maintain it slightly above ambient temperature. As the air flows through the wire or film and cools it, more power is required on the sensing device to maintain its temperature. The power dissipated in the hot wire or film can be known by measuring the value of the current necessary to obtain such equilibrium. The power dissipated in a hot-wire or hot-film anemometer in the constant temperature mode can be related to the air flow through correct calibration (DOBSON et al., 2012).

Hot-wire or hot-film anemometers have a high frequency response, with fine spatial resolution, and present no moving parts. Those characteristics are highly advantageous in meteorological applications. However, a single wire or film cannot be used to determine wind direction. Multi wire probes are commercially available and may be used to acquire 3D flow measurements (EBEFORS et al., 1998), however, their measurements still drift over time, and require frequent calibration. Fig. 7 illustrates configurations for 1D(a), 2D(b) and 3D(c) hot-wire probes. The calibration of a 3D hot-wire/film probe is not a simple operation and requires additional equipment which may make its usage not time or cost effective for wind resource assessment operations. The calibration may be performed by removing the probe of its installation site and subjecting it to a range of known flow velocities at a variety of angles, in a wind tunnel or using a reference jet flow. Another alternative is to calibrate the probes *in situ*, with additional wind measurement equipment, such as ultrasonic anemometers (KIT; LIBERZON, 2016). Another big disadvantage of hot-wire anemometers is that the sensing wire is often too fragile to be used in any application other that measuring the flow of pure, clean gas. Hot-film probes are mechanically stronger and can be used in liquid, smoke or in other gas fluids that have dirt or debris or even outdoors in rainy condition. At the other hand, the thermal inertia of hot-film probes is larger than that of hot-wire probes and thus it presents a lower frequency response.

Figure 7 – Different arrays of hot-wire probes

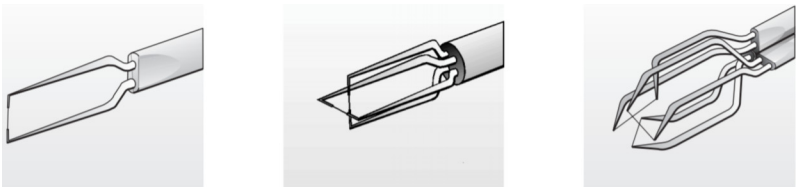

Source: (JØRGENSEN, 2002, p.9).

2.3.5 Sphere anemometers

Sphere anemometers have been firstly described by Reed and Lynch (1963). They are composed of a sphere attached to the tip of a flexible rod. The drag force caused by the wind on the sphere causes a deflection on the tip of the rod which is proportional to the wind velocity. The deflection of the rod in one direction was originally measured by a strain gauge fixed at the broader side of a rod with rectangular section. Modern options use circular section rods and laser distance sensors (HÖLLING et al., 2007). The laser beams are projected into the sphere and reflected by a surface located inside the sphere. The reflected laser beam is split on a beam splitter and projected on a measuring device. The reflection position is affected by the sphere dislocation caused by the wind forces. In order to measure 2D components of wind velocity a 2D position sensitive photodetector can be applied to acquire the position of the reflecting spot. Fig. 8 illustrates the measuring principle of the sphere anemometer.

Figure 8 – Sphere anemometer principle of functioning.

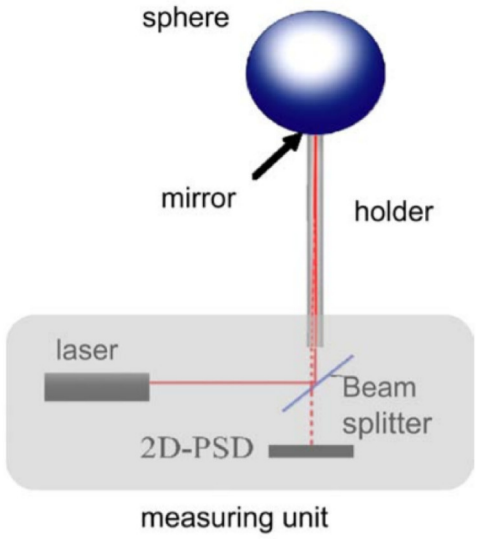

Source: (HÖLLING et al., 2007, p. 3).

Sphere anemometers require very low maintenance, due to the fact that they have no moving parts and do not need constant recalibration. Its measurements are accurate and they have a higher frequency response than cup anemometers that is comparable, but not as good as hot-wire anemometers' frequency response (HÖLLING et al., 2007). However, equipment with precision laser distance measurements are costly and the sphere anemometer cannot measure wind velocity components parallel to the rod length.

2.3.6 Laser-cantilever anemometers

A laser-cantilever anemometer uses a very small cantilever that is deformed by the drag forces caused by fluid flow passing through it. A laser beam is projected on the cantilever and the beam is reflected back and projected into a 2D position sensitive photodetector (PSD), in a manner similar to the sphere anemometer aforementioned. The cantilever shape is made in a way that allows it to be deformed in a different manner by wind components incident from two directions, making the device able to perform 2D wind measurement. This anemometer has a very high temporal and spatial resolution, comparable to hot-wire probes, but without the mechanical fragility. This allows for the Laser-cantilever anemometer to be used in harsher conditions than the hot-wire anemometer (BARTH et al., 2005). However, Laser-Cantilever systems make use of precision laser devices, which usually are very expensive. The system also requires constant calibrations due to the wear of bearings. The laser-cantilever anemometer is also prone to overspeeding, as the cup anemometers, due to the unsymmetrical shape of the cantilever (HÖLLING et al., 2007). Fig. 9 presents the working principle of the laser-cantilever anemometer.

Figure 9 – Laser-cantilever work principle

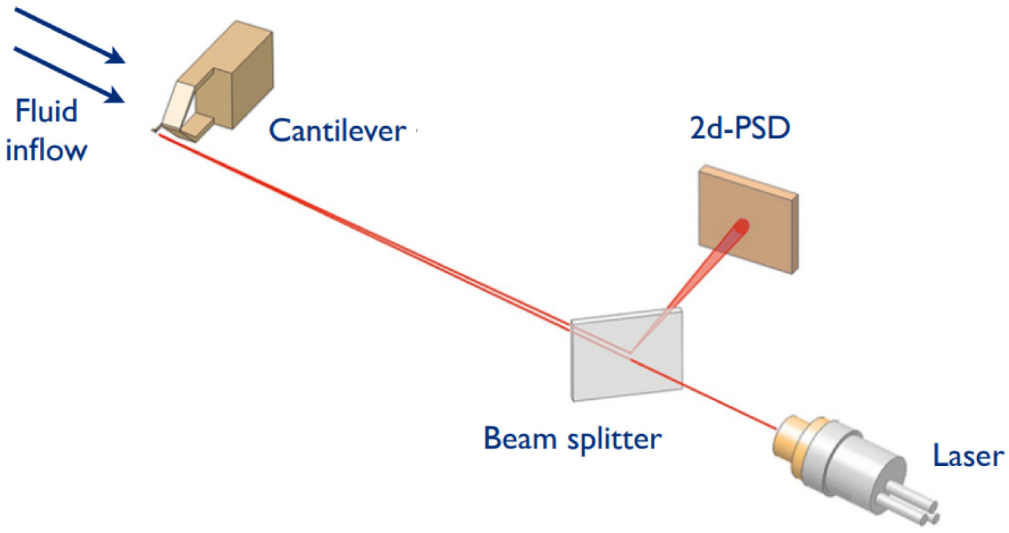

Source: (PUCZYLOWSKI, 2014, p. 3).

2.3.7 Pitot-tube anemometers

Pitot tube anemometers measure the flow velocity of the air by the use of Pitot-static systems with a digital pressure sensor. They are based on Bernoulli's principle, which states that an increase in the speed of fluid occurs simultaneously with a decrease

in pressure (CLANCY, 1975). Thus, by comparing the stagnation pressure obtained in the Pitot tube with the static pressure obtained in a static port, we can obtain the dynamic pressure, which is proportional to the air speed incident in the Pitot tube.

It is an anemometer usually applied in ducts, aircraft, and other applications where the direction of fluid flow is usually constant. This is due to the fact that in order for a Pitot tube to be able to measure stagnant pressure, it needs to be pointed directly at the fluid flow. In wind anemometry, the wind direction is constantly changing, so to use a Pitot tube anemometer for this application, it needs to be mounted on a wind vane, thus limiting the time response of the sensor. Fig. 10 shows a Pitot-tube anemometer with a wind vane.

Figure 10 – Pitot-tube anemometer with wind vane

Source: https://the-weather-station.com/types-of-anemometer/, accessed Jan. 2020.

2.3.8 Multi-hole probe anemometers

Multi-hole probes are similar to Pitot tubes in the sense that it uses Bernoulli's principle to measure fluid flow velocity. However, instead of using a Pitot tube to acquire stagnant pressure, it uses multiple holes combined in the same probe in a specific manner to get the stagnant pressure in different directions in order to measure the 3D components of the wind. A multi-hole probe is heavier than a Pitot tube, requires multiple pressure sensors and precise machining in order to be built. This makes a multi-hole probe anemometer system expensive. Fig. 11 shows an example of a probe with 7 holes.

Figure 11 – 7-hole pressure sensor probe

Source: https://www.surreysensors.com/products/probes/, accessed Jan. 2020.

2.3.9 Ground-based remote-sensing wind profilers

The wind profile may be obtained remotely by using ground-based instruments. Those instruments work by emitting and then measuring the Doppler shift of the backscattered acoustic, radio-frequency or laser rays in the atmosphere. The Doppler shift contains information about the radial velocity of the wind. The time lag between emission and reception of the waves determines the distance of the point where the wave was backscattered. This way, it is possible to identify the radial wind speed component at different points along the ray path. Multiple radial wind velocity measurements are taken at different heights and directions to obtain a 3D wind profile. In those systems, often times the same instrument may be configured to obtain the wind profile in different vertical ranges, however, the resolution of the measured profile remains the same. This means that in higher range mode, the sampling volumes are larger (WEISSHAUPT et al., 2018). Those instruments are classified according to the the ray type used, and the particularities of each technology shall be briefly discussed in the following sections. For an in-depth review of these observational techniques, the reader is referred to Banta et al. (2012).

2.3.9.1 LIDAR

Meteorological Light Detection And Ranging (LIDAR) systems use the Doppler shift of light beams backscattered in aerosols suspended in the atmosphere to measure the wind profile. They effectively measure the radial velocity of those aerosols,

which matches the wind speed component in that direction. Multiple measurements from different directions at different heights are taken and combined to obtain a 3D wind profile. LIDAR systems can only operate in conditions with sufficient aerosols in the atmosphere. Its vertical range is limited by the power output of the LASER diode. By comparison with other ground-based remote-sensing instrumentation, LIDAR instruments are more accurate, and have been deployed both at ground level and airborne (LANG; MCKEOGH, 2011). However, LIDAR systems are costly, and cloud or mist may generate non-uniform backscatter which may contaminate significantly the Doppler signal received from aerosol scattering. Fig. 12 shows a meteorological LIDAR capable of measuring the wind profile for heights up to 200 m.

Figure 12 – LIDAR Zephyr ZX300

Source: https://www.campbellsci.com.br/p2546a, accessed in Jan. 2020.

2.3.9.2 SODAR

SODAR (Sonic Detection And Ranging) uses the Doppler shift of acoustic waves backscattered in the atmosphere due to refraction caused by small temperature and/or wind velocity gradients to measure the wind profile. They consist of antennae that transmit and receive acoustic signals and a processing unit that calculates the Doppler shift and the wind speed from those measurements. The vertical range of SODARs is from 0.2 to 2 km, and is determined by the audio signal frequency, its power output, the atmospheric characteristics, such as sound attenuation, turbulence and stability, and the noise environment (EPA, 2002). SODAR systems usually are expensive and heavy, and cannot be embedded in any aircraft due to noise concerns. They are very sensitive to audio noise and low power systems usually have a short measurement

scale. SODAR systems are subject to echoes and may present poor performance while measuring an atmosphere with poor temperature contrast and wind gradient or in rainy conditions. Fig. 13 shows the Triton SODAR, one of the most validated remote sensing systems (DVORAK, 2020).

Figure 13 – Triton SODAR wind profiler

Source: (DVORAK, 2020).

2.3.9.3 RADAR

RADAR (Radio Detection and Ranging) profilers uses electromagnetic (radio frequency) waves, which, in a similar way to SODAR, backscatters due to inhomogeneities in temperature, humidity and wind velocity in the atmosphere. The RADAR wind profilers (RADAR Wind Profiler (RWP)) wavelength must be in the range of the irregularities it is trying to detect (PETERSON et al., 2002). A RWP may register non atmospheric measurements, such as birds, insect, bats and precipitation, as the reflectivity of those targets is greatly superior than the reflectivity of clear air signals. Since those targets are mostly not traveling in the same velocity as of the wind, their presence may present erroneous measurements. The filtration of those signals is possible, but would degradate the system's performance. Still, if correctly configured, RWP is the only ground-based remote-sensing wind profiler that can be used regardless of atmospheric conditions. This is due to the fact that, unlike with SODAR and LIDAR technology, atmospheric phenomena such as fog or precipitation are transparent to the radio frequency waves typically used in RWP. This is advantageous for the RWP in relation to other systems. Another thing to be considered is that there are certain frequency ranges that are restricted or present high interference from other commercial, military or research

instruments. Many parameters need to be considered when setting up a RWP, such as signal wavelength, the latitude and height of its installment, and the seasonal variations in the atmosphere. A good guideline for choosing the adequate RWP system was made by McLaughlin (2014). Fig. 14 presents one of the smallest RWP systems commercially available.

Figure 14 – Small 915MHz phase array wind profiler

Source: https://www.esrl.noaa.gov/psd/data/obs/instruments/WindProfilerDescription.html, accessed Jan. 2020.

2.4 USE OF AIRCRAFT TO MEASURE WIND

Aircraft have been used to measure wind ever since the 1950's (MURGATROYD; HELLIWELL, 1959), however, the usage of UAV in this application has only started in 1970 (KONRAD et al., 1970). Ever since, and specially after 2000, with the popularization of aeromodelism and the development of lighter and smaller meteorological instruments, some unmanned fixed-wing devices have been specifically designed for meteorological purposes (MARTIN et al., 2011; JONASSEN, 2008). The usage of unmanned rotary-wing aircraft for meteorological purposes has been much more recent (PALOMAKI et al., 2017; ETTS et al., 2015; WOLF et al., 2017). In those publications, wind measurement is made without the usage of additional embedded instruments in the aircraft. The aircraft is controlled in a manner as such to maintain its position in relation to an inertial navigation frame. In the presence of wind, in order for the UAV to maintain its position, a slight angular displacement is necessary, in a way such that the lift components may compensate the horizontal drag force of the wind acting on the UAV. By measuring the angular displacement and the lift force from the electric motors,

it is possible to estimate the drag force of the wind acting on the UAV with a model of the UAV dynamics, and finally obtain the wind velocity by means of the drag equation.

The addition of embedded wind sensors in rotary-wing UAV systems for meteorological purposes has only been proposed more recently and it is in preliminary stages of research. An experimental study on the response of wind sensors embedded in rotary wing UAV in a controlled environment is presented by Prudden et al. (2016). In that work, special attention is given to the interference of the wind generated by the propellers in the measurements of wind speed and direction by the embedded sensors. A sensor positioning strategy is proposed and calibration functions are presented in order to perform corrections of the measurement errors introduced by the rotors. In Assireu et al. (2019), the authors proposed that an anemometer may be suspended from a rotary-wing UAV by a 4 m cable in order to take atmospheric wind measurements without them being influenced by the wind generated by the propellers. Two experimental tests were performed, the first using a sonic anemometer and the second using a cup anemometer, in order to evaluate the performance of the system in comparison to a set of industry-standard anemometers located at a nearby tower at different heights. Both experiments showed promising results. However, suspending an anemometer from an UAV may introduce errors in the readings due to the pendulum motion on the payload caused by strong wind conditions or horizontal translation of the UAV. Also, automated take-off and landing procedures are much more complicated in such system. The work presented in Chilson et al. (2012) shows some field experiment results of a rotary-wing UAV with embedded wind measurement sensors. The initial results seemed positive, but the work still needs a more solid methodology in order to objectively evaluate the results in a clearer manner. Besides that, in the prototype presented, the wind sensors are located inside the wind cone of the propellers, which may introduce systematic errors on the wind readings that may significantly alter the measurements taken.

2.5 ACOUSTIC ATMOSPHERIC TOMOGRAPHY AND UAV AS A TOMOGRAPHIC PLATFORM

The use of acoustic atmospheric tomography (AAT) applied in great fluid volumes has been firstly proposed in 1978 (MUNK; WUNSCH, 1979). Since then, a large quantity of ocean tomographic studies has been realized (MUNK et al., 1995). This technique has been applied to acquire, mainly, information about temperature and underwater currents (CORNUELLE et al., 2008) of significant volume transport. The technique applied is analog to those applied in medicine for diagnostic imaging. Acoustic tomography starts from measuring the modifications of acoustic waves caused by varying characteristics of the propagating media. A mathematical model that explains such modifications is proposed and through model inversion, the varying propagating media characteristics are estimated.

When applied to the atmosphere, acoustic tomography comes up initially applied in the context of mapping and locating animals, in Spiesberger and Fristrup (1990). In that work, the author proposes that by measuring the difference between animal vocalizations recorded in different pairs of microphones and using tomographic inversion algorithms, the animal can be located. Even though the intended proposal of the work did not relate to, a certain amount of wind and temperature profiling was present in his analysis, as a form of improving the precision of the obtained results. Later, the first time that the usage of acoustic tomography of the atmosphere was proposed in order to obtain the wind and temperature profile was in Keith Wilson and Thomson (1994). In this case, in a different manner than the one proposed by Spiesberger and Fristrup (1990), the location of the acoustic sources is known and fixed, and not just another variable to be determined.

In Spiesberger and Fristrup (1990), the author estimated deviations in wind temperature and velocity from a reference value along a horizontal plane in the atmosphere. Since then, due to contributions from different groups, the acoustic tomography technique has been significantly enhanced. Those enhancements came by applying better inversion algorithms, new propagation time measurement techniques, and by the proposal of 3D acoustic tomography algorithms. Studies were presented evaluating and validating acoustic tomography techniques in comparison to conventional wind measurement techniques (ZIEMANN, Astrid et al., 2002). The year 2011 was the first time that the AAT technique was proposed to be applied with the aid of an UAV platform (FINN; FRANKLIN, 2011). On UAV-assisted AAT, an acoustic source and a microphone are embedded in the vehicle and a matrix of microphones is spread around on the ground. The UAV then moves along a pre-determined trajectory emitting an acoustic signal while the microphones record the acoustic signal. The trajectory is determined in a way such as the acoustic rays propagating from the acoustic source to the sensors traverse in a sufficiently uniform and dense manner the air volume being studied. The UAV-assisted AAT devices presented since then have been implemented utilizing the sound signature of combustion engines of fixed winged UAVs as the acoustic source (ROGERS, K.; FINN, 2013; ROGERS, K. J.; FINN, 2013; ROGERS, K.; FINN, 2014; ROGERS, K.; FINN, et al., 2013; FINN; ROGERS, K., 2016a, 2016b, 2017). The simultaneous usage of multiple fixed-wing UAVs for AAT has been proposed by Finn et al. (2014). More recently, a detailed comparison of the wind profile measurements obtained by UAV-based AAT with the measurements obtained by a SODAR was presented by Finn et al. (2017).

2.6 LITERATURE REVIEW CONCLUSION

This literature review described the sensors and platforms used in measuring the wind profile in the boundary layer and presented the current state of the research in

regards of the usage of UAVs as a platform for meteorological instruments. Specifically, the instruments used in measuring the wind profile in the atmospheric boundary layer. A methodology has been applied in order to find the references in this area of study upon which this dissertation can be based upon. After this initial survey, an innovative method of measuring the wind profile is proposed in this thesis, using multirotor UAV as a platform for acoustic tomography instead of fixed-wing aircraft. The motivation behind this work is that automatized take-off and landing operation of VTOL (Vertical Lift-Off and Landing) UAVs is simpler than fixed-wing ones. No work of similar scope was found during this review. However, the publications surveyed definitely contribute in many ways with the development of this dissertation.

3 METHODOLOGY

This dissertation is concerned with proposing an automated solution for AWE resource assessment. From the many methods, sensors and platforms presented in Ch. 2, the multirotor-UAV-based AAT device stands as an advantageous alternative that is worth being explored. This chapter focuses on the methods and principles beneath this technique, upon which the experimental setup is proposed in Ch. 4. Based on the works of Kevin Rogers and Finn (2013), V.E. Ostashev et al. (2000) and Vecherin et al. (2006), the AAT setup is presented. The AAT algorithm uses propagation time measurements of a large set of acoustic rays traversing a determinate volume of the atmosphere to estimate the values of air temperature and wind velocity in that volume. In order to analyze and validate the algorithm, simulation is used in this dissertation to generate the input data for the AAT algorithm through atmospheric and sound propagation models, in accordance to the proposed setup. The atmospheric and sound propagation models mentioned above are presented in Secs. 3.1 and 3.2. The algorithms and the simulation tools used to compute the propagation time and perform the AAT are presented in Sec. 3.4.

In what concerns the prototype, sensors and actuators are required to emit and receive the acoustical signals required as inputs for the algorithms. In this chapter, a description of the measurement and instrumentation principles applied in the experimental setup is presented in Sec. 3.3.

3.1 BOUNDARY LAYER WIND PROFILE

Oke (2002) says that often times, the wind velocity, humidity and temperature values vary with height and may be conveniently expressed as a set of functions called *vertical wind profile*. The most significant effect concerning the wind velocity profile near the surface in the absence of strong thermal effects is the frictional drag imposed on the flow by the underlying rigid surface. Therefore, for a neutrally stable atmosphere, i.e. in the absence of strong thermal effects, the wind speed variation with height may be accurately described by the logarithm decay curve:

$$u_Z = \frac{u_*}{\kappa} ln \frac{z}{z_0} \tag{1}$$

Where u_Z is the mean wind speed velocity at the height z, u_* is the friction velocity in ms^{-1}, κ is Von Kárman's constant and z_0 is the roughness length in meters. Another method of representing the variation of wind speed with height is by the power law, generally expressed as:

$$\frac{u_Z}{u_1} = \left(\frac{z}{z_1}\right)^p \tag{2}$$

Where u_1 is the known wind speed at height z_1 and p is an exponential parameter between 0 and 1 and may be determined by wind speed measurements at two known locations:

$$p = \frac{ln\frac{u_1}{u_2}}{ln\frac{z_1}{z_2}} \tag{3}$$

While the wind speed variation with height on the boundary layer may be represented by power or logarithmic laws, usually temperature profiles are much less well behaved. The chaotic weather variations that happens daily and seasonally on sun radiation, wind flow and air properties greatly affects the temperature profile of the atmosphere near surface. Fig. 18.13 of (STULL, 2017, p. 695) exemplifies how differently the temperature profile evolves on different seasons. It should be noted that the temperature profile diverges significantly from what is presented in Fig. 18.13 on different wind, cloud coverage, humidity or atmospheric stability conditions.

3.2 PROPAGATION OF SOUND IN THE ATMOSPHERE

To obtain information about the propagation speed of sound in the atmosphere, the devices used for acoustic tomography of the atmosphere must be equipped with sound sensors and actuators. In this section we discuss the principles of sound propagation in the air, which is essential to design the instrumentation in the prototype.

As stated by V. Ostashev and Wilson (2016, p. 11), the sound speed c_L in a motionless atmosphere is given by:

$$c_L = \sqrt{\gamma R T} \tag{4}$$

Where $\gamma = 1.40$ is the ratio of specific heats (adiabatic index) for dry air, $R = 287.058\,\mathrm{m}^2$ is the gas constant for dry air, $T = T_a(1 + 0.511q)$ is the acoustic temperature, q is the specific humidity and T_a is the dry air temperature in Kelvin. We can observe from Eq. 4 that the sound speed in the atmosphere is affected primarily by the temperature T_a and with a smaller effect, by humidity. The group velocity of a wave in a moving media is represented as (OSTASHEV, V.; WILSON, 2016, p. 72):

$$\vec{U} = c_L(T)n + \vec{V} \tag{5}$$

Here, $\vec{V}$ is the wind velocity vector, n is the unit vector normal to the sound wave front and $\vec{U}$ is the group velocity of a sound wave. The atmosphere is a highly complex and dynamic system, in which its parameters constantly fluctuate due to many different causes that are constantly changing, such as the local topography, weather and wind turbulence. For higher sound frequencies, the combination of the effects caused by an atmosphere with these characteristics on the ray path can be studied

through geometrical acoustics. Those effects may contribute to enhance or diminish the intensity of sound signals at different regions.

As it has been explained in Sec. 3.1, vertical gradients of wind speed and temperature are common in the atmosphere. Those gradients make the sound ray path slightly curved due to the effects of refraction, specially in the section of the atmosphere closer to the surface, where those gradients are more intense. The effects of refraction can be analyzed in terms of Eq. 5 and Eq. 4. From those equations, it can be deduced that positive gradients of temperature, humidity and wind velocity components tangential to the sound path in the vertical profile causes downward refraction in the acoustic ray. Likewise, negative gradients of those physical quantities causes upward refraction.

Acoustic waves in the atmosphere may be subject to effects of reflection. Reflections may happen when the acoustic wave hit an interface between media with different propagation speed. It occurs specially on surfaces such as a nearby walls, trees, buildings, towers and specially the ground. Another phenomena that happens in the atmosphere when the sound waves traverse an interface between media with different propagation speed is scattering.

In a complex atmosphere, there may be multiple paths which a sound wave can travel through from a sound emitter to a receiver. The envelope of ray paths that reaches a receiver from a determinate source is called caustics. Caustics can occur in the atmosphere due to the effects of refraction or reflection of these sound rays. If the travel time of the sound through these multiple paths is different, the signal may be distorted due to the effects of constructive or destructive interference and the receiver may experience echoing.

For a sound wave in the atmosphere emitted from a point source, the wave front travels out with an increasing radius in a spherical shape. As the wave front advances, its surface increases and the sound intensity decreases in an effect called geometric spreading. For spherical propagation, the sound level decreases 6 dB as the distance from the sound source doubles. This relation is valid for propagation in homogeneous media without reflecting surfaces.

As the sound propagates in the atmosphere, its power may be attenuated significantly due to atmospheric absorption. Atmospheric absorption occurs when the sound wave loses energy to the media either in kinetic form, by causing vibration and rotation of the air molecules, or thermal form, by viscous losses due to the friction that happens as air molecules collide with each other. The attenuation in dB due to atmospheric absorption (A_a) of a plane sound wave with intensity S_0 at the origin and intensity S after propagating the distance r in a direction perpendicular to the phase front can be expressed as (BROWN; HALL, 1978, p. 54):

$$A_a = ar = 10 \log_{10} \left(\frac{S_0}{S} \right) \tag{6}$$

Where a is the absorption coefficient in $\mathrm{dB\,m^{-1}}$ and can be determined for pure tones in homogeneous atmosphere as a function of tone frequency, air temperature, pressure and relative humidity. Additional information on how to calculate the atmospheric absorption coefficient can be found in Brown and Hall (1978). High pitched sounds are more attenuated in the atmosphere, and the tone frequency should be carefully determined for a receiver to be able to measure long range sound emissions.

Any sound propagating outdoors is subject to noise, which may come from many different sources and may have different levels and spectral characteristics depending on the ambient in which the receiver is located. An urban or industrial environment during daytime may present very high ambient sound noise, specially in lower frequencies, caused by traffic, industrial, human and other sources. Rural or remote sites may present much lower noise levels, caused by animals, running water, wind and other weather-related phenomena. In wilderness areas, noise may occur in levels as low as 30-40 dB as compared to 55-95 dB in urban areas.

3.3 INSTRUMENTATION

In this section, instrumentation principles behind the devices that are used to emit and receive audio signals in the acoustic tomography device are presented.

3.3.1 Audio

3.3.1.1 Microphones

There are two main types of microphones that can be used to acquire sounds from distant sources, classified according to the method of converting the air pressure variations of a sound wave to electric signals: condenser and dynamic microphones. Both microphones uses diaphragms to convert the air pressure in linear movement.

The diaphragm in a dynamic microphone is connected to a coil suspended in a magnetic field. The movement of the diaphragm generates a variable current on the coil through electromagnetic induction. Dynamic microphones are robust to mechanical shocks and sound signals with high pressure level. However, a single membrane on a dynamic microphone does not respond linearly to different audio frequencies, and multiple membranes may be used combined in a single microphone to enhance the frequency response of the device. Multiple membrane dynamic microphones are usually costly. A simplified schematic of a dynamic microphone is presented in Fig. 15.

On condenser microphones, the diaphragm is physically attached to one of the plates of a capacitor. The vibrations transmitted to one plate varies the distance between the plates which causes a change in the capacitance of the capacitor. The plates of the capacitor are biased with a fixed charge with a Direct Current (DC) circuit with very high resistance resistors. Since the charge in the capacitor is nearly constant

Figure 15 – Simplified drawing of a dynamic microphone

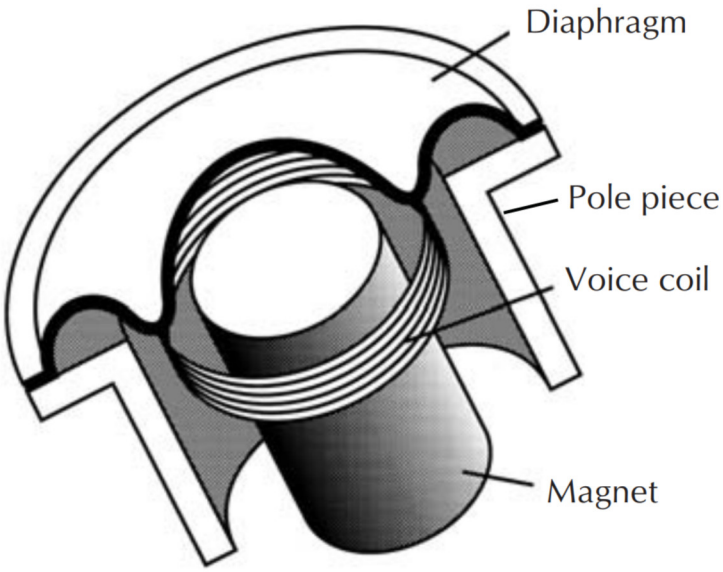

Source: https://service.shure.com/Service/s/article/difference-between-a-dynamic-and-condenser-microphone?language=en_US, accessed May 2020.

for vibrations in audible frequencies, the capacitance changes produce proportional changes in the voltage maintained across the capacitor plates. A high-value resistor is placed in series in order to capture the changes in the voltage on the capacitor. The voltage in the resistor changes in inverse proportion to the capacitance across the capacitor's plates and the signal becomes the feed for the microphone's output. Due to the high-value resistor on the microphone's circuit, the resulting signal has a very high impedance and needs to be fed through a preamplifier active circuit to maintain the microphone's frequency response. The preamplifier circuit is usually embedded inside the microphone case in order to minimize electrostatic and electromagnetic noise and signal loss. The power necessary for the operation of the condenser microphones can be provided internally by a battery or externally. Condenser microphones are usually used in high-fidelity recording setups, and have a frequency response that is much more linear in comparison to dynamic microphones, due specially to the reduced amount of mass dislocated in the diaphragm. A simplified schematic of a condenser microphone is presented in Fig. 16.

A common solution to provide external power to professional audio equipment is to use what is called a *phantom power* supply. A standard balanced microphone line consists of three pins: a ground pin (1) and two others (2 and 3) that contains the microphone signal, which is differential. Phantom power consists of providing a constant voltage (usually of 48 V) through both the audio conductors (pins 2 and 3) to the audio equipment. The voltage on the audio conductors is provided by an external device through two identical value resistors to prevent any contamination to the differential

Figure 16 – Simplified drawing of a condenser microphone

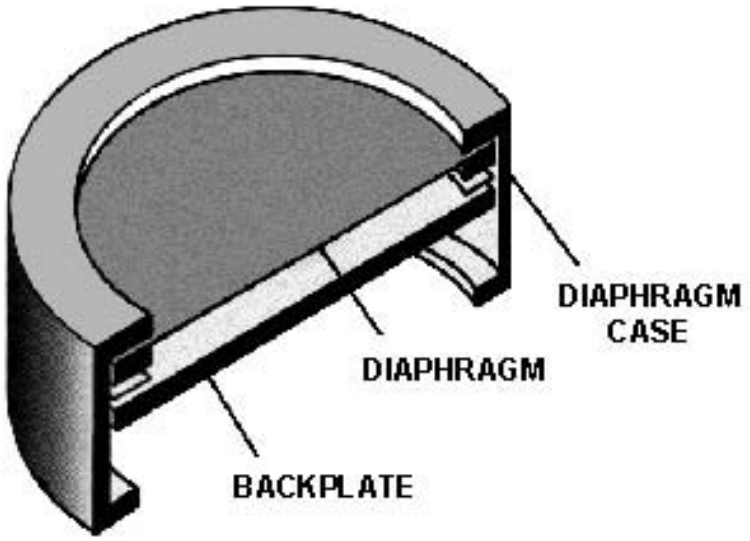

Source: https://service.shure.com/Service/s/article/difference-between-a-dynamic-and-condenser-microphone?language=en_US, accessed May 2020.

audio signal (HUBER; RUNSTEIN, 2014).

In order to dismiss the external bias voltage condenser microphones requires, an electret can be used instead. The electret is a ferroelectric material that has been permanently electrically charged which in turn can be used to provide the static charge needed for the capacitor of a condenser microphone to operate. Although the external bias voltage is not required, an active preamplifier circuit is still needed due to the high impedance characteristic of the generated signal. This preamplifier circuit still requires to be powered. The microphones that uses this technology are called *electret microphones*. They are usually cheaper to fabricate and present a poorer performance in comparison to condenser microphones, but some of the best electret microphones available are equivalent in quality to externally polarized condenser microphones.

Since condenser and electret microphones need external power, the quality of the sound signal acquired can be degraded by noise introduced through the external voltage input. Poor symmetry in the resistors of the phantom power circuit may propagate common mode noise to the differential audio conductors. Moreover, the audio conductors can be subject to varying electromagnetic and electrostatic fields caused by the circuit nearby, which may result in additional noise to the sound signal. Common-mode noise can be reduced by using low-noise power sources, such as batteries, by filtrating the output of the noisy power source or by using higher-quality components in the phantom power circuit. Electromagnetic and electrostatic noise can be mitigated by using armored cable grounded in only one extremity, in order to avoid inductive loops.

Another important characteristic of microphones is its directionality. It relates to

the sensitivity of the microphone to capture sounds arriving from different directions. The many directionality patterns exist due to differences in the construction pattern of microphones, the membrane placement and the exposure of each of the sides of the diaphragm to external pressure variations. A microphone is called omnidirectional when it responds with the same sensitivity to sound waves reaching it from every direction. Otherwise, a microphone can be called uni or bi directional when the sensitivity is enhanced in one or two directions, respectively.

3.3.1.2 Loudspeakers

According to Ballou "A loudspeaker is a device that converts electrical energy into acoustic energy (electroacoustic transducer), or more generally, a system consisting of one or more such devices" (BALLOU, 2008, p. 597). In this section, an overview of the theory behind some of the devices commonly used to produce sounds suitable for acoustic tomography is presented.

3.3.1.2.1 Electrodynamic transducers

These are the most common type of transducers. They consist of a coil suspended inside a magnetic field and attached to a diaphragm. As a time-varying current passes through the coil, it interacts with the magnetic field and vibrates the diaphragm accordingly. The vibration of the diaphragm causes sound waves to radiate. The suspension mechanism has two main purposes: To constrain the movement of the moving parts of the electrodynamic sound transducer, comprising of the coil and the diaphragm, and to restore it to an initial position. This type of transducer is found on its most common version as a cone driver, in which the diaphragm is cone-shaped. One of the issues with this kind of design is that its energy efficiency is very low, usually below 10 %. In this case, energy efficiency is defined as the ratio between the output of energy in acoustic form compared to the electric energy inserted in the system. Another issue is that cone-shaped diaphragms may present breakup modes in lower frequencies which distorts the acoustic signal and the devices need to be carefully designed to avoid such problems. A different issue of loudspeakers with electrodynamic transducers is that in order to generate lower frequencies, larger and heavier devices are necessary. Fig. 17 shows a schematic of an electrodynamic loudspeaker.

3.3.1.2.2 Compression driver

In order to achieve more efficient devices, the air volume that is vibrated by a diaphragm can be partially constrained in a compression chamber with a small opening. This mean that the slow variations in the diaphragm produce a much faster movement in the air particles at the opening of the compression chamber, which in turn makes the

Figure 17 – Electrodynamic loudspeaker schematic

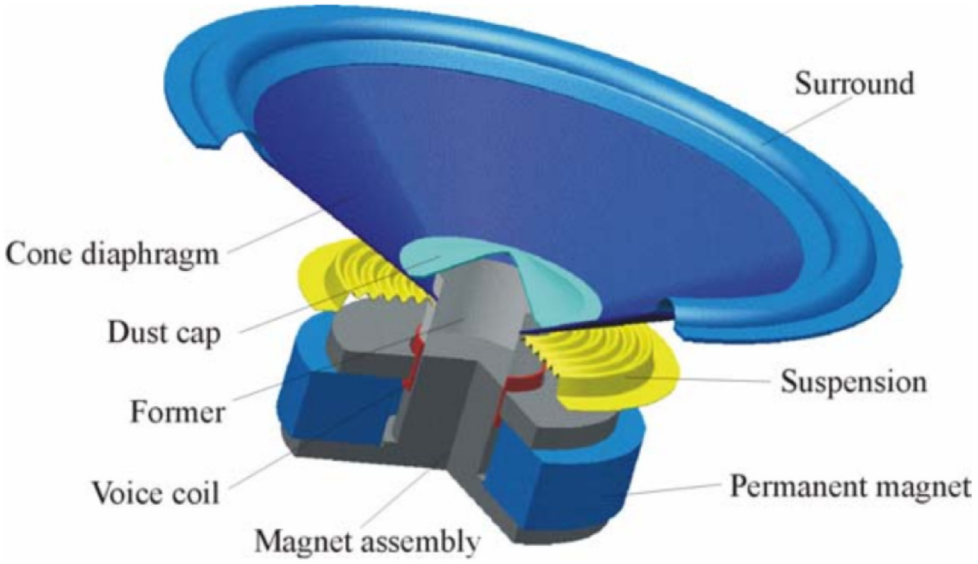

Source: (LANDES et al., 1999).

loudspeaker much more efficient than the standard electrodynamic transducers. A horn is used with its throat attached to the compression's chamber opening to direct and amplify the sound. The compression drivers may be especially prone to acoustic and mechanic resonance, which limits the bandwidth of the loudspeaker. Therefore, a phase plug, which consists of the channels between the diaphragm and the compression cavity, must be designed to minimize such effects. The vibration of the diaphragm in a compression driver is performed in a similar way of the electrodynamic transducer, with a coil immersed in a magnetic field. However, the diaphragm is usually dome or annular-shaped. A schematic of a compression driver is presented in Fig. 18. There is an ample variety of horn shapes which perform differently in respect to sound directivity and amplification. Also, every horn has a lower bound in respect of the frequency of the sound waves it can direct, which is determined by the horn's length, because a wave can only reflect on a surface which is larger than its wavelength. For example, in order to operate with frequencies as low as 100 Hz a horn should have a length of around 4 m, which is unpractical for most applications. Finally, compression drivers and horns introduce significant distortions to the sound signal and are not usually applied in scenarios where sound fidelity is required.

3.3.1.2.3 Electrostatic transducers

Electrostatic transducers work with two pieces of metallic foil placed parallel and separated by a sheet of dielectric as a diaphragm. When an electrostatic charge is applied to the foils, it produces a force between both foils that is proportional to the

Figure 18 – Compression driver schematic

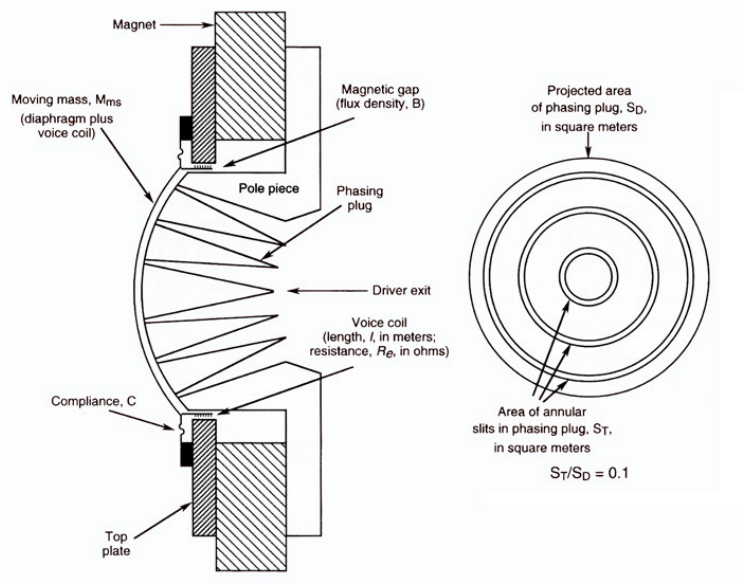

Source: (EARGLE; FOREMAN, 2014, p. 2).

magnitude of the charges. The force is of attraction when the charges have different signs and of repulsion if they have the same sign. If a polarizing voltage is applied to the diaphragm in a way that the foils only experience attraction forces, an Alternating Current (AC) audio signal can be used on top of this to modulate the force and vibrate the diaphragm accordingly. In electrostatic transducers, all of the surface of the diaphragm is subject to the driving forces in a uniform way, which eliminates breakup modes that may be present on other more common cone-shaped diaphragms driven by coils on electrodynamic transducers. This characteristic allows the construction of loudspeakers with larger flat-surfaced diaphragms in comparison to cone-shaped diaphragms in electrodynamic loudspeakers, which in turns improves the directivity of the emitted sound waves, especially at higher frequencies. However, for low frequencies, the output signal has a magnitude which is limited by the amplitude of the diaphragm's movement. Although electrostatic loudspeakers may reproduce sound with very low distortion for mid and high frequencies, usually they are very large, heavy, and expensive. Also, these speakers may not be compatible with most of the amplifiers, which usually are not designed to drive capacitive loads. Fig. 19 shows a schematic of an electrostatic loudspeaker.

3.3.1.2.4 Piezoelectric transducers

A very simple type of speaker can be made by using piezoelectricity. Piezoelectric materials have the capacity of generating a mechanical strain in response of an electric voltage. A piezoelectric speaker consists of a thin disc of a piezoelectric crystal

Figure 19 – Electrostatic loudspeaker schematic

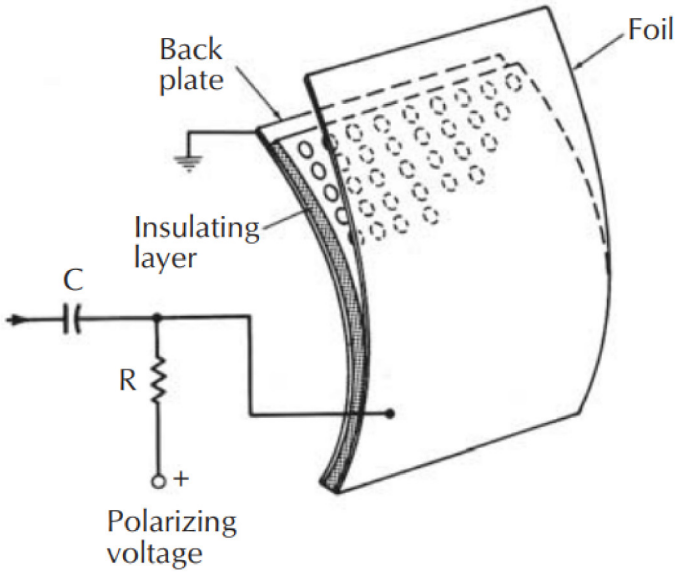

Source: (BALLOU, 2008, p. 603).

to which a voltage audio signal is applied. The voltage produces a vibration in the disc which in turn generate a sound wave accordingly. Since the displacement of the piezo crystals caused by the applied voltage usually is very small, some additional devices may be used in conjunction with a piezo diaphragm to amplify the generated acoustic signal, such as compression chambers or horns. This also makes piezoelectric speakers not a good option to be used in lower frequencies. They have been the standard speaker system used in sonar and ultrasound applications, due to the lack of moving parts which may produce resonance in higher frequencies. Also, piezoelectric speakers resist well the effects of high oxidation environments, such as both fresh and seawater. Piezoelectric speakers are commonly used in buzzers and other small audio devices that may be directly soldered to an electronic circuit board. Also, although the sensitivity of piezo speakers is usually low, due to the high impedance of the piezoelectric materials, the efficiency of such speaker is much higher in respect to the sound pressure output for electrical power input ratio. The piezoelectric speaker is very easy to drive, and can be drived directly by TTL outputs. Fig. 20 shows an example of a piezoelectric transducer.

3.3.2 Ray path definition

A critical input data to the tomography algorithm is the ray path of the acoustic signals. The refraction caused by the gradients of temperature and wind velocity present in the atmosphere makes the path of acoustic signals slightly curved. However, a straight ray model is considered in this paper. This simplification greatly reduces the

Figure 20 – Piezoelectric transducer

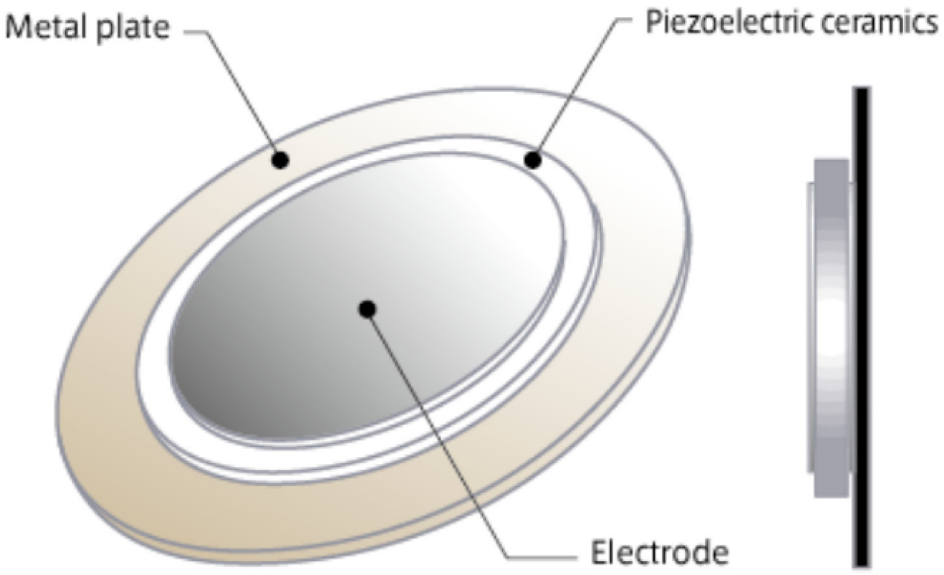

Source: https://product.tdk.com/info/de/products/sensor/level/powder-level/technote/tpo/index.html, accessed Jan. 2020.

complexity of the tomographic algorithm, as a ray tracing algorithm is dismissed. On the other hand, a straight ray model introduces errors in the ray path definition. These errors, as shown in A. Ziemann et al. (1998), may be of 0.2 m for a 200 m distance between source and receiver and decrease for greater distances at a rate that depends on the conditions of the atmosphere. Although in order to deliver accurate reconstructions of target atmospheres an error of <0.01 % of the true path length may be required (FINN; ROGERS, K., 2016b), a tomographic algorithm with curved ray paths is beyond the scope of this paper. For a straight line ray model, the measurement of the position of both the acoustic source and the receiver are sufficient for a full definition of the ray path. In the following sections, an overview of the positioning systems technology considered for the tomography device is presented.

3.3.2.1 Wireless positioning systems

Positioning systems are used to determine the location of an object in space in relation to a determinate coordinate system or reference frame. The reference frames used can be the ones determined by standard conventions or they can be arbitrarily defined for a specific application. The choice of the reference frame is made by convenience. For example, to locate a certain object on Earth, a convenient coordinate system to be used is a global (or geographic) coordinate system. In it, every location is represented with a set of three coordinates, usually called latitude, longitude and elevation. The positioning of a determined object in relation to a global coordinate system

can be obtained with many different ways. Historically, the knowledge and observation of the celestial bodies, compasses and landmarks were used to obtain a global referenced position. Nowadays, modern satellite systems with local receivers are usually employed to locate a certain object with respect to a global coordinate system. A local coordinate system is an arbitrarily established convenient reference frame, attached to another object or landmark from which the relative position is desired to be expressed.

For this dissertation, only the positioning systems and techniques used to locate outdoor flying objects on or near the surface of the earth are of interest. Zekavat and Buehrer (2019) presents fundamental techniques of positioning systems. Below, the techniques relevant to this work are be briefly presented.

3.3.2.1.1 Direction-of-arrival (DOA)

Direction of arrival, or angulation positioning systems use a conjunction of directional sensitive sensors at reference points to find the position of a target object. A position can be obtained by finding the intersection of the lines pointing to the direction indicated by each sensor. For sensors that can provide angular measurements only in relation to one axis, two sensors are required to locate a target object on a coplanar case, and three are necessary for a non-coplanar case (ZEKAVAT; BUEHRER, 2019). The angular sensors often used in this case have a steering mechanism that points their antenna to the direction of peak incoming energy (ZEKAVAT; BUEHRER, 2019). The Direction of Arrival (DOA) of the signal can then be determined by measuring the angles of the steering mechanism when pointing to the signal source. Those sensors are usually costly, complex and have high power consumption (ZEKAVAT; BUEHRER, 2019).

3.3.2.1.2 Time of arrival (TOA)

Time of arrival localization is based on obtaining the distance between a target object and multiple reference points through measuring the propagation time of a wireless signal emitted at the target object and received at the reference points. The localization of a point in a 3D space can be determined by knowing its distance to at least 4 reference points. The distance measurement to one reference point constrains the possible location of an object on space to the surface of a sphere centered in that reference point with a radius equal to the distance measurement. A second distance measurement from a different reference point constrains the possible location of the target object to another sphere. Now, the target object's position is delimited into a circumference defined by the intersection of both spheres. A third distance measurement reduces the set of possible locations to two, determined by the intersection between the circumference and the surface of the sphere centered in the third reference point.

A fourth measurement is required for disambiguation between the last two possible locations. The number of measurements required may be reduced in the case the target object is coplanar or colinear to a subset of the reference points. The direct Time of Arrival (TOA) localization results in two problems (LIU et al., 2007), all nodes in the system need to be precisely synchronized and a timestamp needs to be labeled in the transmitting signal to measure the distance. All of the geometric processing can be done in real-time or post processed, aided by one of the widely researched least-squares algorithms.

3.3.2.1.3 Time difference of arrival (TDOA)

Time difference of arrival localization works in a similar way to TOA, by successively constraining the set of possible target locations using geometrical relations and distance measurements. Instead of spheres, Time Difference of Arrival (TDOA) uses hyperboloids. A signal is emitted from the target source and the TDOA of the received signal between two known reference points is measured. The hyperboloids are formed by the set of points in space that satisfies that TDOA relation (LIU et al., 2007). A 3D target location can then be obtained by the intersection of four of those hyperboloids. The number of hyperboloids a set of N reference points can obtain is defined by the number of different combinations of two elements out of N. It has been determined, according to rigidity theories on positioning systems (PRIYANTHA et al., 2005), that five reference points are necessary to unequivocally determine a 3D location of an object in space. Since noise is present at the distance measurements, iterative algorithms are often used to determine the best possible solution to this problem (TORRIERI, 1984; BUCHER; MISRA, 2001).

3.3.2.1.4 Received signal strength indication (RSSI)

Received Signal Strength Indication (RSSI) systems use lateration techniques to localize the target objects by acquiring the distance readings through measuring the power of a wireless signal received from a reference point. The attenuation of a certain signal measured on a receiver is related to the distance from its source. Theoretical and empirical models of the signal propagation are used to achieve range measurements from the power readings (ZEKAVAT; BUEHRER, 2019). The algorithms used to perform localization are similar to the ones used in TOA applications. Different than TOA or TDOA, RSSI positioning systems can be applied when there is no direct *line-of-sight* (Line Of Sight (LOS)) between emitters and receivers.

3.3.2.2 Inertial navigation systems (INS)

Gyroscopes and accelerometers have been used in many cases as instruments to sense rotational and translational motion with respect to an inertial reference frame (TITTERTON; WESTON, 2004). Based on the laws of classical mechanics formulated by Newton, inertial navigation systems rely on the fact that a body continues to perform a straight line uniform motion, unless an external force is acting on the body. If there is a sensing device capable of measuring the acceleration of the body, which is proportional to the resulting force vector acting on the body, changes in its velocity and position may be calculated by performing successive mathematical integrations with respect to time. For a free body moving in 3D space, the measurements of the acceleration in respect to three perpendicular axes need to be obtained in order to obtain the position of the body. Triaxial accelerometers are usually the instrument employed in such cases. Another important information required for inertial navigation is the direction in which the accelerometers are positioned in relation to the reference frame. Those can also be obtained by mathematical integration of the measurements of the angular motion variations measured by using a triaxial gyroscope. By combining the measurements taken from accelerometers and gyroscopes attached to a certain vehicle, it is possible to obtain its translational motion with relation to a reference frame and thus its position within it. However, all inertial navigation position measurements are subject to drift, which happens due to the successive integration of small errors on the measurements of the sensors over time. These errors, however small they are, when integrated along a sufficiently large time interval, grow significantly. Therefore, to use inertial navigation systems, an additional positioning system need to be used in conjunction to perform periodical corrections. Usually, the inertial navigation systems are used in conjunction with a lower acquisition rate system, such as a Global Navigation Satellite System (GNSS) system, with some sort of sensor fusion algorithm. In this case, the Inertial Navigation System (INS) keeps providing position measurements with greater time resolution during the sampling intervals of the slower GNSS system.

3.4 ALGORITHMS

3.4.1 Simulation platform

The platform where the models, algorithms and data simulated are being run is MATLAB. MATLAB is a complete computing environment developed at university of Colorado. It is widely applied in research all around the world in many diverse areas involving computation. It features a high level programming language with a vast library of mathematical functions for many applications, including control, linear algebra, data processing, statistics and differential equations solving, combining numeric and symbolic computational techniques. MATLAB also has a very convenient way of displaying

data by a set of built-in graphics functions that enables the user to create customizable 2D and 3D plots. It also provides the functionality of integrating its algorithms with other external application and languages such as C.

The MATLAB platform has already been used before to simulate acoustic tomography algorithms by Wiens and Behrens (2009a) and Finn and Franklin (2011). MATLAB is also an environment familiar to the UFSCKite group to run mathematical models, study and simulate control strategies. Therefore, it has been chosen to be the platform where the models and algorithms are run.

3.4.2 Acoustic tomography of the atmosphere

Acoustic tomography is a technique that can be used to estimate the wind velocity vector field and/or temperature scalar field on a certain plane or volume of the atmosphere. It is based on the fact that the propagation speed of an acoustic ray on the atmosphere is dependent on the wind velocity and temperature along its path. By measuring the propagation time of acoustic rays that traverse the desired plane or volume, inverse techniques are used to provide an estimate for the wind velocity vector field and the temperature scalar field of the atmosphere.

3.4.3 Acoustic tomography algorithm

The propagation time of an acoustic wave in the atmosphere along the ray Γ may be determined by the following equation (OSTASHEV, V.; WILSON, 2016, p. 76):

$$\tau = \int_{\Gamma} \frac{1}{\vec{U}} dl \tag{7}$$

It is desired to obtain a linear relationship between the propagation time of a determined acoustic signal of index *i* through the atmosphere and the wind velocity and temperature variations along its ray path. That can be done starting from Eq. 7 and Eq. 5 (OSTASHEV, V.; WILSON, 2016, p. 102), which results in:

$$\tau = \int_{\Gamma} \frac{1}{\left({c_L}^2 + 2c_L n \cdot \vec{V} + |\vec{V}|^2\right)^{1/2}} dl \tag{8}$$

Where $\cdot$ is the scalar product. The integrand in Eq. 8 is a nonlinear expression that relates $c_L(l,t)$ and $\vec{V}(l,t)$, which complicates in a significant manner the solution of the inverse problem. However, a linear relation of τ with the deviations of T and $\vec{V}$ can be obtained. First, by making $c_L = c_0 + \delta c$, the integrand in equation Eq. 8 can be written as:

$$\frac{1}{\vec{U}} = \frac{1}{c_0 \left(1 + \frac{2\delta c}{c_0} + \frac{2n\cdot\vec{V}}{c_0} + \frac{|\vec{V}|^2}{{c_0}^2} + \frac{\delta c^2}{{c_0}^2} + \frac{2\delta c n\cdot\vec{V}}{{c_0}^2}\right)^{1/2}} \tag{9}$$

Then, the terms of order $\left(\frac{\vec{V}}{c_0}\right)^2$ and $\left(\frac{\delta c}{c_0}\right)^2$, which are small, can be ignored (GODIN, 2002; VECHERIN et al., 2006). Next, $\left(1+\frac{2\delta c}{c_0}+\frac{2n\cdot\vec{V}}{c_0}\right)^{-1/2}$ is linearized using first order Taylor's expansion, which results in:

$$\frac{1}{\vec{U}} = 1 - \frac{\delta c}{c_0\left((1+\frac{2\delta c}{c_0}+\frac{2n\cdot\vec{V}}{c0}\right)^{3/2}} - \frac{n\cdot\vec{V}}{c_0\left((1+\frac{2\delta c}{c_0}+\frac{2n\cdot\vec{V}}{c0}\right)^{3/2}} \tag{10}$$

Taking into account that $(\delta c + n\cdot\vec{V})/c_0 << 1$ and making $\vec{V} = \vec{V}_0 + \delta\vec{V}$, the integrand becomes:

$$\frac{1}{\vec{U}} \approx 1 - \frac{\delta c}{c_0} - \frac{n\cdot\vec{V}_0}{c_0} - \frac{n\cdot\delta\vec{V}}{c_0} \tag{11}$$

The expression of the sound speed fluctuations δc can be obtained as a function of δT. That can be achieved by linearizing c_L in Eq. 4 with relation to δT around the point $T = T_0$ and $c_L = c_0$, as follows:

$$c_L = \sqrt{\gamma RT} \approx c_0 + \delta T\frac{\sqrt{RT_0\gamma}}{2T_0} \tag{12}$$

Since $\sqrt{RT_0\Gamma} = c_0$ and c_L can be written as $c_L = c_0 + \delta c$, δc can be expressed as:

$$\delta c = \frac{c_0}{2T_0}\delta T \tag{13}$$

From Eqs. 7, 11 and 13, the following relation for the propagation time of a single acoustic signal is obtained, with the ray Γ being approximated by a straight line of length l_i (VECHERIN et al., 2006):

$$\tau_i = \frac{l_i}{c_0}\left(1 - \frac{\hat{L}_i\cdot\vec{V}_0}{c_0}\right) - \frac{1}{2T_0c_0}\int_\Gamma \delta T(l)_i dl - \frac{\hat{L}_i}{{c_0}^2}\cdot\int_\Gamma \delta\vec{V}(l)_i dl \tag{14}$$

Eq. 14 is linear with respect to the integrals of δT and $\delta\vec{V}$. The variations of temperature and wind velocity on a certain volume of the atmosphere can be reasonably represented by a network of weighed 3D gaussian radial basis functions (RBFs) with their centers uniformly distributed along the volume (WIENS; BEHRENS, 2009b; ROGERS, K.; FINN, 2013). With that, the variations of the temperature and the wind velocity along a straight line ray path *i* that traverses that volume may be represented by the sum of the projections of each weighed RBF *j* along the ray's path. The projection of a single weighed RBF function to the point *l* in a line is denoted by

$$\delta F(l)_{i,j} = W_{Fj}e^{-k{h_{i,j}}^2}e^{-k|l-d_{i,j}|^2} \tag{15}$$

Where $h_{i,j}$ is the shortest distance between the ray path i and the center of the RBF j, $d_{i,j}$ is the distance from the beginning of the ray path i to the orthogonal projection of the center of the RBF j to the ray path i, k is the scaling factor of the RBF and W_{Fj} is the weigh of the RBF j related to quantity F. Thus, the projection of N weighed RBF functions to the sound ray i is

$$\delta F(l)_i = \sum_{j=1}^{N} \delta F(l)_{i,j} \tag{16}$$

The generic function δF can be substituted in Eq. 16 by δT, δV_x, δV_y or δV_z and N by N_{RBF}, where δV_x, δV_y and δV_z are the deviations of the components of the wind velocity along the ray path and N_{RBF} is the number of RBFs in the RBF network. To each of those quantities being modeled in the atmospheric volume, a separate set of weighs describes its variation. Thus, Eq. 16 and Eq. 15 can be used to represent the integrals on Eq. 14 the following manner:

$$\int_{\Gamma} \delta F(l)_i dl = \sum_{j=1}^{N_{RBF}} \Omega_{i,j} W_{Fj} = \mathbf{\Omega_i} \cdot \mathbf{W_F} \tag{17}$$

$$\Omega_{i,j} = e^{-k h_{i,j}{}^2} \sqrt{\frac{\pi}{k}} \left(\mathrm{erf}(l_i - d_{i,j}) - \mathrm{erf}(-d_{i,j}) \right) / 2 \tag{18}$$

Where erf is the Gauss error function, $\mathbf{W_F}$ is a column array containing the weighs of all of the RBFs related to quantity F and $\mathbf{\Omega_i}$ is a column array containing the projection of every RBF at the ray path i. Eq. 14 and Eq. 17 can then be represented as

$$\frac{\mathbf{L}}{c_0} - \boldsymbol{\tau} = \frac{\begin{bmatrix} \mathbf{L}_x & \mathbf{L}_y & \mathbf{L}_z \end{bmatrix}}{{c_0}^2} \vec{V}_0 + \frac{\mathbf{\Omega}}{2 T_0 c_0} \mathbf{W_T} + \frac{\mathbf{D}(\mathbf{L}_x)\mathbf{\Omega}}{{c_0}^2} \mathbf{W_{V}}_x + \frac{\mathbf{D}(\mathbf{L}_y)\mathbf{\Omega}}{{c_0}^2} \mathbf{W_{V}}_y + \frac{\mathbf{D}(\mathbf{L}_z)\mathbf{\Omega}}{{c_0}^2} \mathbf{W_{V}}_z \tag{19}$$

Where $\mathbf{L}$ is a column array that contains the length of each ray and $\boldsymbol{\tau}$ is a column array that contains the propagation time of each ray. $\mathbf{L}_x$, $\mathbf{L}_y$ and $\mathbf{L}_z$ are column arrays that contains the x, y and z components of the vector pointing from the acoustic source to the receiver ($l_i \hat{L}_i$) for every ray. Those column arrays are of size $N_R \times 1$ where N_R is the total number of ray paths. $\mathbf{\Omega}$ is a matrix of size $N_R \times N_{RBF}$ containing the projection of every RBF on each ray path. $\mathbf{W_T}$, $\mathbf{W_{V}}_x$, $\mathbf{W_{V}}_y$ and $\mathbf{W_{V}}_z$ are column arrays of size $N_{RBF} \times 1$ that contain the weighs of the RBFs for the properties δT, δV_x, δV_y and δV_z of the atmosphere. $\mathbf{D}(v)$ returns a diagonal matrix with elements of v in the main diagonal.

3.4.3.1 Estimation of the deviations

Assuming the estimates for the mean values $\vec{V}_0$, T_0 and c_0 is known, Eq. 19 can be rearranged to:

$$-\boldsymbol{\tau} + \frac{\mathbf{L}}{c_0} - \frac{\begin{bmatrix}\mathbf{L}_x & \mathbf{L}_y & \mathbf{L}_z\end{bmatrix}}{{c_0}^2}\vec{V}_0 = \frac{\boldsymbol{\Omega}}{2T_0c_0}\mathbf{W_T} + \frac{\mathbf{D}(\mathbf{L}_x)\boldsymbol{\Omega}}{{c_0}^2}\mathbf{W_{V}}_x + \frac{\mathbf{D}(\mathbf{L}_y)\boldsymbol{\Omega}}{{c_0}^2}\mathbf{W_{V}}_y + \frac{\mathbf{D}(\mathbf{L}_z)\boldsymbol{\Omega}}{{c_0}^2}\mathbf{W_{V}}_z \quad (20)$$

and then stacked, which results in:

$$\mathbf{d} = \boldsymbol{\Phi}\mathbf{W} \quad (21)$$

Where $\mathbf{W}$ is a matrix of size $4N_{RBF} \times 1$ and $\boldsymbol{\Phi}$ is a matrix of size $N_R \times 4N_{RBF}$. They are defined as:

$$\mathbf{W} = \begin{bmatrix}\mathbf{W_T}^T & \mathbf{W_{V}}_x{}^T & \mathbf{W_{V}}_y{}^T & \mathbf{W_{V}}_z{}^T\end{bmatrix}^T \quad (22)$$

$$\boldsymbol{\Phi} = \begin{bmatrix}\frac{\boldsymbol{\Omega}}{2T_0c_0} & \frac{\mathbf{D}(\mathbf{L}_x)\boldsymbol{\Omega}}{{c_0}^2} & \frac{\mathbf{D}(\mathbf{L}_y)\boldsymbol{\Omega}}{{c_0}^2} & \frac{\mathbf{D}(\mathbf{L}_z)\boldsymbol{\Omega}}{{c_0}^2}\end{bmatrix} \quad (23)$$

$$\mathbf{d} = -\boldsymbol{\tau} + \frac{\mathbf{L}}{c_0} - \frac{[\mathbf{L}_x \;\; \mathbf{L}_y \;\; \mathbf{L}_z]}{{c_0}^2}\vec{V}_0 \quad (24)$$

Acoustic tomography consists of an inverse problem, where the parameters $\mathbf{W}$ of an atmosphere model are desired to be obtained from the data array $\mathbf{d}$ which contains the information of the measurements of the propagation time of the sound rays through the atmosphere. That is accomplished by finding the inverse mapping given by the Moore-Penrose pseudoinverse of $\boldsymbol{\Phi}$ which provides the optimal solutions to the least-squares problem. This is a high cost operation both in memory and computational complexity, and other less-costly algorithms have been proposed in order to solve the inverse problem (JOVANOVIC, 2008), but those are not be explored in this thesis, for simplicity reasons.

The inverse algorithm receives as input the deviations from the average propagation time along the path of each acoustic ray, namely $\mathbf{d}$. That information is obtained from measurements of the propagation time and the length and direction of the acoustic ray, which is assumed to be a straight line from the acoustic emitter to the receiver. It outputs the solution that minimizes the square error of Eq. 22 which is a vector that contains the weighs of a matrix of RBFs that describes the wind velocity and temperature of the atmosphere on the evaluated volume. The distribution and scaling factors of the RBFs are pre-determined. For additional information on RBFs center determination, scaling factor and weigh computing methods, the reader is referred to Schaback (2007).

3.4.3.2 Estimation of the mean values

In order to estimate the mean values for $\vec{V}_0$, T_0 and c_0, a linear relation can be obtained based in Eq. 14 (VECHERIN et al., 2006). First, the integrals in Eq. 14, representing the deviations of the propagation time caused by fluctuations in temperature and wind velocity from the mean values should be set to zero. By doing so and rearranging the terms, the following equation is obtained for a single ray path:

$$\frac{\tau_i}{l_i} = \frac{1}{c_0} - \frac{\hat{L}_i \cdot \vec{V}_0}{{c_0}^2} \tag{25}$$

This equation can be stacked for every ray path i and rewritten in the following manner:

$$\mathbf{Gp} = \mathbf{b} \tag{26}$$

$$\mathbf{G} = \left[\mathbf{J}_{N_R} \;\; \hat{\mathbf{L}}_x \;\; \hat{\mathbf{L}}_y \;\; \hat{\mathbf{L}}_z\right] \tag{27}$$

$$\mathbf{p} = \left[\frac{1}{c_0} \;\; \frac{V_{0x}}{{c_0}^2} \;\; \frac{V_{0y}}{{c_0}^2} \;\; \frac{V_{0z}}{{c_0}^2}\right] \tag{28}$$

Where $\mathbf{J}_{N_R}$ is a column array of ones with length N_R and $\mathbf{b}$ is a column array where $b_i = \frac{\tau_i}{l_i}$. $\hat{\mathbf{L}}_x$, $\hat{\mathbf{L}}_y$. $\hat{\mathbf{L}}_z$ are column arrays containing the components of the unitary vectors pointing in the ray path direction for every ray. V_{0x}, V_{0y} and V_{0z} are the x, y and z components of $\vec{V}_0$.

Eq. 26 provides a linear system from which the values of $\mathbf{p}$ can be estimated using a least square algorithm. The observation array $\mathbf{b}$ is composed by propagation time and ray path measurements. From the values of $\mathbf{p}$, the values of c_0 and $\vec{V}_0$ can be derived. The value for T_0 can be obtained from c_0 using Eq. 4.

3.4.4 Propagation time measurement

One of the input data of the acoustic atmosphere tomography algorithm is the propagation time of acoustic rays through the atmosphere. To obtain those measurements, short pulses of rectangular waves are sent by the siren located in the UAV. In this section, the method used to measure the propagation time of each pulse is presented.

3.4.4.1 Cross-correlation

Cross-correlation is a technique widely used along acoustic tomographic algorithms to determine the time-of-flights of acoustic signals (ZIEMANN, Astrid et al., 1998).

This technique provides a measurement of the similarity between two signals as a function of the delay between them. For two discrete signals x and y, the cross-correlation R_{xy} between them is described using the following formula:

$$R_{xy}[n] = \sum_{m=-\infty}^{\infty} \overline{x[m]} y[m+n] \tag{29}$$

In order to obtain the propagation time of a single pulse, the cross-correlation function is applied between the signal recorded by the receiver and a pre-recording of a pulse sent by the transmitter. A series of distinct peaks in the function is expected at delay times that are related to the time-of-flight of each acoustic pulse. To obtain the correct measurement time of the delay times, a peak detection algorithm is used (ZHANG; WU, 2006). Other smaller correlation peaks may appear due to the periodic characteristic of the signal, caustic rays, or non-linearities, and the peak detection algorithm should be set to ignore them. As expected, the sound signal characteristics, such as its bandwidth, signal to noise ratio, central frequency and pulse duration greatly influence the error of the estimated delay obtained by the cross-correlation algorithm. An empirical analysis on how these parameters influence the output of the cross-correlation algorithm is presented by Ash and Moses (2005).

3.5 METHODOLOGY CONCLUSION

This chapter presented the methods from which the experimental setup is constructed and presented in Ch. 4. The model of the boundary layer wind profile presented is used as the basis for the atmosphere simulation presented in the next chapter. The sound propagation model presented contains the principles behind the algorithms used to simulate the effects of temperature and wind on the propagation time sound rays traversing the atmosphere. It also contains the fundamental equations upon which the AAT algorithms are based on. The AAT algorithms are present in the simulation presented in Ch. 4 to reconstruct the wind and temperature profile of the atmosphere. The time delay estimation technique presented in this chapter is the data processing algorithm that extracts the time of propagation of the sound rays from the audio information received the sensors which is fed to the AAT reconstruction algorithms.

The principles of instrumentation behind the audio sensor and actuator technology currently available were presented. Those principles aided the design process of the prototype hardware presented in Ch. 4. An overview of the theory of positioning and navigation systems was presented, and contributed to the choice of the instrumentation used to define the trajectory of the acoustic rays in the prototype.

4 EXPERIMENTAL SETUP

To get a working prototype of an UAV assisted tomography device, an extensive amount of simulation and experimental work is required. This chapter aims to describe the simulation and experimental setup designed in order to test and validate the algorithms and instruments that compose the subsystems of the tomography device. First the system architecture is presented in two parts, hardware and software. After that, a section is dedicated to the simulation, which is the chosen method to validate the algorithms in this work. In Sec. 4.2, the assumptions and the structure of the simulation algorithm are described.

4.1 SYSTEM ARCHITECTURE

The main functionality expected of the acoustic tomography device proposed in this dissertation is to estimate the wind speed and temperature profiles of a determinate volume of the atmosphere. That is accomplished in this system by measuring the propagation speed of sound rays traversing that atmosphere volume and processing the measurements with a series of algorithms. The next sections are dedicated to explain the general structure of the hardware and software subsystems designed to realize these functions.

4.1.1 Hardware architecture

In order to measure the propagation speed of sound rays in the atmosphere, this work proposes to embed a loudspeaker system in a payload of a VTOL UAV and record the emitted audio signal in a matrix of microphones located in ground modules spread on the ground. A time-delay algorithm can then be used to determine the delay between the signal in the source and in the receiver, which corresponds to the propagation time. The details regarding the choice of the UAV platform used are discussed in Sec. 4.1.1.1. The instruments and signal processing systems involved in the tomography operation can be separated in two parts. The part carried by the UAV is called the payload module and the part located on the ground with the microphones is called the ground module. The system is built in a way where multiple payload and ground modules can be employed. The subsystems in the payload and ground modules and their arrangement are discussed in Sec. 4.1.1.2 and 4.1.1.3.

4.1.1.1 UAV platform

This dissertation presents a rotary wing UAV as a platform for acoustic tomography of the atmosphere.

A multirotor UAV is a convenient choice of platform because of the many closed systems commercially available with an accessible price which can be easily programmed to perform periodic missions with pre-determined trajectories. Sensors and actuators can be embedded on the UAV without the need to program or modify the UAV system by using small microcontrollers or embedded Linux platforms to interface with the sensors and actuators. Sensors, actuators and the processing unit can be powered either by an additional battery on the UAV's payload or by the UAV battery without a significant decrease of flight time, because of the small estimated weight and power requirements of the embedded components in relation to medium and large UAV systems (40+ cm frame, 4+ rotors). Those systems are able to fly to heights of 1 km and above and maintain stable flight in the presence of moderate wind gusts with a flight time around 25 minutes.

A desirable functionality of a VTOL UAV platform for wind resource assessment is the possibility of operation in non-ideal weather conditions. The operation of drones in rain condition is not advised by the manufacturers of most of the commercially available devices. If a wind resource assessment system cannot operate under rain, a lot of gaps in the measurements are expected. This is very undesirable, as the analysis on wind assessment is performed on a time series and the presence of gaps in the data makes this process difficult. Therefore, a weatherproof device is desirable, and a few off-the-shelf UAV systems can be found with these characteristics.

4.1.1.1.1 Charging pad

Another advantage in the use of VTOL UAV is the possibility of automatic recharging the batteries. If the system is equipped with a precision landing system, which is usually based on computer vision or precision positioning technologies, such as Real-Time Kinematic (RTK), as described in 3.3.2.1, an automatic charging pad can be used. The charging pad systems commercially available are based on either wireless technologies based on inductive power transfer or by contact (see Tab. 1). Usually, inductive power charging solutions operate with limited electric current, which makes the battery charging process slow, which in turn increases the dead time of the system. Thus, the contact-based charging pads present themselves as the best alternative available to autonomously charge the device proposed in this dissertation. As for the precision landing system required, since an RTK/PPK system is already expected to be embedded in the UAV payload, the UAV system must be able to use it to navigate. This means that the flight controller of the UAV system must allow such kind of integration. This is an important requirement for the UAV platform, because many Ready To Fly (RTF) systems have closed proprietary firmware that does not allow such modifications.

Table 1 – Charging pad technology

Technology	Company name	URL
Inductive charging pads	Wibotic	https://www.wibotic.com/
	Wipo	https://www.wipo-wirelesspower.com/
	Witricity	https://witricity.com/
Contact charging pads	Skysense	https://www.skysense.co
	Edronic	http://www.edronic.com/
	Heisha	http://www.heishatech.com/

4.1.1.2 Payload module

The payload module has two main functionalities. The first is to emit a determinate sound signature at fixed intervals in a way that it can be measured by a matrix of microphones on the ground. The second is to precisely acquire the position of the payload and timestamp the moment the sound signal is emitted. In order to achieve this, a series of devices are applied, which are described next. The payload module is designed to be self-contained. None of the payload subsystems require anything from the UAV plaftorm, such as power, processing or communication. This design choice makes the test of the payload modules in laboratory simple, and reduces the requirements of the UAV platforms, since no software and hardware integration is required.

A loudspeaker is required to emit the sound. A simple microcontroller is used to control the sound pulse signature. A Linux embedded system is used to control and register the timestamp of the activation times of the loudspeaker, to synchronize to an external clock reference, to communicate and to manage the system operation in a high level. To precisely measure the position of the drone in activation times, two positioning systems are used. The first is based on travel time multilateration with Radio Frequency (RF) and the second is an RTK/PPK GNSS positioning system. A set of auxiliary subsystems is required to power all of those devices. The subsystems described in this paragraph are all located in the payload module and are described in details as follows. Fig. 21 shows the ground module assembly at the moment of publication of this dissertation.

4.1.1.2.1 Loudspeaker

The UAV-Based Acoustic tomography system proposed by Finn and Franklin (2011) uses the sound signature of combustion engines for acoustic tomography. Since the electric motors of the UAV used in this dissertation do not emit enough acoustic energy, a 100 g, 4 W piezoelectric siren with a compression chamber is used as the sound source for the acoustic tomography. Between the available loudspeaker options, presented in Sec. 3.3.1.2, the piezoelectric transducer presents itself as a good option due to the fact that it has high power efficiency, low weight, can be used to emit

Figure 21 – Payload module.

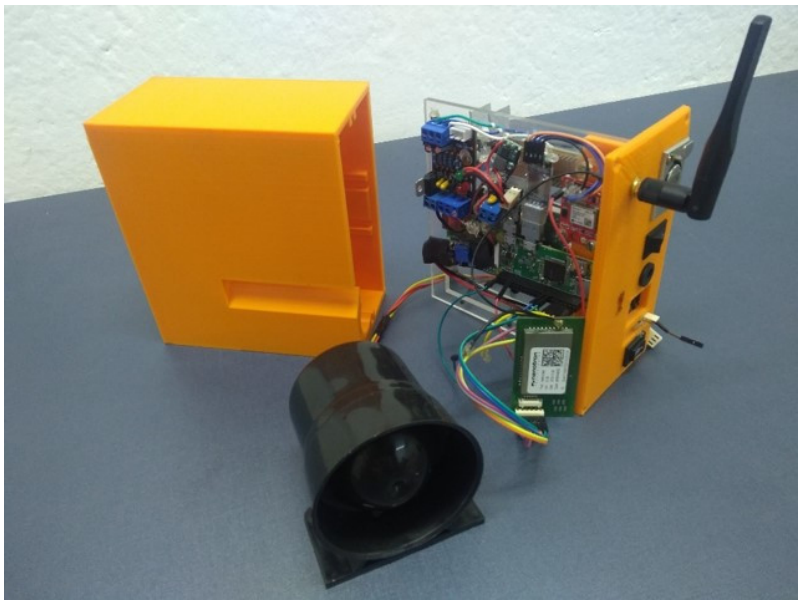

Source: Own elaboration.

sound in the desired frequency range and requires simple driving circuit. The siren chosen produces a signal of 100 dB pressure at 1 m distance with the main frequency components in the 2-2.6 kHz range. The effects of atmospheric sound absorption and attenuation are not expected to lower the Signal-to-Noise Ratio (SNR) of a signal with these characteristics in a significant way for the considered flight path, as explained in Sec. 3.2.

4.1.1.2.2 Linux embedded system

The usage of a multi-task, open source Operating System (OS) board embedded in the payload is convenient for this application. Most embedded Linux boards contain a stable, highly customizable operating system, with a large support from the community. The Linux OS platform allows the usage of open source software, libraries and protocols, which in turn may speed up significantly the software development. There is also many available embedded Linux boards with multiple standard interfaces to connect sensors, actuators and other systems, which makes those boards highly versatile, which is also advantageous for the development phase. A Linux embedded board can be operated remotely, without the need of external modules or peripheral devices, through network or a Universal Synchronous Asynchronous Receiver Transmitter (USART) interface. This functionality is ideal for field applications. Many cheap lightweight options of Linux-based embedded operating system are commercially available. The fact that Linux-based Operating System (OS) are not real-time is not expected to hinder this application

in any significant way, because there is no hard time constraints on the functions that need to be executed by the OS.

4.1.1.2.3 Synchronization system

The measurements of the propagation time of sound should be made with as minimum uncertainties as possible to reduce the estimation errors of the acoustic tomography errors. The technique used in this dissertation consists of comparing the timestamp of the transmission of the sound pulse, made in the payload module, with the reception time of the sound pulse in the ground module. Since timestamp values in distributed devices are being compared, the systems need to be synchronized. A simple way of achieving this is by synchronizing the nodes of the system to an external reference clock that must be accessible to both nodes. The synchronization method proposed in this dissertation consists of using the atomic clocks present in the GNSS satellites that are made available through cheap GNSS receivers as the reference clocks for every node of the system. The GNSS receiver, however, must provide an accurate PPS (*pulse per second*) signal which marks the beginning of the second indicated by the timestamp of the GNSS message. With the GNSS messages and the Pulse-Per-Second (PPS) signal, the Network Time Protocol (NTP) driver protocol running on the Linux embedded system can be configured to continuously correct the system's local software clock accordingly. With this setup, a synchronization to a stratum-0 reference clock may be achieved with offset and jitter values consistently under 20 µs (SCHMIDT, R. E., 2020).

4.1.1.2.4 Multilateration RF positioning system

Radio-Frequency (RF) transceivers may be used to acquire the position of the UAV through different techniques. The one explored in this dissertation is the multilateration technique. This choice of positioning system and method is due to its reliability with simple and inexpensive hardware, ease of implementation, and scalability, in comparison to other approaches (SCHMIDT, E., 2017). In order to precisely determine the position of a given transceiver, the multilateration technique requires the distance measurements from 4 anchors with known positions.

4.1.1.2.5 RTK/PPK positioning system

The most common outdoor positioning systems used nowadays are based on satellite technologies, or shortly GNSS (Global Navigation Satellite System). A GNSS device receives radio signals from a constellation of satellites orbiting the Earth. Each signal provides information about the distance between the satellite and the receiver,

the travel time of the signal and the orbital location of the satellite. Based on a TOA technique, described in 3.3.2.1, the position of the GNSS receiver can be computed. Autonomously operating, single-frequency GNSS receivers have a typical position accuracy in the range of meters (TOMAŠTÍK et al., 2019). Systems that require higher precision have been adopting differential GNSS solutions that require two receivers. One in a base station, in a known location, used to provide corrections to the measurements taken by another receiver located in a rover station, which in this case is the UAV. The corrections on the rover positions can be made in real time (Real-Time Kinematic (RTK)) or be post-processed (Post-Processed Kinematic (PPK)). Some Continuously Operating Reference Stations (CORSs) provide service correction data online in real time for local rover stations. The correction data history provided from CORS may also be accessed to correct previously acquired rover GNSS locations. This makes the usage of RTK/PPK technologies readily available wherever CORS services can be accessed. RTK/PPK systems can achieve horizontal positioning measurements with standard deviations under 5 cm and vertical positioning measurements with standard deviations under 10 cm (TOMAŠTÍK et al., 2019). However, GNSS positioning systems present some disadvantages. The signals received from the satellite constellation are affected by a varying time-delay and phase shift due to the different movement and position of the sources (GLEASON; GEBRE-EGZIABHER, 2009). The satellite constellation may not be accessible depending on meteorological conditions and location and the GNSS information is provided only once every second. This is a problem when the precise location is needed for events happening in the intervals between the data acquisition instants. An interpolation is necessary to estimate the position in such cases.

4.1.1.2.6 Strapdown inertial navigation system (INS)

Strapdown INS systems are composed by three orthogonal Micro Electro Mechanical systems (MEMS) accelerometers, gyroscopes and magnetometers to provide positioning estimates, as presented in 3.3.2.1. The measurements obtained, however, are subject to noise and present integration drift, which becomes significant the longer the system is running. However, INS systems remain suitable to supplement other positioning systems and improve the quality of the combined measurement.

4.1.1.2.7 Payload module power management

In order to power all subsystems inside the payload module in a self-contained way, a battery is necessary. The most widely used batteries in portable and mobile electronic devices nowadays are Li-ion (DENG et al., 2009). According to Deng (2015), Li-ion batteries stand out from other commercially available secondary batteries for a

number of reasons. They have higher voltage, gravimetric and volumetric energy density. They can be fabricated in many different shapes, forms and sizes, which makes them suitable for space constrained portable devices. They do not suffer from memory effect. They also present low self-discharge rate.

The two cathodes most widely used in Li-ion batteries are $LiCoO_2$ and $LiFePO_4$, due to their longer cycle life. According to Deng (2015), $LiCoO_2$ batteries present higher energy density, conductivity and capacity, but are more expensive, have higher environmental impact, are less stable, safe and temperature tolerant than $LiFePO_4$ batteries. Another advantage of $LiFePO_4$ batteries is that they have longer cycle and calendar lifes. BL Series (2020) says that "After one year on the shelf, a $LiFePO_4$ cell typically has approximately the same energy density as a LiCoO2 Li-ion cell, because of LFP's [$LiFePO_4$] slower decline of energy density".

Thus, mainly due to the cycle and calendar life issues, the battery chosen to power the payload module is a single $LiFePO_4$ cell.

In order to provide the required voltage for the 12 V siren and the rest of the subsystems, which are Universal Serial Bus (USB)-powered, a two stage power supply circuit is required. The initial stage is comprised of a switching boost converter, raising the battery cell voltage to 12 V. From that stage, two step-down buck regulators are used to regulate the voltage to 5 V. One to power the Linux embedded system and the RF transceiver, one to power the RTK/PPK positioning system and the microcontroller controlling the driving signal of the siren.

4.1.1.3 Ground modules

The ground module has three main functionalities. The first one is to record the audio signals emitted by the payload module. The second one is to collect a correct timestamp of the moment the recording starts. Finally, the ground module has the functionality of commanding, housing and powering the RF transceivers used to locate the UAV. The devices used to perform these functionalities are described in the following paragraphs. The ground modules are positioned on the ground, at a certain distance from each other. The use of cables inserts limitations to the positioning of the ground modules. This is undesirable, specially during field experiments, where the optimal ground module positioning is being tested. A self-contained design is also advantageous for the ground modules.

To record the audio, a microphone is the sensor of choice. The analog to digital converter is contained in an audio interface which is commanded by an operating system. The operating system, together with an external synchronization subsystem may be configured to register precise timestamps. To provide power to all of those subsystems, a power supply subsystem is required. The Linux embedded system, the synchronization system and the multilateration RF system have the same functionalities

as described in 4.1.1.2, and the solutions chosen in the design process in principle can be applied in both modules. Fig. 22 shows the ground module assembly at the moment of publication of this dissertation.

Figure 22 – Ground module

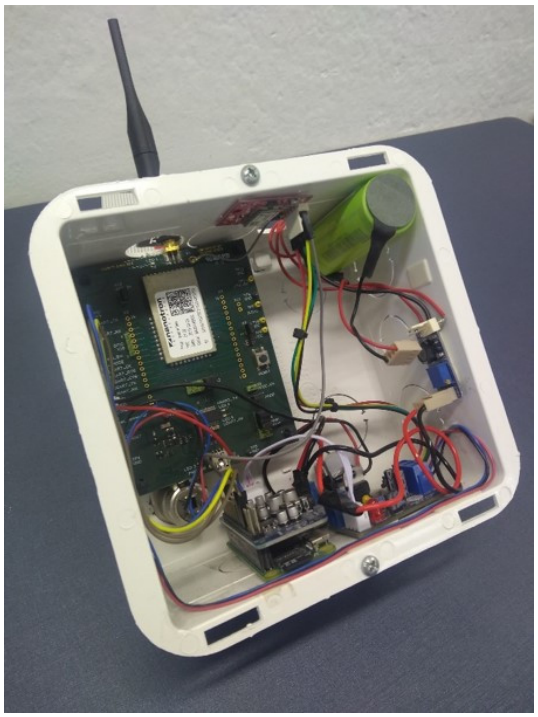

Source: Own elaboration. Microphone is not in the figure, but during experiments, it is plugged to the frame of the module.

4.1.1.3.1 Sound receivers

The acoustic signal captured by the microphones located on the ground modules is expected to be distorted and with noise introduced by the local environment where the system is placed. For sharper peaks in the cross-correlation function, the audio acquisition system should not introduce significant additional noise and distortion to the signal. Hence, a low-noise, omnidirectional and linear microphone is required. As presented in Sec. 3.3.1.1, an electret condenser microphone is a good choice for sensor in this application. Some low-cost microphone models with those characteristics made to perform frequency spectrum analysis of sound systems in closed or open environments are commercially available in the market. These type of sensors require an external power source for the amplification circuit, but that can be provided by a dedicated battery system. A dedicated battery is advantageous because otherwise the common-mode noise introduced due to load variations caused by the digital systems being powered in parallel would degrade the microphone's measured signal.

4.1.1.3.2 Audio interface

An audio interface is used to interface any audio input or output to an operating system. An audio interface allows the usage of open source software to play and record audio in a Linux environment. A model with high acquisition rate and resolution and a clock signal with jitter control can provide high quality audio input for a Linux embedded system that does not provide such functionality.

4.1.1.3.3 Ground module power management

The ground module requires a power supply system different than the one in the payload module. A single $LiFePO_4$ cathode battery cell is used as the power source for the system. The phantom power circuit for the sound receiver is being powered by a dedicated battery pack. All of the other subsystems in the ground module (Linux embedded board, synchronization, multilateration, audio interface) are powered by a 5 V DC source. Hence, a simple boost converter can be used to provide the supply needed for the ground module.

4.1.2 Software architecture

To properly estimate the wind profile, a series of algorithms are employed. The information provided from the hardware is processed through a software chain. The payload module provides sound pulses identified by timestamps. The audio files recorded by the ground modules serve as an input for a Cross-Correlation Algorithm (CCA) that provides time-delay estimations for every sound pulse ray emitted by the payload module and recorded by each of the ground modules. The audio recordings are also accompanied by a timestamp indicating the moment the audio recording started. By comparing the time-delay estimation outputs from the CCA with the timestamp of the audio signal, the propagation time for each sound ray can be obtained. Separately, the localization system provides the location of the payload module at every pulse event. The usage of multiple localization systems can be combined using a sensor fusion algorithms, such as *extended Kalman filters*. However, the development of such algorithms is outside the scope of this work. The timestamp of the sound pulse event and the location of the payload module at that instant are combined with the propagation time of every sound ray to form a triplet. Those triplets are the input of the acoustic atmospheric tomography algorithm. Fig. 23 shows in a schematic how the different algorithms are arranged in order to provide an estimation of the wind profile, as proposed in Sec. 1.2. The general aspects of the software algorithms are discussed in Sec. 3.4 and the details on their implementations on the experiments are presented in Sec. 4.2.

Figure 23 – Software architecture

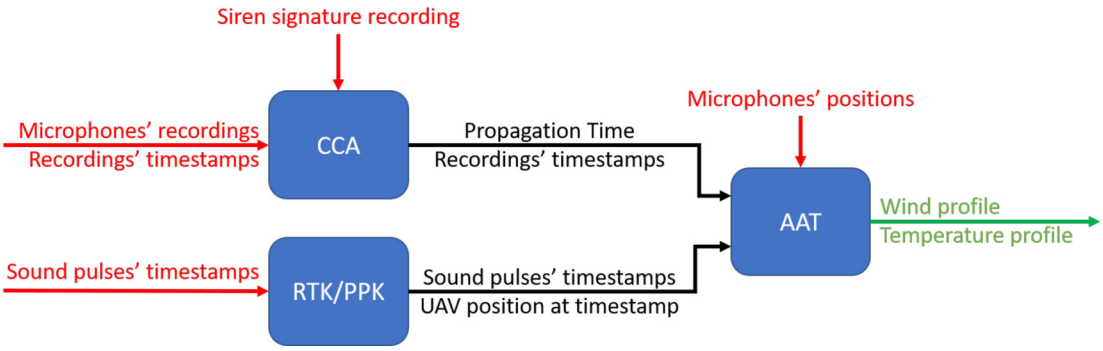

Source: Own elaboration. The inputs are highlighted in red color, the output in green and the main subsystems that compose the software are highlighted in blue. Cross-Correlation Algorithm (CCA) stands for Cross-Correlation Algorithm. RTK/PPK is the positioning system (see Sec. 4.1.1.2). AAT is the Acoustic Atmospheric Tomography algorithm.

4.2 SIMULATION

An initial validation method to evaluate the multirotor UAV-based acoustic tomography is simulation. It allows for preliminary testing of the algorithm principles without the cost and time needed to build a prototype. Fig. 24 shows the structure of the simulation presented in this section. In the following sections, the algorithms and parameters that composes the simulation setup as illustrated in Fig. 24 are described in detail. The atmospheric model over which the AAT algorithms is being applied on this simulation setup is presented. The sound propagation model which, from the atmosphere model, provides the propagation time of the sound rays which compose one of the inputs of the AAT algorithm, is also presented. The parameters for the AAT algorithm and the reasons for their choice are presented in Sec. 4.2.3. The main references for the simulation algorithm employed in this dissertation are Kevin Rogers and Finn (2013) and Wiens and Behrens (2009a).

4.2.1 Atmosphere model and atmospheric RBF approximation

The base atmosphere model is simulated inside an 100 m diameter 600 m height regular cylinder with its base in the ground plane. A reference coordinate frame is placed centered in the bottom of the cylinder, with its z axis pointed upward. The atmosphere is divided in a grid mesh of around 100000 points, with each cell being 4 m in the x and y direction and 12 m in the z direction. A value of temperature and 3D wind velocity vector is assigned for every element of the grid based on the RBF network. Although the specific humidity value affects the speed of sound, as it can be seen in Eq. 4, the effects are much less significant than the variations in temperature and wind speed. Finn and Kevin Rogers (2016b) states that a 10 % error in the specific humidity estimation corresponds to a 0.02 % error in the path length. Because of that,

Figure 24 – Simulation setup

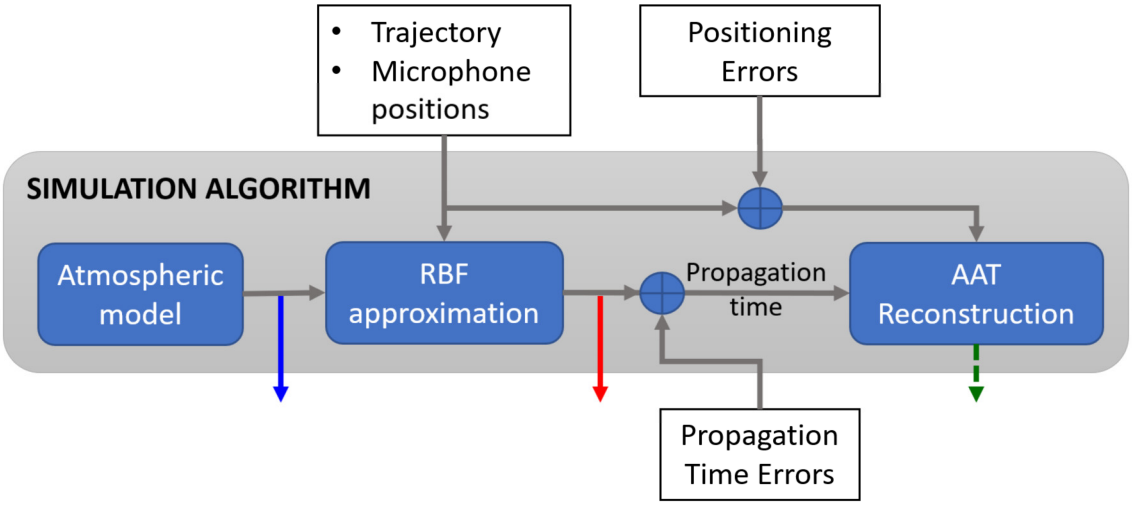

Source: Own elaboration. The blue rounded squares indicate the main algorithm blocks contained in the simulation. The white squares indicate the simulation parameters. The blue, red and green arrows correspond to the output data of the main algorithm blocks as presented in Figs. 28-31.

the variations in humidity in the atmosphere model are ignored. The errors caused by this abstraction are considered to be part of the noise of the system.

The simulated atmosphere model considers the atmosphere to be static in the time interval of the simulation, and does not account for any time-varying phenomena that are usually present in a real atmosphere. On a future stage of the research, when a prototype is fully functional, the acoustic tomography device will provide estimations of the average wind profile over the time interval where the data is collected. This simplification greatly reduces the complexity of the AAT algorithms while still allowing a preliminary analysis about the effectiveness of the technique in this configuration to be made.

4.2.1.1 Temperature profile

The temperature profile inside the simulated volume is based on the International Standard Atmosphere (International Standard Atmosphere (ISA)) model. The temperature profile of the ISA model inside the first 600 m decreases linearly from a base value of 288 K at 0 m height at a gradient of $-6.5 \times 10^{-3}\,\mathrm{K\,m^{-1}}$. Each point in the grid is assigned a temperature according to this model. A normally distributed random noise with standard deviation of 0.25 K is added on top of the temperature values in each point in the grid.

4.2.1.2 Wind speed profile

The wind speed profile is determined based on the log wind profile module, as explained in Sec. 3.1. In order to obtain the wind speed at a certain height based on a measurement taken at another, Eq. 1 can be rearranged as such:

$$u(z_2) = u(z_1)\frac{ln(z_2/z_0)}{ln(z_1/z_0)} \tag{30}$$

In order to make the execution of the AAT algorithms easily repeatable, and seeking to evaluate the performance of the AAT algorithm on different wind sites and conditions, the parameters that determine the characteristics of the wind profile on the simulated atmosphere are in part randomly assigned.

Eq. 30 is the equation used to determine the wind speed. z_0 is determined by a uniformly distributed random number in the interval between 0 and 0.1. This simulates a site with a maximum roughness length value equivalent to the one presented by an open-field terrain with up to 1 m tall grass (OKE, 2002). This value range corresponds to the expected roughness values encountered in wind assessment sites. $u(z_1)$ is the base wind speed at the height z_1. The base height is arbitrarily determined as 50 m. The base wind speed is determined by a uniformly distributed value between 3.5 and 9.5 $m s^{-1}$.

For the wind direction, all of the wind vectors on every point of the grid are rotated by the same amount, and point to the same randomly assigned direction. It is assumed that the prevailing wind direction does not have any vertical component.

From the wind speed and prevailing direction defined as such, the x and y components for the wind vectors in every point of the grid are determined. A normally distributed noise is then multiplied to the x and y components and added to the z component of each wind vector that composes the grid. This introduces small variations on the wind speed and direction.

4.2.1.3 Sound propagation

It is required from the simulation the ability to model the behavior of sound propagating in the atmosphere. Specifically, the propagation time of sound waves emitted from acoustic sources to sensors located inside or in the boundary of the modeled atmospheric module. As stated in Sec. 3.2, the atmosphere is a highly complex and dynamic system, and sound waves propagating through it are affected by many different phenomena. In order to achieve computationally less demanding simulation algorithms, a series of simplifications are made to the sound propagation model. Geometrical acoustic techniques are applied to analyze and obtain the propagation time. This abstraction is adequate to represent the AAT setup proposed in this dissertation, as long as the acoustic signal's wavelength is small enough compared to the surfaces it interacts with.

For the simulation, the curvature of the ray path, caused by diffraction effects, due to temperature, humidity and wind speed gradients in the atmosphere, is ignored. Consequently, all of the sound ray paths are approximated by straight lines in this simulation. This abstraction introduces an error in the ray path that affects both the direct travel-time analysis and the tomographic data reconstruction (ARNOLD et al., 2004). Compared to the straight line ray model considered here, the real curved ray path length is longer. This shortening in the path length causes an underestimation of the speed of sound during the tomographic reconstruction. This error increases with stronger sound speed gradients in the atmosphere.

4.2.1.4 RBF network

The propagation time of sound rays in the atmosphere in this simulation is determined by Eq. 14. In order to calculate the line integrals, a strategy similar to the one presented in Sec. 3.4.2 is employed. A network of Gaussian RBFs can be trained to provide a good approximation of the atmosphere profile data presented in Sec. 4.2.1.1 and 4.2.1.2. From the trained RBF networks, the complex computational task of calculating the line integrals of each ray path is reduced to a simple matrix multiplication, as in Eq. 17. However, the RBF based atmosphere model is merely an approximation, and errors are introduced in this step. These errors are dependent on the distribution and the spread coefficients of the RBF network. The RBF network used to simulate the atmosphere is the same one used by the AAT algorithm, with the same spread coefficients and distribution, but with different weights.

The position of the RBF centers is determined primarily by the performance of the AAT algorithm. Thus, to present the reasons behind the location of the RBF centers used by the atmosphere model to simulate the atmosphere profile, some aspects of the AAT inversion need to be assessed. In order to provide the AAT algorithm a well-conditioned least-squares inversion, each RBF function should be intercepted by a sufficient amount of observations, or in this case, ray paths. For an adequate distribution of RBFs, the work by Kevin Rogers and Finn (2013) is referred. That work states that if the spacing between the RBF centers is lower than 1.5 times the spacing of the sensor separation, a dramatic increase in the estimation errors is expected. It also states that for a fixed ratio between the spacing of the RBFs and the spacing between the sensors, the estimation errors are approximately inversely proportional to the RBF spacing. This phenomena occurs due to the fact that an increase in resolution, i.e. an increase in the number of RBFs, incurrs in an increase on the number of RBF coeficients to be estimated. This means that for a limited amount of observations, such increase in the resolution comes at the expense of a finer accuracy. For this simulation setup, the ground modules are displaced 100 m apart from a central module. The RBF spacing adopted is of 150 m. For this spacing, the RBF are disposed in a straight vertical line

centered over the central ground module. This chosen RBF disposition results in a loss of horizontal resolution in the atmosphere representation, and provides results similar to ones obtained by using LIDAR systems (see Sec. 2.3.9), which are currently applied in wind resource assessment for conventional wind power systems. A different RBF network configuration, with horizontal resolution, can be proposed, but the one presented in this dissertation presented the best results for the number of microphones and their disposition.

Fig. 25 shows a comparison of the wind and temperature values obtained by a RBF network approximation with respect to the atmospheric model and to an atmosphere estimated by an acoustic tomography of the atmosphere simulation. Figs. 28-31 show the height-averaged wind profile RBF approximation in comparison to the atmospheric model and the data reconstructed from the acoustic tomography of the atmosphere. It can be observed, specially from Fig. 28, that the RBF approximation cannot represent adequately the wind profile components that are closer to the surface, up to 60 m height. This is due to the small spread values determined for the Gaussian RBFs network. While those are adequate to represent the slower wind speed variations in higher altitudes, they are not adequate to represent the steeper inclination in the wind speed curve near the ground. Ultimately, this misrepresentation means that the RBF network applied cannot correctly represent the log wind profile which the atmosphere was modeled after. Different methods of determining the positions, spread coefficients and weights of the RBF network may be investigated in order to obtain RBF approximations with smaller errors, but such investigation is out of the scope of this dissertation.

Since the AAT algorithm receives the propagation time measurements of sound rays propagated in the RBF-approximated atmosphere model, the performance of the wind profile estimates is evaluated in comparison to this model, and not the original simulated profile presented in Sec. 4.2.1.1 and 4.2.1.2. This should be observed because most of the errors are caused by the RBF atmospheric approximation, and not the AAT algorithm. The accuracy of the atmospheric model is not being evaluated in this simulation, thus, the RBF approximation error is not considered in the algorithm analysis in this dissertation. On the other hand, neither our original atmosphere model nor a real atmosphere behave like a RBF trained network, and further study should be made in order to validate the algorithm on more accurate atmospheric models. However, such analysis is out of the scope of this dissertation.

One of the parameters to be determined for each network of RBFs is the spread coefficient. This parameter greatly affects the accuracy of the RBF representation of the atmosphere model. In order to decide the spread coefficient, a search algorithm is used to find the spread coefficient that minimizes the error between the RBF approximated atmosphere and the base atmosphere. This algorithm is run for each atmosphere

Figure 25 – Scatter plots of the original, approximated by RBFs and tomografically reconstructed atmospheres.

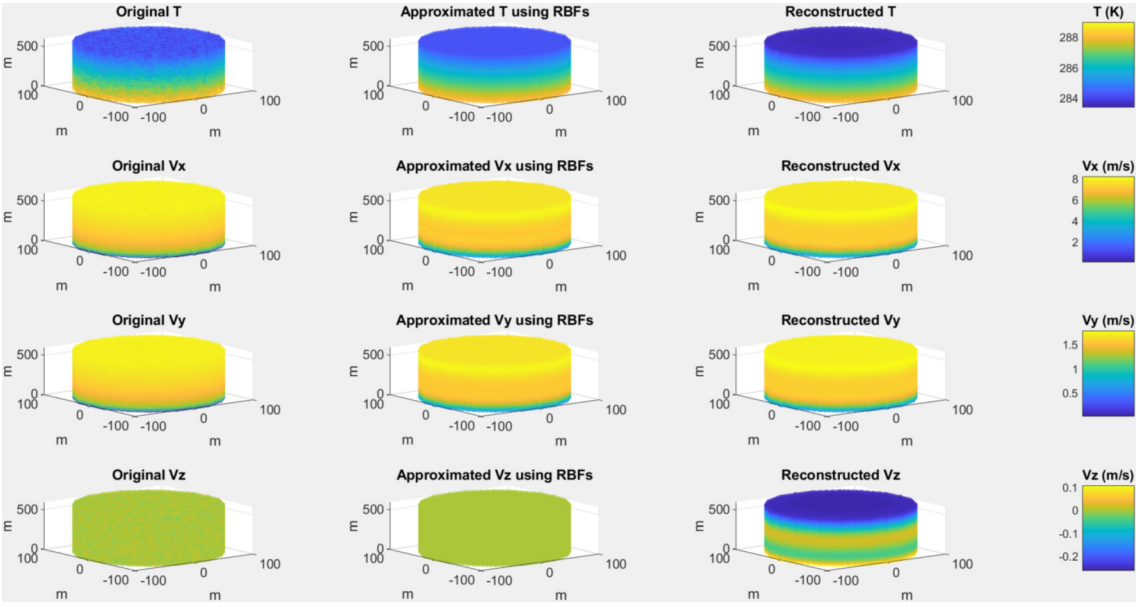

Source: Own elaboration. Data generated from propagation times with an added 0.01 % path length error and a 0.1 ms standard deviation normally distributed noise (see Sec. 4.2.4).

generated.

4.2.2 Measurement errors

In order to simulate the uncertainties in the measurements performed by the tomography system due to non-linearities and unmodeled phenomena, noise was added to the simulated propagation time, sensor and drone positions measurements, which are the input provided to the AAT algorithm. Finn and Kevin Rogers (2016b) presents a list of some of the sources of errors for a technique similar to the one presented in this thesis. Ray path approximation, effects of refraction of the sound ray, caustics, lack of wave coherence, statistical errors in the time delay estimation, wind noise in microphones, UAV and microphone position errors, variations in the sampling of Analog to Digital Converter (ADC) converters and uncertainty in the moisture content in the atmosphere are some of the errors cited by Finn and Kevin Rogers (2016b) that apply to this algorithm. All of those errors can be modeled as noise, added to the positioning of the UAV and ground sensor and to the propagation time. Finn and Kevin Rogers (2015) have done an extensive error analysis on the acoustic tomography algorithm and for a more detailed analysis on this matter, the reader is referred to their work. In their work they separated the error sources in four categories: Path length error; Timing error; UAV positioning error and Microphone location error. The way those errors are introduced to the simulation is described in this section.

The input error that contributes to most of the output error of the AAT algorithm is the error in the path length. The error in the path length is caused mainly by the straight line ray path approximation, as explained in 4.2.1.3. To simulate this effect, the time delay estimations are contaminated with a positive bias of 0.1 or 0.01 % of the true path length, in accordance with the simulations presented by Kevin Rogers and Finn (2013) and Finn and Kevin Rogers (2016b).

The other input errors listed by Finn and Kevin Rogers (2016b) that affect the time delay estimation in effect introduce non-linearities to the propagating media which alters the signal being processed by the cross correlation algorithm. These non-linearities attenuate the correlation peaks and introduce secondary peaks to the cross correlation function. The contribution of the errors in the moisture content in the atmosphere to the propagation time are briefly commented in Sec. 4.2.1. All of the errors other than path length errors are modeled as a normally distributed random component added to the propagation time with a standard deviation of 0.1 and 0.01 ms.

The RTK/PPK positioning system can be used to determine the position of both the UAV and the microphones in the ground modules. Thus, the positioning errors are modeled as a normally distributed random noise with a standard deviation of 5 cm added to the simulated position measurements, such as by Finn et al. (2017).

4.2.3 Acoustic atmosphere tomography setup

Three aspects are relevant for the tomography algorithm simulated in this dissertation: The RBF network, the UAV trajectory and the sensor placement. The RBF network adopted in the tomographic inversion is the same one defined for the atmosphere model already presented, thus, its characteristics are described in Sec. 4.2.1.4. In the following sections, the design choices made for the other aspects of the acoustic tomography setup are presented

4.2.3.1 Trajectory

In a previous work using UAV as a platform for 3D acoustic tomography (ROGERS, K.; FINN, 2013), an array of 49 sensors spaced 125 m apart is used to estimate the parameters of the atmosphere inside a 1 km edge cube. The acoustic tomography is performed with around 15000 observations and the results obtained are as accurate as the existing techniques used for measuring the wind and temperature profile. In an attempt to reduce costs, the number of microphones used in the array presented in this paper is reduced to only 5. Since the array presented in this paper comprises of only 5 sensors, a 2 Hz sampling rate is desired for the system to present a similar number of observations, considering a 25 min flight time of a multirotor UAV.

The flight trajectory proposed is similar to the one presented by Kevin Rogers and Finn (2013). The UAV starts its trajectory by ascending in a helix pattern. Once it

reaches the maximum height desired, the UAV then keeps its altitude and fly towards the center of the helix in a spiral motion. The flight trajectory of the UAV is represented in Fig. 26. This trajectory ensures that every RBF is intersected by a sufficient amount of observations that ensures a full rank matrix for the least-squares inversion in the tomographic algorithm. Fig. 27 shows a representation of the sound ray paths inside the atmosphere volume.

Figure 26 – Trajectory, sensor placement and RBF centers

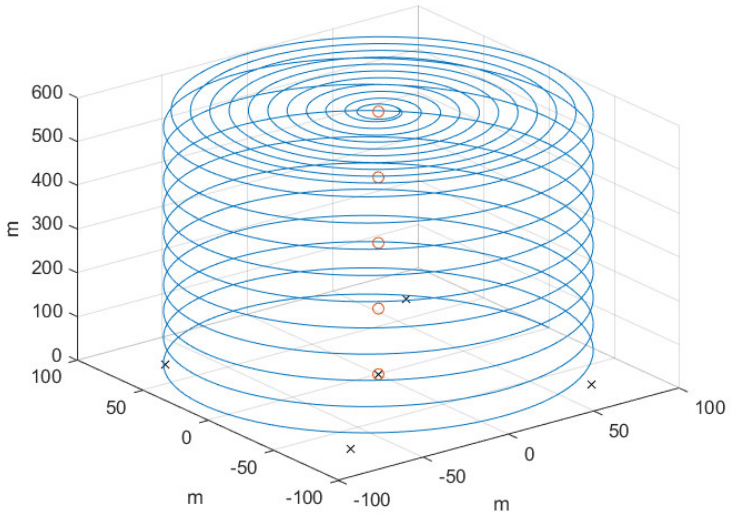

Source: Own elaboration. The UAV trajectory is represented in the blue line. The sensors are represented by black crosses and the RBF centers are rerpresented by red circles.

The disadvantage of using a 25 min trajectory for the tomographic observation is associated with the fact that the atmosphere is very dynamic and its parameters are likely to change in that time span. This means that the acoustic tomography presented in this dissertation is only capable of providing an estimate on the average of the wind speed and temperature along the desired volume in that time span. Thus, the information about the faster dynamics of the atmosphere is in effect filtered out. However, it is believed that this is not a significant hindrance in wind resource assessment applications, due to the fact that the commercially available wind profilers currently being used in this applications also provide time-averaged measurements.

4.2.3.2 Sensor placement

The simulation presented by Kevin Rogers and Finn (2013) considers a $\pm$ 1 m accuracy positioning device to determine the acoustic ray path. This is done for an array of microphones spaced apart by 125 m and distributed on the ground inside a 1000 m side square. A smaller spacing between microphones of around 100 m is proposed

Figure 27 – Graphic representation of the ray paths.

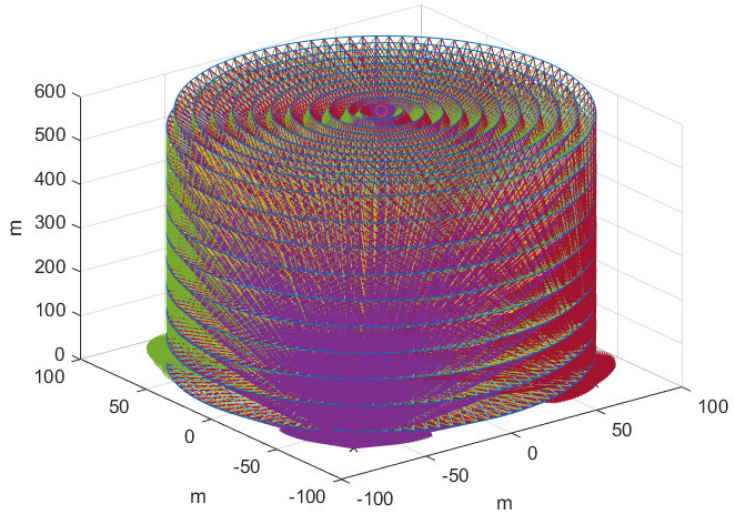

Source: Own elaboration. Straight lines with the same color represent the ray paths that are detected by the same microphone. The blue curved line is the UAV trajectory.

on this paper. The displacement of the sensors is defined as follows: One sensor is placed at the center of the array and the other 4 are positioned equally spaced in a 100 m radius circumference centered around the first sensor. The displacement of the sensors may be observed in Fig. 26. Simulation and experiments are used to evaluate the accuracy of the estimations provided by the AAT device with this sensor matrix configuration.

4.2.4 Simulation results

The AAT algorithm presented in this section is performed on a randomly generated atmosphere model, as specified in Sec. 4.2.1. The parameters from which the atmosphere was generated are described in Tab. 2, in terms of Eq. 1. The zero-plane displacement parameter is substracted to z_1 and z_2, and represents the height above the ground at which zero wind speed is achieved, due to obstacles such as vegetation. The randomly generated horizontal prevalent wind direction angle is 335.0352° off from the z axis in the reference frame. For the atmosphere generated based on these parameters, the spread of the RBF values obtained as explaned in 4.2.1.4 are 1.0712×10^{-7} for the temperature and 5.6414×10^{-7} for the wind speed networks.

The estimations of the AAT algorithm contaminated with a 0.1 % path length and 1 ms propagation time errors, as explained in Sec. 4.2.2, can be observed in Fig. 28. In this figure, the height-averaged wind profile data is plotted in comparison with the height-averaged atmosphere profile and the height-averaged RBF approximated atmosphere

Table 2 – Logarithmic wind profile parameters

Roughness length	z_0	0.0939 m
Base height	z_1	50 m
Mean wind speed at base height	u_{z_0}	6.6924 m s^{-1}
Zero-plane displacement		0.1 m

profile. In that figure, the wind speed values closely follow the RBF approximation, such as the wind direction and temperature. For a closer look at the errors, an error data plot is presented in Fig. 29. It can be seen from that figure that the wind speed and direction reconstruction height-averaged errors increase in the lower and higher extremes of the atmospheric volume. This effect has been observed on AAT data reconstructed from different simulated atmospheres, and usually the errors in the higher altitudes are larger than at the bottom. This could be explained by the fact that, due to the chosen trajectory and to the small amount of microphones at the ground, the RBFs located in the top of the volume are intersected by less ray paths and the ones in the bottom are not as uniformly distributed. The height-averaged reconstruction errors in the temperature profile present a significant bias in Fig. 29, but do not present any accentuated error either in the lower or higher altitudes. However, in a different manner, this trend was not observed on reconstructions performed in different simulated atmospheres. A detailed study about this apparent error behaviors is not in the scope of this project.

A similar trend can be observed on the data contaminated with less noise, as presented in Figs. 30 and 31. In this case, the simulated atmosphere and RBF network is the same, but the propagation time is contaminated with a 0.01 % path length and 0.1 ms standard deviation error. As expected, the accuracy of the algorithm is improved on low-noise conditions. Such as with the higher noise situation, an increase in the reconstruction error is observed near the upper limits of the atmosphere. The increase in the reconstruction error near the ground observed in Figs. 30 and 31 only happens in the wind direction estimations for the low noise situation. However, for the temperature estimations, a reconstruction error increase is observed on the higher altitudes.

If this trend of increased uncertainties in the lower and upper extremities of the AAT volume is verified in a future study, these data sections can be ignored in order to achieve an increased accuracy of the estimated wind profile in a shorter height range.

4.2.4.1 Comparative analysis

In order to evaluate the viability of the solution hereby presented, a comparison of the performance of the tomography device with other similar devices is of great interest. Two works have been chosen to participate in the comparison presented in this chapter. The first one is Palomaki et al. (2017). Palomaki et al. (2017) presents a performance comparison of two different methods to measure the wind speed and

Figure 28 – Height-averaged wind and temperature profile comparison for high noise situation

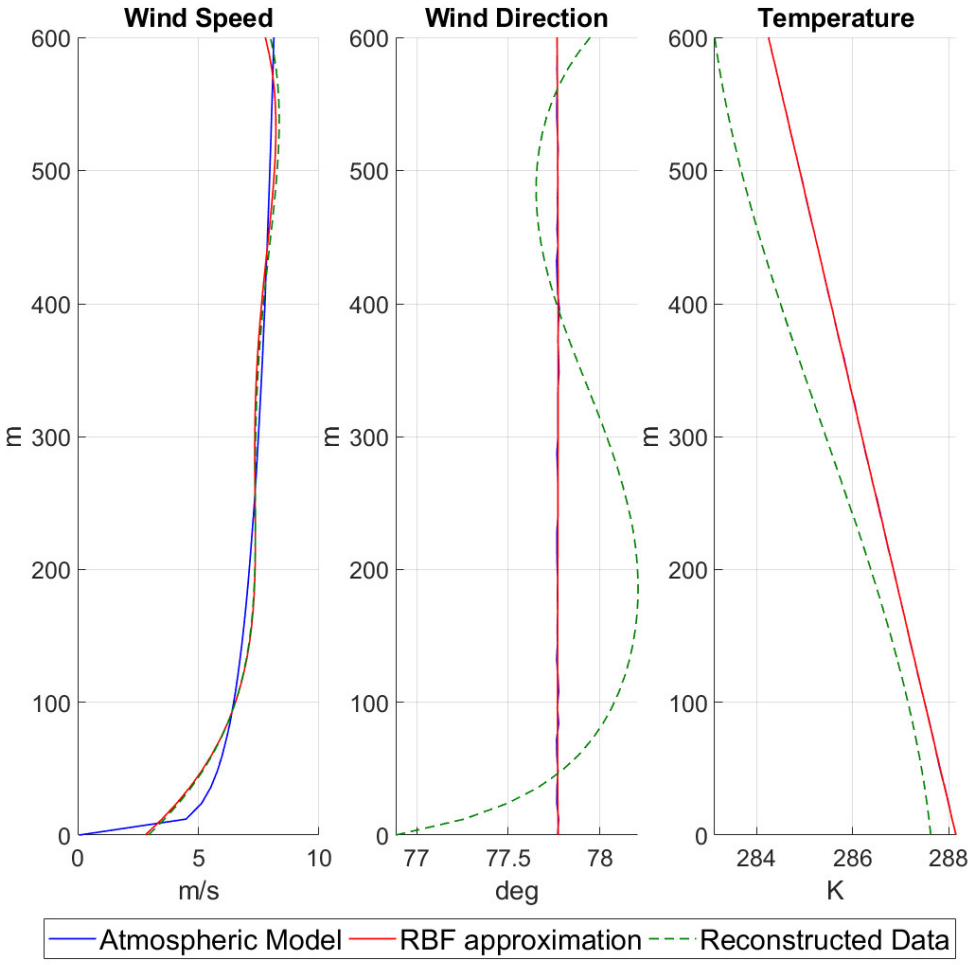

Source: Own elaboration. Data generated from propagation times with an added 0.1 % path length error and a 1 ms standard deviation normally distributed noise.

direction using multirotor UAVs. The first one is called the *direct approach* and the second one is called the *indirect approach*. The direct approach obtains the wind speed and direction measurements in a direct way, by using a sonic anemometer embedded in an hexacopter. The indirect approach uses the dynamic response of a hovering quadrotor to wind disturbances to estimate the wind and direction measurements. In order to hold a fixed position in space, an UAV has to counter-balance the drag forces actuating in it caused by the wind. The multirotor UAV does that by tilting the thrust vector slightly into the wind direction. This counter-balancing tilt-thrust combination is directly related to the wind speed and direction. The tilt can be measured by a simple

Figure 29 – Height-averaged wind and temperature profile errors for high noise situation

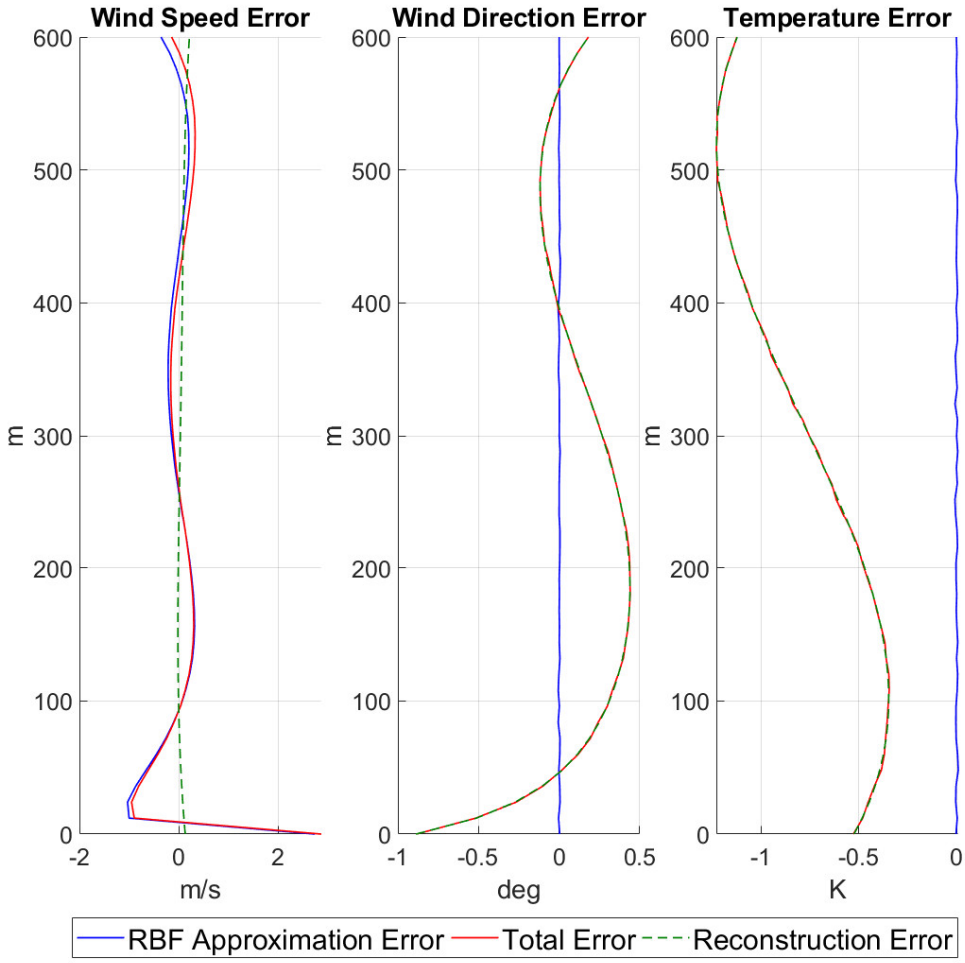

Source: Own elaboration. Data generated from propagation times with an added 0.1 % path length error and a 1 ms standard deviation normally distributed noise. For a more in-depth explanation of the different errors presented in this figure, see Sec. 4.2.1.4.

IMU, from which data is already available on most UAV flight controllers. The thrust is related to the current sent to the motors, which is also determined by the flight controller. In Palomaki et al. (2017), the performance of both methods is compared to independent measurements obtained simultaneously by an ultrassonic anemometer located in a nearby tower. An inferior performance of the measurements obtained by Palomaki et al. (2017) is expected in comparison to the estimations obtained in this dissertation due to the fact that they were not obtained in a perfectly controlled environment, such as in a simulation. The performance measurements provided by Palomaki et al. (2017) are the bias and the RMSE of the wind speed and direction obtained from four flight

Figure 30 – Height-averaged wind and temperature profile comparison for low noise situation

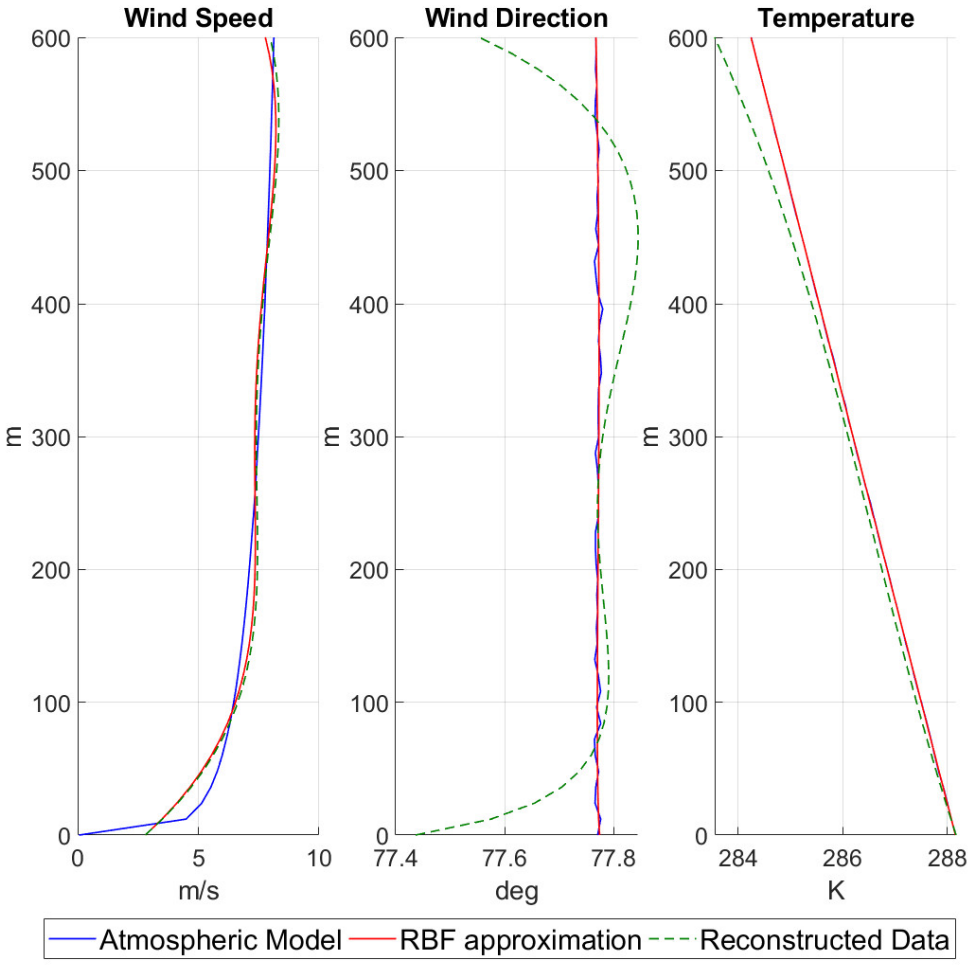

Source: Own elaboration. Data generated from propagation times with an added 0.01 % path length error and a 0.1 ms standard deviation normally distributed noise.

experiments performed on each measuring device.

The second work from which this dissertation's results are compared is Finn et al. (2017). Finn et al. (2017) presents an AAT device that uses a fixed-wing UAV to estimate the wind profile. The method employed in that work to obtain the estimations is similar to the one proposed in this dissertation. The methods mainly differ in regards to the propagation time determination. In Finn et al. (2017), the propagation time is determined based on the frequency-shift of the sound signature of the UAV's engine. In Finn et al. (2017), the estimated wind profile is compared to SODAR measurements obtained simultaneously on a section of the atmosphere contained inside the AAT

Figure 31 – Height-averaged wind and temperature profile errors for low noise situation

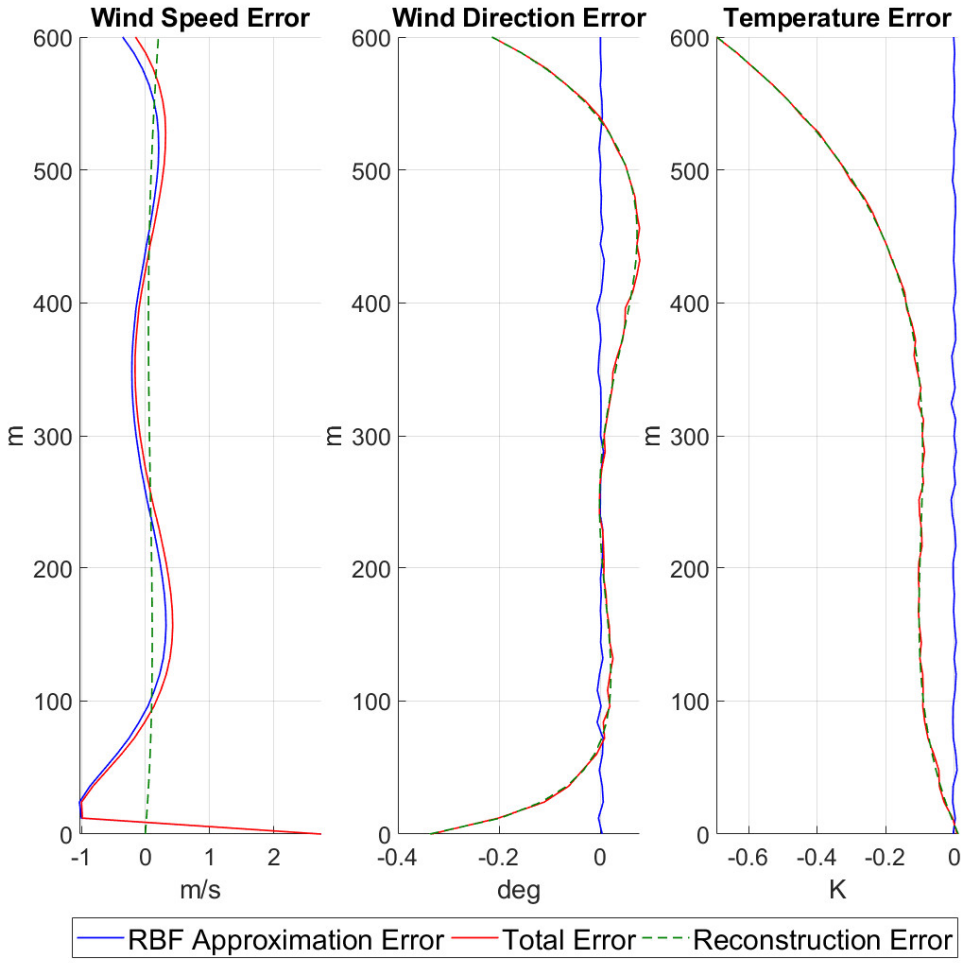

Source: Own elaboration. Data generated from propagation times with an added 0.01 % path length error and a 0.1 ms standard deviation normally distributed noise. For a more in-depth explanation of the different errors presented in this figure, see Sec. 4.2.1.4.

volume. The performance measurements on that work provided for the AAT device are the bias and the standard deviation for every component of the wind vector and temperature.

Another performance threshold that is interesting for the evaluation of weather observation instruments is the World Meteorological Organization's (WMO) accuracy requirements for wind and temperature instruments (WMO, 2014). Those are presented in Tab. 3.

The RMSE values for the AAT algorithm in comparison to the RBF approximated for a single experiment is presented in Tab. 4. Figs. 32 and 33 show a comparison

Table 3 – WMO's uncertainty requirements for weather observation instruments (WMO, 2014).

Quantity	Uncertainty Requirement (2σ)	Observation
Air temperature	0.1 K	between –40 °C and 40 °C
Wind velocity	0.5 m s^{-1}	10 % for >5 m s^{-1}
Wind direction	5°	

with the data found in Palomaki et al. (2017) and the WMO requirement threshold. The lines WMO-V and WMO° are determined as half the corresponding 2σ requirements. Although the bias and standard deviation are the adequate quantities to be compared with the uncertainty requirements, this data was not made available in Palomaki et al. (2017). The threshold is only present on the plot to be an independent reference from which both devices can be evaluated. The information in the data tables, at the end of this section, is presented for four different scenarios:

(a) Propagation time contaminated with 0.1 % path length error and 1 ms standard deviation normally distributed noise;

(b) Propagation time contaminated with 0.01 % path length error and 0.1 ms standard deviation normally distributed noise;

(c) Propagation time contaminated with 0.1 % path length error and 1 ms standard deviation normally distributed noise, disconsidering the lowest and the highest 10 % of the estimated data;

(d) Propagation time contaminated with 0.01 % path length error and 0.1 ms standard deviation normally distributed noise, disconsidering the lowest and the highest 10 % of the estimated data.

Table 4 – RMSE values

	a	b	c	d
V_x	0.0790	0.0877	0.0541	0.0779
V_y	0.0372	0.0217	0.0379	0.0142
V_z	0.2336	0.0992	0.2247	0.0625
T	0.8458	0.2429	0.8300	0.1622
$\lvert V \rvert$	0.2494	0.1342	0.2342	0.1009
$\angle V$	0.2869	0.0783	0.2790	0.0374

Fig. 32 shows a very large difference between the RMSE values of the wind direction estimations presented in this dissertation and the ones obtained by Palomaki et al. (2017). The RMSE values for wind directions provided for Palomaki et al. (2017) are significantly above the WMO requirements, while the ones obtained by the device

Figure 32 – RMSE of the multirotor UAV-assisted AAT horizontal wind direction estimations in comparison with other similar devices

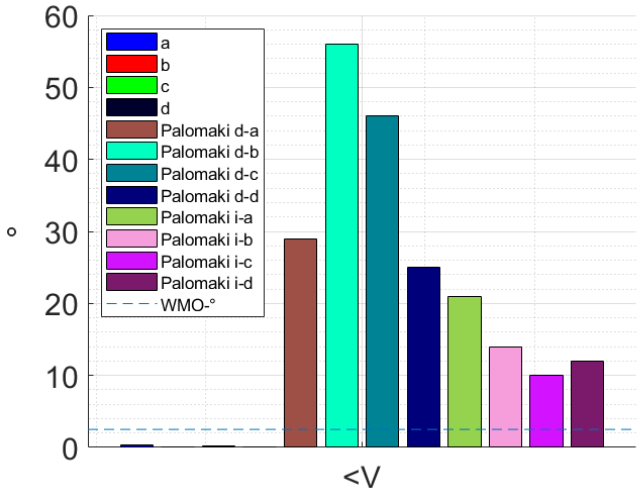

Source: Own elaboration. RMSE values for the AAT algorithm in comparison with the RBF approximated profile for the following scenarios: a) Propagation time contaminated with 0.1 % path length error and 1 ms standard deviation normally distributed noise; b) Propagation time contaminated with 0.01 % path length error and 0.1 ms standard deviation normally distributed noise; c) Propagation time contaminated with 0.1 % path length error and 1 ms standard deviation normally distributed noise, disconsidering the lowest and the highest 10 % of the estimated data; d) Propagation time contaminated with 0.01 % path length error and 0.1 ms standard deviation normally distributed noise, disconsidering the lowest and the highest 10 % of the estimated data. Datasets *Palomaki d(a-b)* are resulting from 4 flights performed on a comparative analysis experiment between a multirotor UAV-mounted sonic anemometer and independent measurements (PALOMAKI et al., 2017). Datasets *Palomaki i(a-b)* are resulting from 4 flights performed on a comparative analysis experiment between an indirect wind-measuring method using a theoretically derived tilt-wind relationship and independent measurements (PALOMAKI et al., 2017). *WMO-°* is the WMO performance requirement established for horizontal wind direction sensors used in weather observation (WMO, 2014).

proposed in this dissertation are below, in every scenario. The wind angle measurements comparison with the results presented by Palomaki et al. (2017) shows the largest parameter accuracy difference between devices. According to Palomaki et al. (2017), the poor RMSE performance for the direction measurements can occur due to a series of reasons. For the direct approach, the variable tilt in the UAV caused by wind gusts and flight control and the turbulence caused by the rotors are the reasons appointed. For the indirect approach, variability in the GNSS coverage is the reason pointed for such inaccuracies. As seen in Fig. 34, the high RMSE values presented by Palomaki et al. (2017) can be explained mostly by the large bias values. It is unfortunate that the standard deviation of the measurements has not been published by the authors. Consequently, a better comparison between devices and understanding of the error characteristics is not possible.

Fig. 33 shows that the RMSE values of the wind speed estimations obtained in this dissertation are smaller than the ones obtained by Palomaki et al. (2017), lying

Figure 33 – RMSE of the multirotor UAV-assisted AAT wind speed estimations in comparison with other similar devices

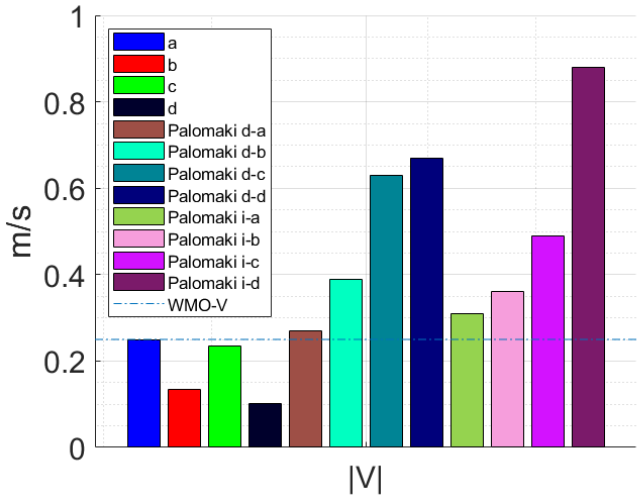

Source: Own elaboration. RMSE values for the AAT algorithm in comparison with the RBF approximated profile for the following scenarios: a) Propagation time contaminated with 0.1 % path length error and 1 ms standard deviation normally distributed noise; b) Propagation time contaminated with 0.01 % path length error and 0.1 ms standard deviation normally distributed noise; c) Propagation time contaminated with 0.1 % path length error and 1 ms standard deviation normally distributed noise, disconsidering the lowest and the highest 10 % of the estimated data; d) Propagation time contaminated with 0.01 % path length error and 0.1 ms standard deviation normally distributed noise, disconsidering the lowest and the highest 10 % of the estimated data. Datasets *Palomaki d(a-b)* are resulting from 4 flights performed on a comparative analysis experiment between a multirotor UAV-mounted sonic anemometer and independent measurements (PALOMAKI et al., 2017). Datasets *Palomaki i(a-b)* are resulting from 4 flights performed on a comparative analysis experiment between an indirect wind-measuring method using a theoretically derived tilt-wind relationship and independent measurements (PALOMAKI et al., 2017). *WMO-V* is the WMO performance requirement established for wind speed sensors used in weather observation (WMO, 2014).

below the WMO uncertainty requirements.

Tab. 5 presents the bias values for the estimations obtained by the multirotor AAT device. It can be seen that for the cartesian components of the wind velocity, their absolute values are mostly small, below or around $0.1\,\mathrm{m\,s^{-1}}$. The temperature biases are negative and have a larger magnitude for the high-noise scenarios a and c. The larger negative bias for the temperature estimations can be explained by the effect of the path length error in the tomographic inversion. Since the considered path length is always smaller than the actual path length of the sound rays, a negative bias for the speed of sound appears in every AAT observation. Since the path length error is not modeled in the reconstruction phase of the AAT algorithm, a negative temperature bias may appear in the estimated wind profile to account for the negative speed of sound bias effect on the atmospheric volume. Another parameter bias that may be specially affected by the unmodeled path length error is the V_Z component of the wind vector. Since every ray path propagates downward, a negative V_Z bias would also be able to compensate

the negative speed of sound bias for every point in the grid. If this hypothesis is verified to be true, it could explain the large negative temperature bias observed. A detailed investigation on this matter is not in the scope of this dissertation, but, if confirmed upon further studies, could be compensated by a calibration function, by an improved ray path definition algorithm and/or by introducing sound rays propagating upwards to the observations.

Table 5 – Bias Values

	a	b	c	d
V_x	0.0581	0.0798	0.0397	0.0752
V_y	-0.0040	0.0170	-0.0149	0.0125
V_z	-0.1071	-0.0532	-0.1168	-0.0383
T	-0.7766	-0.1792	-0.7660	-0.1417
$\lvert V \rvert$	0.2311	0.1136	0.2161	0.0936
$\angle V$	0.1141	-0.0053	0.1870	0.0278

It can be observed from Figs. 34 and 35 that, apart from the temperature, the bias values of the multirotor AAT simulation are at least in the same range of the bias of the other devices. Finn a's bias are significantly larger in comparison to the other devices, specially in the V_x, V_y and T estimations. The bias of the wind direction measurements obtained by Palomaki et al. (2017) are significantly larger than the ones presented in this dissertation.

Tab. 6 presents the standard deviations of the estimations obtained by the multirotor AAT simulation described in this dissertation. Fig. 36 presents a comparison of these standard deviations with the ones obtained by Finn et al. (2017). The standard deviations of the wind estimations are below the WMO requirements for every scenario, which indicates that if the systematic errors can be corrected or compensated, the estimations are accurate enough to be used for weather observation in low-noise situations. For the temperature measurements, the standard deviations obtained in the simulation do not meet the WMO requirements, in every scenario. However, in scenario d, the difference is small, and may be diminished or even eliminated with further improvements in the AAT algorithm. In Finn et al. (2017), both wind component and temperature estimations do not meet the WMO requirements.

Table 6 – Standard deviation values

	a	b	c	d
V_x	0.0536	0.0366	0.0367	0.0205
V_y	0.0370	0.0135	0.0348	0.0068
V_z	0.2076	0.0838	0.1920	0.0494
T	0.3351	0.1639	0.3194	0.0790
$\lvert V \rvert$	0.0938	0.0716	0.0902	0.0377
$\angle V$	0.2632	0.0781	0.2071	0.0250

Figure 34 – Bias of the multirotor UAV-assisted AAT estimations in comparison with other similar devices

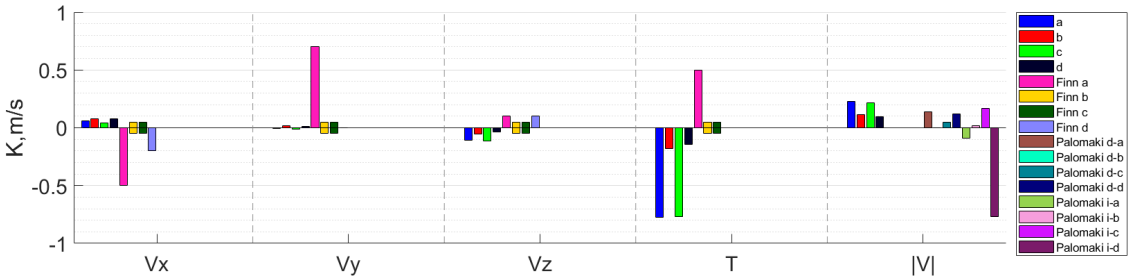

Source: Own elaboration. Bias values for the AAT algorithm in comparison with the RBF approximated profile for the following scenarios: a) Propagation time contaminated with 0.1 % path length error and 1 ms standard deviation normally distributed noise; b) Propagation time contaminated with 0.01 % path length error and 0.1 ms standard deviation normally distributed noise; c) Propagation time contaminated with 0.1 % path length error and 1 ms standard deviation normally distributed noise, disconsidering the lowest and the highest 10 % of the estimated data; d) Propagation time contaminated with 0.01 % path length error and 0.1 ms standard deviation normally distributed noise, disconsidering the lowest and the highest 10 % of the estimated data. Datasets *Palomaki d(a-b)* are resulting from 4 flights performed on a comparative analysis experiment between a multirotor UAV-mounted sonic anemometer and independent measurements (PALOMAKI et al., 2017). Datasets *Palomaki i(a-b)* are resulting from 4 flights performed on a comparative analysis experiment between an indirect wind-measuring method using a theoretically derived tilt-wind relationship and independent measurements (PALOMAKI et al., 2017). Datasets *Finn a-b* are data from a comparison between an fixed-wing UAV-assisted tomography device and a sodar profile (FINN et al., 2017) and stand for: Finn a) Raw estimated data; Finn b) Estimated data corrected for wind-related bias; Finn c) Estimated data corrected for bias and good observations only; Finn d) Vector sum data, obtained from the mean difference between the sodar wind component data and the vector sum of any AAT overflight profiles that fall within the requisite 10 min time window of the sodar observation.

4.2.4.1.1 Comparative analysis summary

The comparative analysis performed in this section shows that, for the fictitious atmosphere generated, the multirotor-UAV-based AAT tomograph presents wind speed and direction estimations with better performance than the other devices it is being compared to. The wind speed and direction estimations are sufficiently accurate for weather observation, as required by the WMO, in every scenario simulated. The temperature estimations of the multirotor-UAV-based AAT tomograph are strongly biased, and because of that, its performance is poorer when compared to the temperature estimations obtained by (FINN et al., 2017). However, this bias seems to be caused by a systematic error that could be compensated by a simple calibration procedure. This calibration procedure has the potential to improve significantly not only the temperature estimations, but all of the other measurements. In order to perform such calibration, an extensive statistical study on the tomography algorithm is required to correctly identify the behavior of the bias, which can be used to correct the obtained measurements. An extensive statistical study of the algorithm is out of the scope of this thesis.

Figure 35 – Wind direction bias of the multirotor UAV-assisted AAT estimations in comparison with other similar devices

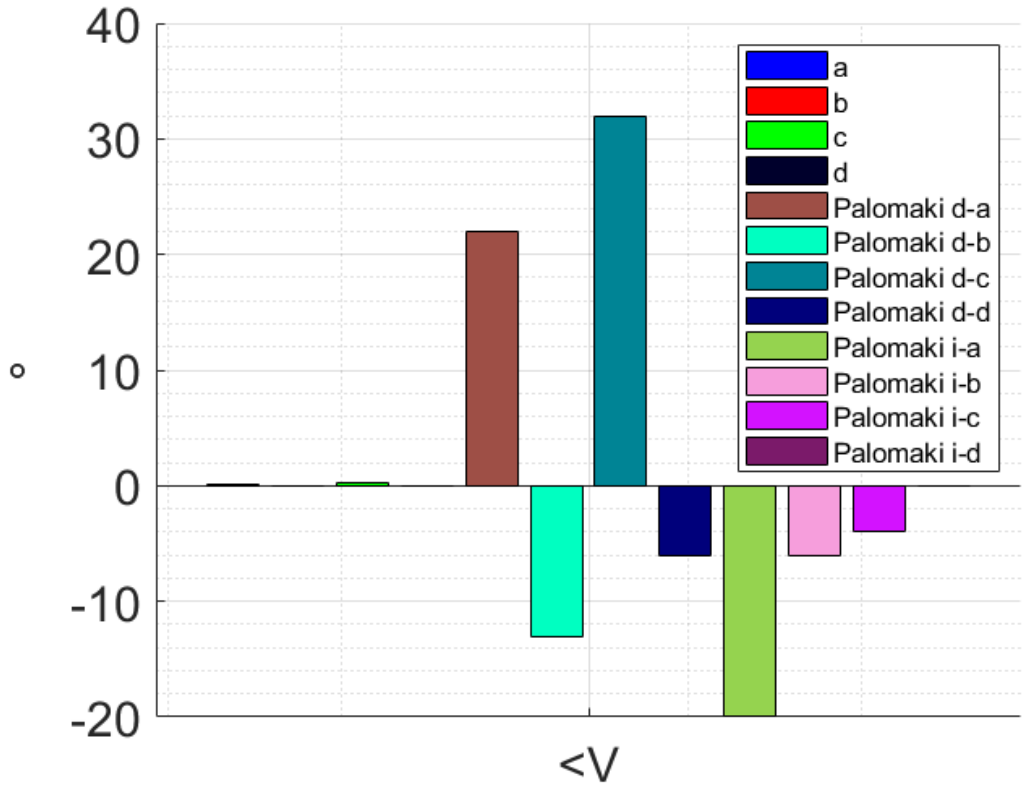

Source: Own elaboration. Bias values for the AAT algorithm in comparison with the RBF approximated profile for the following scenarios: a) Propagation time contaminated with 0.1 % path length error and 1 ms standard deviation normally distributed noise; b) Propagation time contaminated with 0.01 % path length error and 0.1 ms standard deviation normally distributed noise; c) Propagation time contaminated with 0.1 % path length error and 1 ms standard deviation normally distributed noise, disconsidering the lowest and the highest 10 % of the estimated data; d) Propagation time contaminated with 0.01 % path length error and 0.1 ms standard deviation normally distributed noise, disconsidering the lowest and the highest 10 % of the estimated data. Datasets *Palomaki d(a-b)* are resulting from 4 flights performed on a comparative analysis experiment between a multirotor UAV-mounted sonic anemometer and independent measurements (PALOMAKI et al., 2017). Datasets *Palomaki i(a-b)* are resulting from 4 flights performed on a comparative analysis experiment between an indirect wind-measuring method using a theoretically derived tilt-wind relationship and independent measurements (PALOMAKI et al., 2017).

Figure 36 – Standard deviation of the AAT estimations in comparison with other similar devices

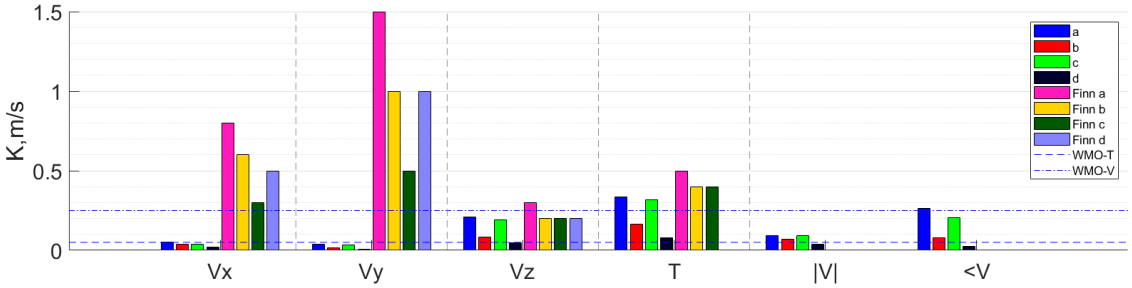

Standard deviation values for the AAT algorithm in comparison with the RBF approximated profile for the following scenarios: a) Propagation time contaminated with 0.1 % path length error and 1 ms standard deviation normally distributed noise; b) Propagation time contaminated with 0.01 % path length error and 0.1 ms standard deviation normally distributed noise; c) Propagation time contaminated with 0.1 % path length error and 1 ms standard deviation normally distributed noise, disconsidering the lowest and the highest 10 % of the estimated data; d) Propagation time contaminated with 0.01 % path length error and 0.1 ms standard deviation normally distributed noise, disconsidering the lowest and the highest 10 % of the estimated data. Datasets *Finn a-b* are data from a comparison between an fixed-wing UAV-assisted tomography device and a sodar profile (FINN et al., 2017) and stand for: Finn a) Raw estimated data; Finn b) Estimated data corrected for wind-related bias; Finn c) Estimated data corrected for bias and good observations only; Finn d) Vector sum data, obtained from the mean difference between the sodar wind component data and the vector sum of any AAT overflight profiles that fall within the requisite 10-min time window of the sodar observation. *WMO-T* and *WMO-V* are, respectively, the WMO performance requirements established for temperature and winds velocity sensors used for weather observations (WMO, 2014). WMO requirements for wind direction measurements are out of the scale (2.5°).

5 CONCLUSION

In this thesis, a software and hardware project for a multirotor UAV-based AAT prototype specifically designed to be used in wind resource assessment for AWE applications is presented. The hardware setup is based upon a series of distributed instruments embedded in the payload of the UAV and in five ground modules. The AAT algorithms were simulated in a computation platform, configured in accordance with the designed prototype, and the performance of the preliminary results of the wind profile estimations were presented and compared with other similar UAV-based wind measuring devices.

The software results presented in this dissertation show that the WMO accuracy requirements are potentially achievable in at least certain scenarios, but some improvements may be necessary to make the system consistently perform under the WMO requirements. It has also been shown that the accuracy performance of the technique in the simulations presented in this dissertation is comparable to the results from experiments performed in similar devices. Though the statistical analysis on the algorithm was out of the scope of this dissertation, some of the algorithm trends that were noted in this dissertation appeared in other repetitions of the experiment that were not reported in the experimental results. Still, this dissertation has shown that the AAT measurement principle works in the proposed setup with a similar performance to other AAT setups.

As for the hardware, it has been shown in this dissertation that in theory the hardware setup proposed seems to be adequate to perform all of the functionalities required by the AAT. In a specific manner, this dissertation presented the multirotor UAV platform as an advantageous alternative for AAT instruments used in wind speed and temperature profile for wind resource assessment. The innovative application of the AAT technology in such platform allows the tomography device to be able to take-off and land vertically in an automated procedure, dispensing the need of long runways or manual operation. This is a fundamental aspect for the continuous and autonomous operation of a measuring equipment being employed in wind resource assessment. Also, the modular hardware design proposed allows for flexibility and portability, both in the preliminary tests and final experiments.

This dissertation investigates for the first time in depth the use of a VTOL UAV as a platform for acoustic atmospheric tomography, and also brings up contributions in different fields. It describes a wind profiler that can be used in wind resource assessment for AWE in different height ranges than the conventional profilers at a fraction of the cost and that could be easily deployed in remote sites. The low-cost, portable wind profiler could facilitate the wind assessment process, opening up the possibilities of installment of AWE technologies where otherwise, the assessment process would make the entrepreneurship unviable due to cost or accessibility issues. The knowledge of the

wind profile also could aid the research of automatic take-off and landing procedures for AWE systems. The multirotor UAV wind profiler could be also employed as a low cost substitute for conventional wind profilers in weather observation systems. To the UFSCKite, the algorithms developed in this work provide a set of tools that will allow further study, comparison, development, validation, statistical analysis and technique enhancement of AAT algorithms.

5.1 FUTURE WORKS

This dissertation presented the first steps of a new area of study on the UFSCKite research group that shows a lot of potential. It is the first study performed in the research group, aimed at the development of a low cost autonomous wind measurement prototype unit capable to operate continuously on a remote site. Many issues have not been fully addressed and studies with more details are expected to follow the dissertation hereby presented. Nevertheless, this work represents a solid advance in that direction. The hardware design presented provides a firm foundation for the final assembly of the prototype, since many instrumentation issues have already been overcome. The algorithms presented and validated compose the majority of the software to be employed in the prototype and also from which further software exploration can be performed.

In what regards the software, limited conclusions can be drawn for the analysis presented in this dissertation, because the results were validated through numerical simulations only. Experimental results were not possible due to several hardware problems that will be addressed in future works. Also, the RBF approximation of a wind profile introduces a significant error to the AAT reconstruction, which is not being considered in the algorithm analysis presented in this dissertation. The straight line ray path approximation is a significant source for error in the AAT algorithm. The performance of the algorithm is expected to degrade on wind conditions with more accentuated wind speed gradients, and that analysis was not performed in this study.

As for the hardware, the lack of preliminary tests of the subsystems may have concealed some issues of the hardware setup that were not made known beforehand. The continuous operation of UAV systems is more likely to have more data gaps than conventional profilers or other weather measurement systems due to unfavorable weather conditions. The lack of a statistical analysis of the AAT algorithm makes the results achieved unable to be used to validate or refine the hardware requirements that were initially proposed.

In order to overcome these and other identified shortcomings, the direction suggested for the future work related to this dissertation is presented:

1. Realization of statistical analysis of the proposed AAT estimations.

2. Realization of preliminary hardware studies.
    a) Study the adequacy of the sound signature for the AAT application.
    b) Study the adequacy of the synchronization system for the AAT application.
3. Improvement of the AAT algorithm.
    a) Implementation a sensor fusion technique to improve the UAV positioning.
    b) Addition of direct observations to aid the AAT algorithm, as described by Finn and Kevin Rogers (2015).
    c) Implementation of an improved model of the sound propagation in the atmosphere.
    d) Implementation of an improved atmosphere model or real atmospheric data.
    e) Study of the effect of different wind and temperature profiles on the AAT reconstruction.
    f) Study of the effect of a curved ray path propagation model for the reconstruction.
    g) Study of the effect of different trajectories on the AAT outcome.
    h) Study of the effect of additional ground modules and different disposition on the AAT outcome.
    i) Addition of upward or reciprocal propagating sound rays to AAT setup.
    j) Study of the effects of employing different methods to define the RBF network distribution, spread coefficients and weights.
    k) Employment of different inversion methods in the AAT reconstruction.

REFERÊNCIAS

ARCHER, Cristina L; CALDEIRA, Ken. Global assessment of high-altitude wind power. **Energies**, Molecular Diversity Preservation International, v. 2, n. 2, p. 307–319, 2009. DOI: 10.3390/en20200307.

ARNOLD, K; ZIEMANN, A; RAABE, A; SPINDLER, G. Acoustic tomography and conventional meteorological measurements over heterogeneous surfaces. **Meteorology and Atmospheric Physics**, Springer, v. 85, n. 1-3, p. 175–186, 2004.

ASH, Joshua N.; MOSES, Randolph L. Acoustic time delay estimation and sensor network self-localization: Experimental results. **The Journal of the Acoustical Society of America**, v. 118, n. 2, p. 841–850, Aug. 2005. ISSN 0001-4966. DOI: 10.1121/1.1953307. Available from: https://asa.scitation.org/doi/10.1121/1.1953307. Visited on: 5 Feb. 2020.

ASSIREU, Arcilan T.; MENDONÇA, José C.; FREITAS, Ramon M.; REIS, André L.; PELLEGRINI, Cláudio C.; PIMENTA, Felipe M. Uso de VANT para Prospecção Eólica em Sistemas Aquáticos: Desenho Amostral e Avanços Instrumentais. pt. **Revista Brasileira de Meteorologia**, scielo, v. 34, p. 237–245, June 2019. ISSN 0102-7786. DOI: 10.1590/0102-77863340037. Available from: http://www.scielo.br/scielo.php?script=sci_arttext&pid=S0102-77862019000200237&nrm=iso.

BALLOU, Glen. **Handbook for Sound Engineers**. Ed. by Focal press. 4th ed. [S.l.: s.n.], 2008. ISBN 978-0-240-80969-4.

BANTA, Robert M.; SHUN, C.M.; LAW, Daniel C.; BROWN, William; REINKING, Roger F.; HARDESTY, R. Michael; M.J. POST, Christoph J. Senffand W. Alan Brewer and; DARBY, Lisa S. Observational Techniques: Sampling the Mountain Atmosphere. In: **Mountain Weather Research and Forecasting**: Recent Progress and Current Challenges. Ed. by Fotini K. Chow. Ed. by Stephan F.J. De Wekker. Ed. by Bradley J. Snyder. 1. ed. [S.l.]: Springer Netherlands, 26 Apr. 2012. chap. 8. (Springer Atmospheric Sciences). ISBN 978-94-007-4098-3. DOI: 10.1007/978-94-007-4098-3.

BARTH, Stephan; KOCH, Holger; KITTEL, Achim; PEINKE, Joachim; BURGOLD, Jörg; WURMUS, Helmut. Laser-cantilever anemometer: A new

high-resolution sensor for air and liquid flows. **Review of Scientific Instruments**, v. 76, Apr. 2005. DOI: 10.1063/1.1979467.

BL SERIES. **BL Series - Lithium Iron Phosphate batteries**. [S.l.: s.n.]. publisher: BSOL Batteriesystemme GmbH. Available from: http://www.bsol-shop.de/files/en/Lithium/BL%20Brochure%20ALL.pdf. Visited on: 5 Feb. 2020.

BROWN, Edmund H.; HALL, Freeman F. Advances in atmospheric acoustics. en. **Reviews of Geophysics**, v. 16, n. 1, p. 47, 1978. ISSN 8755-1209. DOI: 10.1029/RG016i001p00047. Available from: http://doi.wiley.com/10.1029/RG016i001p00047. Visited on: 31 Jan. 2020.

BUCHER, Ralph; MISRA, D. **A Synthesizable VHDL Model of the Exact Solution for Three-dimensional Hyperbolic Positioning System**. en. [S.l.: s.n.], 2001. DOI: https://doi.org/10.1080/1065514021000012129. Available from: https://www.hindawi.com/journals/vlsi/2002/935925/. Visited on: 2 Feb. 2020.

BUSCH, N.; KRISTENSEN, L. Cup Anemometer Overspeeding. **Journal of Applied Meteorology**, v. 15, p. 1328–1332, Nov. 1976. DOI: 10.1175/1520-0450(1976)015<1328:CAO>2.0.CO;2.

BUSCH, N. E.; CHRISTENSEN, O.; KRISTENSEN, L.; LADING, L.; LARSEN, S. E. Cups, Vanes, Propellers, and Laser Anemometers. In: **Air-Sea Interaction: Instruments and Methods**. Ed. by F. Dobson, L. Hasse and R. Davis. Boston, MA: Springer US, 1980. P. 11–46. ISBN 978-1-4615-9182-5. DOI: 10.1007/978-1-4615-9182-5_2. Available from: https://doi.org/10.1007/978-1-4615-9182-5_2.

CHILSON, Phillip B.; HUCK, R.; FIEBRICH, C.; CORNISH, D.; WAWRZYNIAK, T.; MAZUERA, S.; DIXON, A.; BURNS, E.; GREENE, B. **Calibration and Validation of Weather Sensors for Rotary-Wing UAS: The Devil is in the Details**. [S.l.: s.n.], 2012.

CLANCY, L. J. **Aerodynamics**. New York: Wiley, 1975. ISBN 9780470158371.

CORNUELLE, Bruce D; WORCESTER, Peter F; DZIECIUCH, Matthew A. Ocean acoustic tomography. In: IOP PUBLISHING, 1. JOURNAL of Physics: Conference Series. [S.l.: s.n.], 2008. P. 012002.

DENG, Da. Li-ion batteries: basics, progress, and challenges. **Energy Science & Engineering**, v. 3, n. 5, p. 385–418, 2015. DOI: 10.1002/ese3.95. eprint: https://onlinelibrary.wiley.com/doi/pdf/10.1002/ese3.95. Available from: https://onlinelibrary.wiley.com/doi/abs/10.1002/ese3.95.

DENG, Da; GYU KIM, Min; YANG LEE, Jim; CHO, Jaephil. Green energy storage materials: Nanostructured TiO 2 and Sn-based anodes for lithium-ion batteries. en. **Energy & Environmental Science**, v. 2, n. 8, p. 818–837, 2009. DOI: 10.1039/B823474D. Available from: https://pubs.rsc.org/en/content/articlelanding/2009/ee/b823474d. Visited on: 6 Feb. 2020.

DOBSON, Frank; HASSE, Lutz; DAVIS, Russ. **Air-sea interaction: instruments and methods**. [S.l.]: Springer Science & Business Media, 2012. ISBN 9781461591825. DOI: 10.1007/978-1-4615-9182-5.

DVORAK, Paul. **Triton Verification Studies – Ecofys, 2016 – SoDAR & met mast recordings consist & highly correlated**. en-US. [S.l.: s.n.]. Available from: https://www.windpowerengineering.com/triton-verification-studies-ecofys-2016/. Visited on: 29 Jan. 2020.

EARGLE, John; FOREMAN, Chris. **Greater Efficiency: The Inner Workings Of Compression Drivers**. en-US. [S.l.: s.n.], June 2014. Available from: https://www.prosoundweb.com/greater-efficiency-the-inner-workings-of-compression-drivers/. Visited on: 1 Feb. 2020.

EBEFORS, Thorbjorn; KALVESTEN, Edvard; STEMME, Göran. Three dimensional silicon triple-hot-wire anemometer based on polyimide joints. In: p. 93–98. DOI: 10.1109/MEMSYS.1998.659735.

EPA. **Meteorological Monitoring Guidance for Regulatory Modeling Applications**. [S.l.], 1 Feb. 2002. Available from: https://www3.epa.gov/scram001/guidance/met/mmgrma.pdf. Visited on: 29 Jan. 2020.

ETTS, Douglas; ROSSI, Mark; NZAOU, Roland; ZHU, Ruijie; LEWIN, Gregory C; WEKKER, Stephan FJ de. Development of an autonomous multi-rotor copter for collecting atmospheric data near the ground. In: IEEE. SYSTEMS and Information Engineering Design Symposium (SIEDS), 2015. [S.l.: s.n.], 2015. P. 120–124.

EVANS, Annette; STREZOV, Vladimir; EVANS, Tim J. Assessment of sustainability indicators for renewable energy technologies. **Renewable and Sustainable Energy Reviews**, v. 13, n. 5, p. 1082–1088, 2009. ISSN 1364-0321. DOI: https://doi.org/10.1016/j.rser.2008.03.008. Available from: http://www.sciencedirect.com/science/article/pii/S1364032108000555.

FAGIANO, Lorenzo; MILANESE, Mario. Airborne wind energy: an overview. In: IEEE. AMERICAN Control Conference (ACC), 2012. [S.l.: s.n.], 2012. P. 3132–3143.

FINN, Anthony; FRANKLIN, Stephen. UAV-based atmospheric tomography. In: PROC. 2011 Australian Acoustical Society Conf. [S.l.]: Australian Acoustical Society, 2011.

FINN, Anthony; ROGERS, Kevin. An acoustic tomography technique for concurrently observing the structure of the atmosphere and water bodies. **Journal of Atmospheric and Oceanic Technology**, v. 34, n. 3, p. 617–629, 2017.

FINN, Anthony; ROGERS, Kevin. An analysis of unmanned aerial vehicle-based acoustic atmospheric tomography. In: PROC. Acoustics 2016: The Second Australiasian Acoustical Societies Conf. [S.l.: s.n.], 2016a.

FINN, Anthony; ROGERS, Kevin. Improving Unmanned Aerial Vehicle–Based Acoustic Atmospheric Tomography by Varying the Engine Firing Rate of the Aircraft. **Journal of Atmospheric and Oceanic Technology**, v. 33, n. 4, p. 803–816, 2016b.

FINN, Anthony; ROGERS, Kevin. The feasibility of unmanned aerial vehicle-based acoustic atmospheric tomography. **The Journal of the Acoustical Society of America**, v. 138, n. 2, p. 874–889, Aug. 2015. ISSN 0001-4966. DOI: 10.1121/1.4926900. Available from: https://asa.scitation.org/doi/10.1121/1.4926900. Visited on: 7 Feb. 2020.

FINN, Anthony; ROGERS, Kevin; MEADE, Joshua; FRANKLIN, Stephen. Acoustic atmospheric tomography using multiple unmanned aerial vehicles. In: INTERNATIONAL SOCIETY FOR OPTICS and PHOTONICS. REMOTE Sensing of Clouds and the Atmosphere XIX; and Optics in Atmospheric Propagation and Adaptive Systems XVII. [S.l.: s.n.], 2014. 92420q.

FINN, Anthony; ROGERS, Kevin; RICE, Feng; MEADE, Joshua; HOLLAND, Greg; MAY, Peter. A Comparison of Vertical Atmospheric Wind Profiles Obtained from Monostatic Sodar and Unmanned Aerial Vehicle–Based Acoustic Tomography.

Journal of Atmospheric and Oceanic Technology, v. 34, n. 10, p. 2311–2328, 2017.

GIEBEL, Gregor; PAULSEN, Uwe Schmidt; BANGE, Jens; COUR-HARBO, Anders la; REUDER, Joachim; MAYER, Stephanie; KROONENBERG, Aline van der; MØLGAARD, John. Autonomous Aerial Sensors for Wind Power Meteorology-A Pre-Project. Danmarks Tekniske Universitet, Risø Nationallaboratoriet for Bæredygtig Energi, 2012.

GLEASON, Scott; GEBRE-EGZIABHER, Demoz. **GNSS Applications and Methods**. [S.l.]: Artech House, 2009. ISBN 9781596933293.

GODIN, Oleg A. An effective quiescent medium for sound propagating through an inhomogeneous, moving fluid. **The Journal of the Acoustical Society of America**, v. 112, n. 4, p. 1269–1275, Sept. 2002. ISSN 0001-4966. DOI: 10.1121/1.1504853. Available from: https://asa.scitation.org/doi/10.1121/1.1504853. Visited on: 3 Feb. 2020.

GOLDEMBERG, Jose; PROGRAMME., United Nations Development; COUNCIL., World Energy; NATIONS., United. **World energy assessment : energy and the challenge of sustainability / United Nations Development Programme, United Nations Department of Economic and Social Affairs, World Energy Council ; [edited by Jose Goldemberg]**. [S.l.]: United Nations Development Programme New York, 2000. vii, 508 p. : ISBN 9211261260.

HÖLLING, Michael; SCHULTE, B; BARTH, S; PEINKE, Joachim. Sphere anemometer - a faster alternative solution to cup anemometry. **Journal of Physics: Conference Series**, v. 75, p. 012064, Aug. 2007. DOI: 10.1088/1742-6596/75/1/012064.

HUBER, David Miles; RUNSTEIN, Robert E. **Modern Recording Technologies**. Ed. by Focal Press. 8th ed. Burlington, MA: [s.n.], 2014. ISBN 978-0-240-82464-2.

JONASSEN, Marius Opsanger. The Small Unmanned Meteorological Observer (SUMO). **Master's thesis, University of Bergen–Geophysical Institute**, 2008.

JØRGENSEN, Finn E. **How to measure turbulence with hot-wire anemometers**: a practical guide. [S.l.: s.n.], 1 Feb. 2002. Available from: http://web.iitd.ac.in/~pmvs/courses/mel705/hotwire2.pdf. Visited on: 6 Feb. 2020.

JOVANOVIC, Ivana. Inverse problems in acoustic tomography. EPFL, 2008.

KEITH WILSON, D; THOMSON, Dennis W. Acoustic tomographic monitoring of the atmospheric surface layer. **Journal of Atmospheric and Oceanic Technology**, v. 11, n. 3, p. 751–769, 1994.

KIT, Eliezer; LIBERZON, Dan. 3D-calibration of three- and four-sensor hot-film probes based on collocated sonic using neural networks. **Measurement Science and Technology**, v. 27, p. 095901, Sept. 2016. DOI: 10.1088/0957-0233/27/9/095901.

KONRAD, T. G.; HILL, M. L.; ROWLAND, J.R.; MEYER, J. H. A small, radio-controlled aircraft as a plat Variable & **Dates** & **Units** & **Source**
form for meteorological sensors, 1970.

KRISTENSEN, L. The perennial cup anemometer. **Wind Energy: An International Journal for Progress and Applications in Wind Power Conversion Technology**, Wiley Online Library, v. 2, n. 1, p. 59–75, 1999.

LANDES, Hermann; KALTENBACHER, Manfred; LERCH, R. Large Scale Computation of Coupled Electro-Acoustic Systems using ANSYS and CAPA. **NAFEMS-Seminar Computational Acoustics**, 11 Nov. 1999.

LANG, Steven; MCKEOGH, Eamon. LIDAR and SODAR Measurements of Wind Speed and Direction in Upland Terrain for Wind Energy Purposes. en. **Remote Sensing**, v. 3, n. 9, p. 1871–1901, Aug. 2011. ISSN 2072-4292. DOI: 10.3390/rs3091871. Available from: http://www.mdpi.com/2072-4292/3/9/1871. Visited on: 29 Jan. 2020.

LIU, Hui; DARABI, Houshang; BANERJEE, Pat; LIU, Jing. Survey of Wireless Indoor Positioning Techniques and Systems. **IEEE Transactions on Systems, Man, and Cybernetics, Part C (Applications and Reviews)**, v. 37, n. 6, p. 1067–1080, Nov. 2007. ISSN 1558-2442. DOI: 10.1109/TSMCC.2007.905750.

LOYD, Miles L. Crosswind kite power (for large-scale wind power production). **Journal of energy**, v. 4, n. 3, p. 106–111, 1980.

LUCHSINGER, Rolf et al. Pumping Cycle Kite Power with Twings. In: **Airborne Wind Energy: Advances in Technology Development and Research**. Ed. by Roland Schmehl. Singapore: Springer Singapore, 2018. P. 603–621. ISBN

978-981-10-1947-0. DOI: 10.1007/978-981-10-1947-0_24. Available from: https://doi.org/10.1007/978-981-10-1947-0_24.

MARTIN, S; BANGE, J; BEYRICH, F. Meteorological profiling of the lower troposphere using the research UAV" M 2 AV Carolo". **Atmospheric Measurement Techniques**, Copernicus GmbH, v. 4, n. 4, p. 705–716, 2011.

MCLAUGHLIN, Scott. **The right radar wind profiler for your application**. Saint Petersburg, Russian Federation, 2014. P. 11. Available from: https://library.wmo.int/pmb_ged/iom_116_en/Session%201/01_9_McLaughlin_RightRWPforJob.pdf.

MOYANO CANO, Javier. **Quadrotor UAV for wind profile characterization**. 2013. MA thesis.

MUNK, Walter; WORCESTER, Peter; WUNSCH, Carl. EPILOGUE. THE SCIENCE OF OCEAN ACOUSTIC TOMOGRAPHY. In: OCEAN Acoustic Tomography. [S.l.]: Cambridge University Press, 1995. P. 346–354. (Cambridge Monographs on Mechanics). DOI: 10.1017/CBO9780511666926.010.

MUNK, Walter; WUNSCH, Carl. Ocean acoustic tomography: A scheme for large scale monitoring. **Deep Sea Research Part A. Oceanographic Research Papers**, Elsevier, v. 26, n. 2, p. 123–161, 1979.

MURGATROYD, RJ; HELLIWELL, NC. The measurement of wind from aircraft using a Doppler navigation system. **The Journal of Navigation**, Cambridge University Press, v. 12, n. 1, p. 84–89, 1959.

NREL. **Wind Resource Assessment Handbook**. [S.l.]: National Renewable Energy Laboratory, Apr. 1997. Available from: https://www.nrel.gov/docs/legosti/fy97/22223.pdf.

OKE, T.R. **Boundary Layer Climates**. Ed. by Routledge. 2nd ed. [S.l.: s.n.], 2002. ISBN 0-203-40721-0.

OSTASHEV, V.; WILSON, D. **Acoustics in Moving Inhomogeneous Media**. London: CRC Press, 2016. DOI: https://doi.org/10.1201/b18922.

OSTASHEV, V.E.; VORONOVICH, A; WILSON, D.K. Acoustic tomography of the atmosphere. In: IEEE. GEOSCIENCE and Remote Sensing Symposium, 2000. Proceedings. IGARSS 2000. IEEE 2000 International. [S.l.: s.n.], 2000. P. 1186–1188.

PALOMAKI, Ross T; ROSE, Nathan T; BOSSCHE, Michael van den; SHERMAN, Thomas J; DE WEKKER, Stephan FJ. Wind estimation in the lower atmosphere using multirotor aircraft. **Journal of Atmospheric and Oceanic Technology**, v. 34, n. 5, p. 1183–1191, 2017.

PETERSON, Vern L.; HAYENGA, Craig; JOHNSTON, Paul; NEUSCHAEFER, John; SPURBECK, Mark; WOODARD, Douglas. **Wind Profiling**: History, Principles and Applications. [S.l.], Sept. 2002. Available from: ftp://ftp.aqmd.gov/pub/kdurkee/AMS_SC_BLProf/Frederick_Profiler/Vaisala_TechNote.pdf. Visited on: 29 Jan. 2020.

PRIYANTHA, N.B.; BALAKRISHNAN, H.; DEMAINE, E.D.; TELLER, S. Mobile-assisted localization in wireless sensor networks. In: PROCEEDINGS IEEE 24th Annual Joint Conference of the IEEE Computer and Communications Societies. [S.l.: s.n.], Mar. 2005. 172–183 vol. 1. ISSN: 0743-166X. DOI: 10.1109/INFCOM.2005.1497889.

PRUDDEN, S; WATKINS, S; FISHER, A; MOHAMED, A. A flying anemometer quadrotor: Part 1. In: IMAV. IMAV 2016. [S.l.: s.n.], 2016. P. 15–21.

PUCZYLOWSKI, Jaroslaw. **2D-Laser Cantilever Anemometer**. Ed. by ForWind -Center for Wind Energy Research. [S.l.: s.n.], 2014. Available from: https://uol.de/fileadmin/user_upload/physik/ag/twist/Forschung/LaserCantilever.pdf. Visited on: 28 Jan. 2020.

RANNEBERG, Maximilian; WÖLFLE, David; BORMANN, Alexander; ROHDE, Peter; BREIPOHL, Florian; BASTIGKEIT, Ilona. Fast Power Curve and Yield Estimation of Pumping Airborne Wind Energy Systems. In: [s.l.: s.n.], Apr. 2018. P. 623–641. ISBN 978-981-10-1946-3. DOI: 10.1007/978-981-10-1947-0_25.

REED, Wilmer H.; LYNCH, James W. A Simple Fast Response Anemometer. **Journal of Applied Meteorology**, v. 2, n. 3, p. 412–416, 1963. DOI: 10.1175/1520-0450(1963)002<0412:ASFRA>2.0.CO;2. eprint: https://doi.org/10.1175/1520-0450(1963)002<0412:ASFRA>2.0.CO;2. Available from: https://doi.org/10.1175/1520-0450(1963)002%3C0412:ASFRA%3E2.0.CO;2.

ROGERS, Kevin; FINN, Anthony. 3D acoustic atmospheric tomography. In: INTERNATIONAL SOCIETY FOR OPTICS and PHOTONICS. REMOTE Sensing of Clouds and the Atmosphere XIX; and Optics in Atmospheric Propagation and Adaptive Systems XVII. [S.l.: s.n.], 2014. 92420r.

ROGERS, Kevin; FINN, Anthony, et al. **3D atmospheric tomography using UAVs**. 2013. PhD thesis – Australian Acoustical Society, South Australian Division.

ROGERS, Kevin; FINN, Anthony. Three-dimensional UAV-based atmospheric tomography. **Journal of Atmospheric and Oceanic Technology**, v. 30, n. 2, p. 336–344, 2013.

ROGERS, Kevin J; FINN, Anthony. Frequency estimation for 3d atmospheric tomography using unmanned aerial vehicles. In: IEEE. INTELLIGENT Sensors, Sensor Networks and Information Processing, 2013 IEEE Eighth International Conference on. [S.l.: s.n.], 2013. P. 390–395.

SCHABACK, Robert. A Practical Guide to Radial Basis Functions. [S.l.], 16 Apr. 2007. Available from: `https://num.math.uni-goettingen.de/schaback/teaching/sc.pdf`. Visited on: 26 Jan. 2020.

SCHMIDT, Eduardo. **A state estimation strategy for monitoring, control, and optimization of airborne wind energy systems**. 2017. MA. Thesis – Universidade Federal de Santa Catarina.

SCHMIDT, Richard E. **BUILDING A RASPBERRY PI ZERO GPS NETWORK TIME SERVER FOR UNDER 50**. [S.l.: s.n.]. Available from: `https://www.satsignal.eu/raspberry-pi/Schmidt-RPZ-NTP-2016.pdf`. Visited on: 5 Feb. 2020.

SILVA, Edna Lúcia da; MENEZES, Estera Muszkat. Metodologia da pesquisa e elaboração de dissertação. 3. ed. rev. atual, 2001.

SPIESBERGER, John L; FRISTRUP, Kurt M. Passive localization of calling animals and sensing of their acoustic environment using acoustic tomography. **The american naturalist**, University of Chicago Press, v. 135, n. 1, p. 107–153, 1990.

STULL, Roland. **Practical Meteorology: An Algebra-based Survey of Atmospheric Science.** Commentary: version 1.02b. 3rd. Vancouver, BC, Canada: University of British Columbia, 2017. P. 940. ISBN 978-0-88865-283-6.

THRESHER, Robert; ROBINSON, Michael; VEERS, Paul. To capture the wind. **IEEE Power and Energy Magazine**, IEEE, v. 5, n. 6, p. 34–46, 2007.

TITTERTON, David H.; WESTON, John L. **Strapdown Inertial navigation Technology.** 2nd ed. [S.l.]: The Institution of Electrical Engineers, 2004. ISBN 0863413587.

TOMAŠTÍK, Julián; MOKROŠ, Martin; SUROVÝ, Peter; GRZNÁROVÁ, Alžbeta; MERGANIČ, Ján. UAV RTK/PPK Method—An Optimal Solution for Mapping Inaccessible Forested Areas? en. **Remote Sensing**, v. 11, n. 6, p. 721, Jan. 2019. DOI: 10.3390/rs11060721. Available from: https://www.mdpi.com/2072-4292/11/6/721. Visited on: 6 Feb. 2020.

TORRIERI, Don J. Statistical Theory of Passive Location Systems. **IEEE Transactions on Aerospace and Electronic Systems**, AES-20, n. 2, p. 183–198, Mar. 1984. ISSN 2371-9877. DOI: 10.1109/TAES.1984.310439.

VECHERIN, Sergey N.; OSTASHEV, Vladimir E.; GOEDECKE, George H.; WILSON, D. Keith; VORONOVICH, Alexander G. Time-dependent stochastic inversion in acoustic travel-time tomography of the atmosphere. **The Journal of the Acoustical Society of America**, v. 119, n. 5, p. 2579–2588, Apr. 2006. ISSN 0001-4966. DOI: 10.1121/1.2180535. Available from: https://asa.scitation.org/doi/10.1121/1.2180535. Visited on: 3 Feb. 2020.

WEISSHAUPT, Nadja; ARIZAGA, Juan; MARURI, Mercedes. The role of radar wind profilers in ornithology. en. **Ibis**, v. 160, n. 3, p. 516–527, 2018. ISSN 1474-919X. DOI: 10.1111/ibi.12562. Available from: https://onlinelibrary.wiley.com/doi/abs/10.1111/ibi.12562. Visited on: 29 Jan. 2020.

WIENS, Travis; BEHRENS, Paul. Turbulent flow sensing using acoustic tomography. In: INSTITUTE OF NOISE CONTROL ENGINEERING, 7. INTER-NOISE and NOISE-CON Congress and Conference Proceedings. [S.l.: s.n.], 2009a. P. 336–344.

WIENS, Travis; BEHRENS, Paul. Turbulent flow sensing using acoustic tomography. In: BOLTEON, J. S. (Ed.). **38th International Congress and Exposition on Noise Control Engineering 2009 (INTER-NOISE 2009)**. [S.l.: s.n.], Jan. 2009b.

WMO. Annex 1.E. Operational Measurement Uncertainty Requirements and Instrument Performance. In: GUIDE to Instruments and Methods of Observation. 2014 Ed. [S.l.]: World Meteorological Organization (WMO), 2014. .I, chap. 1. (WMO- No. 8). ISBN 978-92-63-10008-5. Available from: https://library.wmo.int/doc_num.php?explnum_id=4147. Visited on: 5 Feb. 2020.

WOLF, Carl A; HARDIS, Richard P; WOODRUM, Steven D; GALAN, Richard S; WICHELT, Hunter S; METZGER, Michael C; BEZZO, Nicola; LEWIN, Gregory C; WEKKER, Stephan FJ de. Wind data collection techniques on a multi-rotor platform. In: IEEE. SYSTEMS and Information Engineering Design Symposium (SIEDS), 2017. [S.l.: s.n.], 2017. P. 32–37.

ZEKAVAT, Reza; BUEHRER, R. Michael. **Handbook of Position Location: Theory, Practice, and Advances**. 2nd ed. [S.l.]: Wiley-IEEE Press, 2019. ISBN 9781119434580.

ZHANG, Lei; WU, Xiaolin. On the application of cross correlation function to subsample discrete time delay estimation. en. **Digital Signal Processing**, v. 16, n. 6, p. 682–694, Nov. 2006. ISSN 1051-2004. DOI: 10.1016/j.dsp.2006.08.009. Available from: http://www.sciencedirect.com/science/article/pii/S1051200406001230. Visited on: 5 Feb. 2020.

ZIEMANN, A.; ARNOLD, K.; RAABE, A. Acoustic tomography in the atmospheric surface layer. en. **Annales Geophysicae**, v. 17, n. 1, p. 139–148, Dec. 1998. ISSN 1432-0576. DOI: 10.1007/s00585-999-0139-9. Available from: https://doi.org/10.1007/s00585-999-0139-9. Visited on: 2 Feb. 2020.

ZIEMANN, Astrid; ARNOLD, Klaus; RAABE, Armin. Acoustic tomography as a remote sensing method to investigate the near-surface atmospheric boundary layer in comparison with in situ measurements. **Journal of Atmospheric and Oceanic Technology**, v. 19, n. 8, p. 1208–1215, 2002.

ZIEMANN, Astrid; ARNOLD, Klaus; RAABE, Armin. Acoustic tomography in the atmospheric surface layer. In: SPRINGER, 1. ANNALES Geophysicae. [S.l.: s.n.], 1998. P. 139–148.

ZILLMANN, Udo; BECHTLE, Philip. Emergence and Economic Dimension of Airborne Wind Energy. In: [s.l.: s.n.], Apr. 2018. P. 1–25. ISBN 978-981-10-1946-3. DOI: 10.1007/978-981-10-1947-0_1.